Predicting mooring line forces of large-scale vessels using machine learning

A case study at the Port of Rotterdam

N.K.S. Wilking

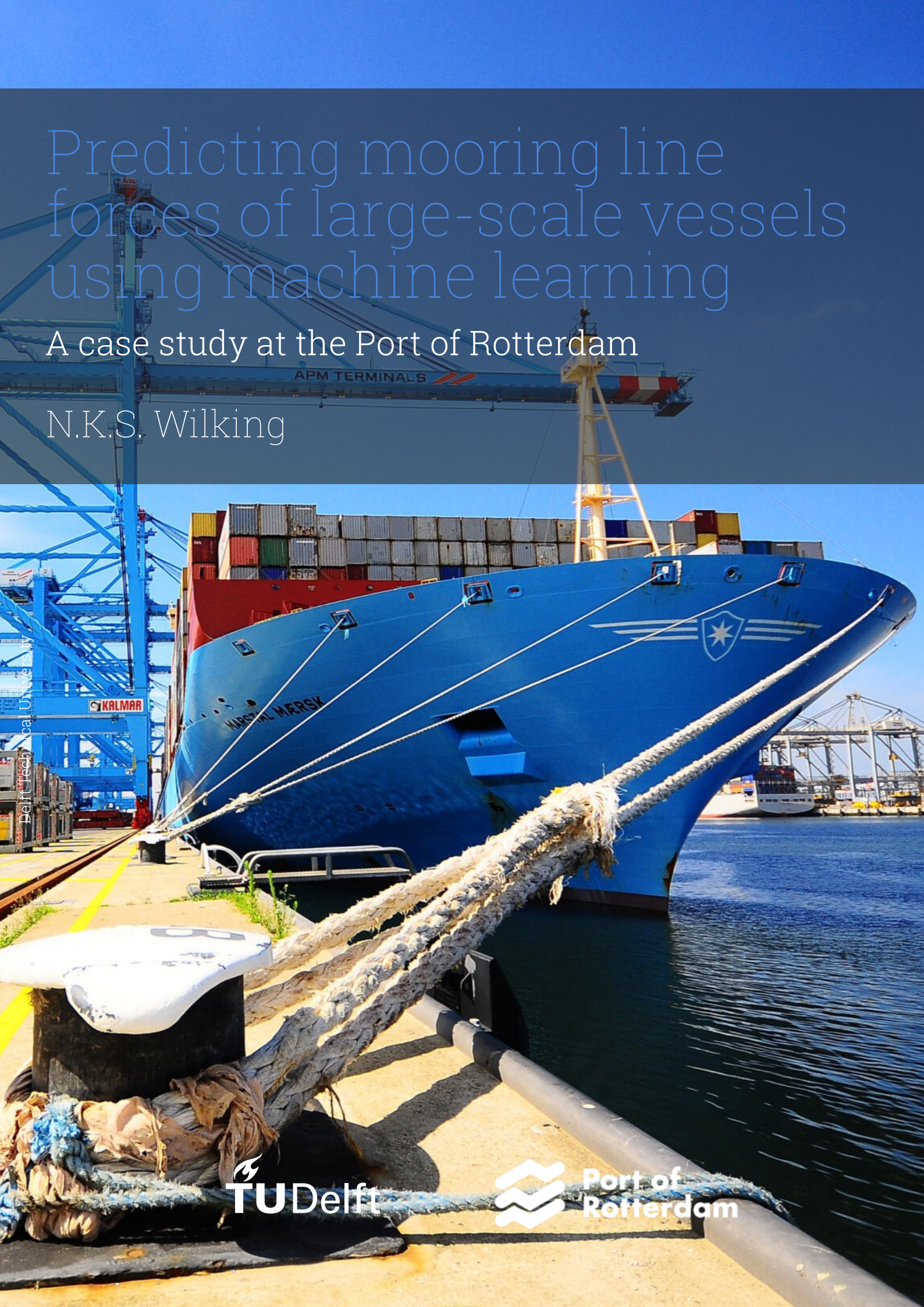

Delft University of Technology

TU Delft

Port of Rotterdam

Predicting mooring line forces of large-scale vessels using machine learning

A case study at the Port of Rotterdam

by

N.K.S. Wilking

Master thesis

in partial fulfillment of the requirements for the degree of

Master of Science
in Mechanical Engineering

at the Department Maritime and Transport Technology of Faculty Mechanical Engineering of Delft University of Technology
to be defended publicly on Thursday July 17, 2025 at 10:00 AM

Student number:	4681444	
MSc track:	Multi-Machine Engineering	
Report number:	2025.MME.9080	
Thesis committee:	Dr. V. Reppa	TU Delft committee chair, ME
	Ir. J. Burgers,	Company supervisor, Port of Rotterdam
	Dr.ir. A. Roubos,	TU Delft committee member, CiTG
	Dr.ir. A. van Deyzen,	Company supervisor, Haskoning
	Dr. F. Schulte	TU Delft committee member, ME
Date:	July 10, 2025	

Cover: Container ship moored at the Maasvlakte, port of Rotterdam (Cornelissen, 2021)

TU Delft

Port of Rotterdam

Preface

This thesis is the final step in completing my MSc degree in Mechanical Engineering at Delft University of Technology, with a specialization in Multi-Machine Engineering.

Port of Rotterdam offered me the opportunity to conduct this research during an internship. The experience of not only observing the port from the World Port Center, where I could even spot the TU Delft campus on clear days, but also visiting and experiencing the port, has been invaluable.

I am especially thankful to Joppe Burgers for his enthusiasm, guidance, and encouragement throughout the project. Secondly, I extend my appreciation to my TU Delft supervisor, Vasso Reppa, for her time and valuable advice. Alfred Roubos, thank you for your thoughtful input, and your dual role representing both the Port of Rotterdam and TU Delft. I also am grateful to Alex van Deyzen from Haskoning, whose DMA expertise was of great help. Special thanks go to the shoremen from the KRVE. Spending a day with them mooring an unmooring large vessels provided me with a unique and practical perspective on the subject of this thesis.

Finally, I want to thank my family, friends and Pepijn for their unconditional support.

Noor Wilking
Rotterdam, July 2025

AI usage statement

During the course of this thesis research, artificial intelligence (AI) tools were used to support the writing and development process. These tools assisted with textual editing, scripting and code debugging, and LaTeX formatting.

All content generated with the help of AI was carefully reviewed, and the tools were used strictly for support. The author takes full responsibility for the content and conclusions presented in this thesis.

Summary

The increasing size of cargo vessels poses significant challenges for ports in ensuring safe mooring operations, as larger ships result in higher mooring forces. Excessive mooring line forces can have catastrophic outcomes, including severe injuries or fatalities to personnel, along with vessels breaking free to cause costly collisions and environmental damage. However, most existing port infrastructure and mooring equipment were designed for smaller ships, creating a disparity between vessel size and infrastructure capabilities. This raises concerns about the safe and efficient mooring of current and future ship generations. To address these risks, accurately predicting mooring line forces is essential for enabling timely and effective mitigation measures.

A numerical approach called Dynamic Mooring Analysis (DMA) can be used to predict moored vessel behavior. DMA solves the equations of motion in six degrees of freedom in the time domain, accounting for nonlinear interactions between ship, mooring system, and environment. However, these simulations are computationally expensive. Machine learning (ML) offers a data-driven alternative by capturing the nonlinear behavior of moored ships through training on measured field data, thereby eliminating the need to explicitly model physical processes. This approach, though promising, typically suffers from limited interpretability and requires large, costly field measurement datasets.

Metamodeling provides a potential solution. In this technique, ML models are trained on simulated data, serving as a simplified surrogate for a more complex numerical model. Metamodels offer similar predictive capabilities but at significantly reduced computational cost, making them suitable for large-scale scenario analysis. Moreover, they can provide insights into system behavior and sensitivities of the original numerical model.

There is a gap in the existing literature on metamodels specifically developed for predicting mooring line forces of large-scale vessels in port environments. This research addresses this gap through the following research question: How can mooring line forces of large-scale vessels within port areas be predicted using machine learning techniques? To answer this, the thesis investigates the development of a machine learning-based metamodel that replicates the results of traditional DMA.

A metamodeling approach is proposed in which ML algorithms, namely Linear Regression (LR) and a Multi-Layer Perceptron (MLP), are trained on a systematically generated dataset of simulated mooring scenarios. These scenarios are created by varying input parameters across the key aspects characterizing mooring: environmental conditions, mooring system, and ship characteristics. The resulting models are evaluated through a multi-objective evaluation framework.

The method was applied to a case study involving a 333-meter container vessel moored at the Port of Rotterdam. Input parameters included environmental, mooring, and vessel-specific factors, while the targets were the mean and maximum mooring line forces. A total of 11,520 scenarios were simulated to form the DMA dataset. This dataset was used to train and test both LR and MLP models. The models were then evaluated based on their accuracy, efficiency in terms of both prediction time and development effort, and lastly interpretability. Based on this evaluation, the MLP model was selected as the final DMA metamodel. It achieved high predictive accuracy (R^2 = 0.996, RMSE = 10 kN) while predicting mooring forces in microseconds, a significant improvement over the 30 seconds per scenario required by numerical DMA. This makes the metamodel well suited for large-batch predictions. Interpretability was addressed through permutation importance and SHAP analysis, providing insights into the influence of individual input features.

In addition, a practical method was proposed to estimate uncertain input parameters, such as pretension and viscous damping, using field measurements. This approach showed promising results for the mean mooring line force but was less reliable for maximum mooring line forces, highlighting the need for multi-objective optimization and more extensive measurement datasets.

The results demonstrate that the DMA metamodel based on MLP is a viable and efficient tool for mooring line force prediction, with practical relevance for port authorities and maritime engineers. Future research should extend the model to different vessel sizes, and explore additional ML algorithms, expand scenario design, and develop models based solely on measured field data.

Abbreviations

ANFIS	Adaptive Neuro-Fuzzy Inference System
ANN	Artificial Neural Network
BHC	Brake Holding Capacity
DL	Deep Learning
DMA	Dynamic Mooring Analysis
DNN	Deep Neural Network
DoF	degrees of freedom
EN	Equipment Number
HMPE	High Molecular PolyEthylene
KRVE	Royal Boatmen Association Eendracht
LHS	Latin Hypercube Sampling
MAE	Mean Absolute Error
MARIN	Maritime Research Institute the Netherlands
MBL	Minimal Breaking Load
$\mathbf{MBL_{SD}}$	Ship Design MBL
MCA	multi-criteria analysis
ML	Machine Learning
MLP	Multi-Layer Perceptron
MSE	Mean Squared Error
NAP	Nederlands Amsterdams Peil
OLS	Ordinary Least Squares
QRH	Quick Release Hook
$\mathbf{R^2}$	Coefficient of Determination
RMSE	Root Mean Squared Error
SLS	Serviceability Limit State
SWL	Safe Working Load
UKC	under keel clearance
ULS	Ultimate Limit State

List of Figures

List of Tables

Contents

1 Introduction

This chapter starts with background information, including the problem statement and a brief literature review. From this, the research gap is identified, the research questions are defined, and the scope of the study is outlined. Finally, the structure of this thesis is presented.

1.1. Background

1.1.1. Increasing mooring forces

In recent years, a significant expansion in cargo vessel dimensions and capacities has been observed, as illustrated in Figure 1.1 (UNCTAD, 2023). This trend of ever-increasing ship sizes poses significant challenges for ports worldwide in ensuring safe mooring operations (Van Zwijnsvoorde, Donatini, et al., 2019). Larger ships experience greater environmental forces (Sáenz et al., 2023; Van Zwijnsvoorde et al., 2018), resulting in higher mooring loads, including increased mooring line forces.

Excessive mooring line forces can lead to catastrophic outcomes. Line failures may cause severe injuries or fatalities to crew members and port personnel. Additionally, vessels may break free from their moorings, resulting in collisions with port infrastructure or other ships, causing substantial economic losses and potential environmental damage.

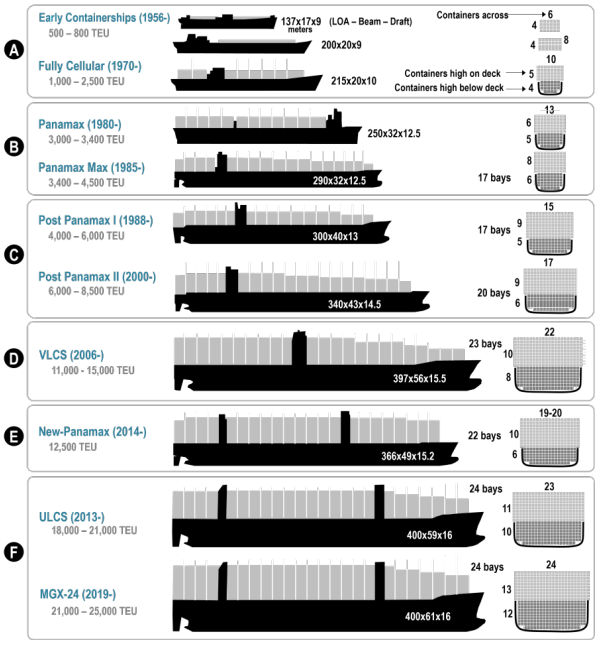

Figure 1.1: Evolution of new generation container ships illustrating the increase in physical dimensions and TEU capacity over time (Rodrigue, 2024)

The majority of the existing port infrastructure and mooring equipment were designed for smaller ships than those currently visiting (Van Zwijnsvoorde, Donatini, et al., 2019). As a result, the growing disparity between vessel size and infrastructure design raises concerns about the safe and efficient mooring of future ship generations.

1.1.2. Port of Rotterdam

This problem is also relevant to the Port of Rotterdam (Figure 1.2), the largest port of Europe. Covering over 12,000 hectares, the port features 76 kilometers of quay walls, 126 jetties, and a wide range of mooring facilities such as dolphins and buoys (Figure 1.3). With a water depth of up to 24 meters, it is capable of accommodating vessels with the deepest draughts. In 2023, the Port of Rotterdam handled approximately 28,000 seagoing vessels and 89,000 inland vessels, with a total cargo throughput of 438.8 million tonnes. This included dry and liquid bulk cargo, containers (13,446,709 TEU), and break bulk (Port of Rotterdam Authority, 2024b).

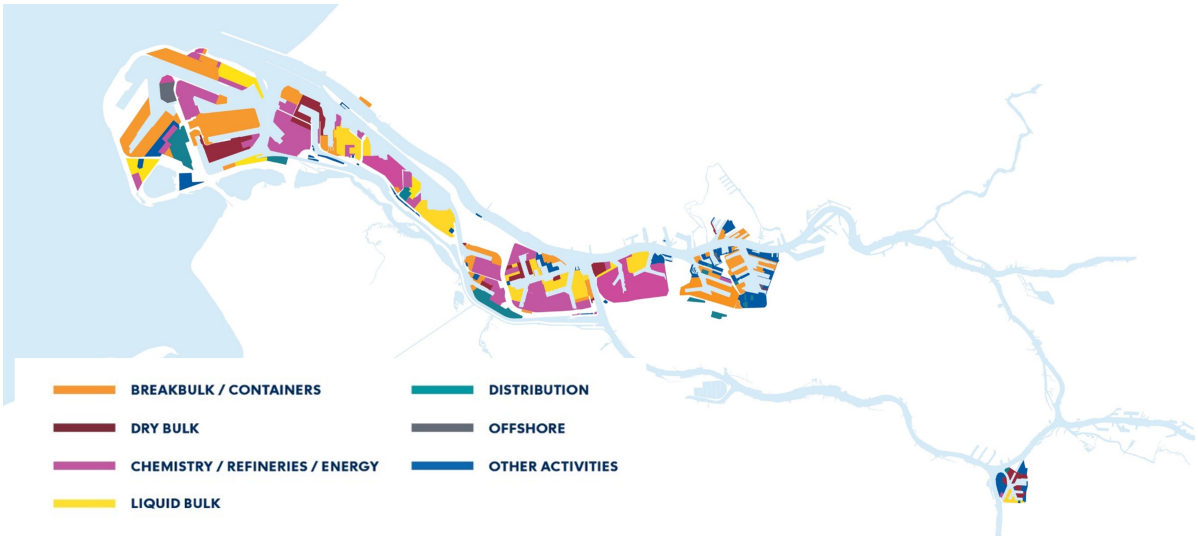

Figure 1.2: Overview of the Port of Rotterdam area, which covers over 12,000 hectares (Port of Rotterdam, 2024)

The Port of Rotterdam Authority, a public company jointly owned by the municipality of Rotterdam and the Dutch government, is responsible for the management, operation, and sustainable development of the port and industrial area (Port of Rotterdam Authority, 2024a).

When there is a risk that moored vessels break loose due to extreme conditions, the Rotterdam Port Authority can employ several mitigating measures to prevent such incidents (Port of Rotterdam, 2023). However, the responsibility for taking these measures lies with the captain of a moored vessel. One approach is to add more ballast water to increase the weight of the vessel and thereby reduce its surface area exposed to wind. ShoreTension systems can be applied as well. Moreover, additional lines can be deployed to (storm) bollards and tugboats can assist by pushing the vessel toward the quay to maintain its position. In very extreme cases, vessels may be sent out to sea, where they are safer by maintaining a favorable wind course. However, this measure is hardly implemented in practice.

The increasing vessel dimensions raise concerns on the part of the Port Authority regarding its ability to safely accommodate such ships in the future. These concerns served as the main motivation for initiating this thesis.

To ensure the mooring safety, it is essential that the Port Authority can accurately estimate mooring forces. This allows the implementation of mitigation measures in time, assessment of whether existing bollards have sufficient capacity, and evaluation of which future vessels can be safely moored in order to enabling optimal use of the existing port infrastructure.

(a) Quay wall (Cornelissen, 2021)

(b) Mooring dolphins (De Roo, 2023)

(c) Jetty (Donker, 2018)

(d) Mooring buoys in the Waalhaven (Port of Rotterdam, 2015)

Figure 1.3: Different types of berths in the port of Rotterdam

1.1.3. Estimating mooring forces

Two main approaches for estimating moored vessel response, exist in the scientific literature: numerical modeling and machine learning. While numerical models are physics-based and simulate detailed interactions, machine learning offers a data-driven alternative that may overcome some limitations of traditional methods. A promising intermediate approach is metamodeling, which uses machine learning trained on simulated data to approximate numerical models at lower computational cost.

1.1.3.1. Numerical modeling

Dynamic Mooring Analysis (DMA), based on time-domain numerical simulations, is widely used to estimate ship responses under various environmental conditions. These methods solve the equations of motion for moored vessels and often involve a series of coupled sub-models (Romano-Moreno et al., 2022).

Numerous studies have demonstrated the application of numerical models for predicting moored vessel behavior. Weiler et al. (2009) combined hydrodynamic scale model tests and time-domain computer simulations to analyze an LNG carrier moored at a jetty with complex bathymetry in Yemen. Van der Molen et al. (2016) evaluated various mooring configuration improvements at Geraldton Harbour, which suffers from long wave-induced vessel motions, by comparing numerical simulations. Van Zwijnsvoorde and Vantorre (2017) numerically simulated an 18,000 TEU container vessel at berth, analyzing mooring line forces under passing ship effects. Gourlay (2019a) developed a coupled ship-and-harbor model to predict wave-induced motions and mooring line and fender loads of moored ships in Geraldton Harbour in Autralia. Sundar et al. (2019) performed a comprehensive simulation of mooring line forces due to combined wind, wave, current, and passing ship effects at Mumbai Port. Sáenz et al. (2023) investigated the impact of next-generation ULCVs (up to 40,000 TEU) on port mooring systems, by simulating the effects of wind and passing ship forces. M. Yan et al. (2023) employed numerical modeling to analyze the hydrodynamic response of moored ships under harbor oscillations. Gourlay (2023) modeled six-buoy spread mooring systems at Cape Cuvier in Australia in order to calculate the wave-induced motions and loads and validated results using field measurements.

Although numerical modeling offers flexibility and is grounded in physical principles, the results can be limited by the complexity of multivariate and nonlinear modeling (Liu et al., 2020; Taveira Pinto et al., 2008). Moreover, it requires many variables that may not always be available. Therefore, hypothetical

or standard values must be assumed, introducing uncertainties (Romano-Moreno et al., 2023). Additionally, the computational cost of numerical modeling makes it impractical for large-batch scenario analysis.

1.1.3.2. Machine learning

Machine Learning (ML) offers a data-driven alternative to traditional simulation-based methods that can capture the nonlinear behavior of moored ships (Liu et al., 2020). Several studies have explored machine learning methods for moored vessel response prediction, employing various algorithms and training on measurement data from field or scaled experiments. S. Li and Qiu (2017) developed a genetic algorithm-back propagation neural network (GA-BP) model to predict mooring forces in an open sea terminal from environmental conditions and the ship's draught defined as input parameters. Liu et al. (2020) trained an artificial neural network (ANN) to predict mooring force, using wave characteristics, ship specifications, and mooring line length as inputs. S. Li and Qiu (2016) proposed a model based on Artificial Neural Network (ANN) techniques to predict the motions of moored ships in an open sea terminal using meteorological parameters and ship draught as input parameters. Alvarellos et al. (2021) created models that predict the 6 degrees of freedom (DoF) of a moored vessel using ocean meteorological data and ship characteristics based on neural network and gradient boosting methods. The model was trained using measured data from field campaigns. Finally, Romano-Moreno et al. (2022) presented a semi-supervised machine learning model to predict moored ship motions from met-ocean variables and ship characteristics, using the same dataset as Alvarellos et al. (2021).

A key advantage of ML techniques is their ability to handle the nonlinear nature of moored ship response. They learn complex relationships directly from data, eliminating the need for explicit physical processes modeling (Liu et al., 2020). However, they typically suffer from limited interpretability (Alvarellos et al., 2021) and require large datasets to avoid overfitting (Kadhim et al., 2023). Moreover, the acquisition of measured field data is costly, logistically challenging, and sometimes unfeasible under severe weather conditions (Romano-Moreno et al., 2022; Alvarellos et al., 2021).

1.1.3.3. Metamodeling

Metamodeling offers a promising alternative. In this approach, ML models are trained on synthetic data generated from numerical simulations. The resulting metamodel can approximate the behavior of the original numerical model at a fraction of the computational cost (Wang et al., 2014).

Several studies have explored training ML models on simulated data in mooring applications, although these have primarily focused on offshore floating structures. Saad et al. (2021) presented two neural networks to predict the movement of a floating platform based on the observation of past time series. The models were trained with simulated motion data generated using actual environmental conditions measured in Rio de Janeiro, Brazil. Mentes and Yetkin (2022) proposed an ANN and Adaptive Neuro-Fuzzy Inference System (ANFIS) to estimate the mooring line tension and displacements of the spread mooring system of a floating platform or vessel, also using simulated data. Sidarta et al. (2023) developed a ANN-based method to detect mooring line failures by identifying subtle shifts in motion patterns of floating offshore platforms. Their model was trained on numerical simulations and tested with modified field data. Sun et al. (2024) assessed five ML methods in order to explore a suitable metamodel to replace time-domain numerical simulation for offshore floating structures. Yetkin and Mentes (2015) presented a metamodel based on ANN to predict mooring tensions and tanker motion displacements in spread mooring systems. Ye et al. (2024) developed a metamodel for floating offshore wind turbines to predict, among other targets, the motion response, incorporating it into a design optimization approach.

1.2. Research gap

While ML models trained on simulated data have been studied in offshore applications, their use in port environments, and specifically for predicting mooring line forces of large vessels, remains underexplored. The objective of this study is to fill this gap by developing a metamodel for Dynamic Mooring Analysis to predict mooring line forces of large-scale vessels moored in port areas.

1.3. Research questions

The aim of this thesis is to answer the following main research question (RQ):

How can mooring line forces of large-scale vessels moored within port areas be predicted using machine learning techniques?

Based on the main question, the following sub-questions (SQs) were formulated:

SQ1. What are the key aspects characterizing the mooring of large-scale vessels in port areas?

SQ2. What are the fundamental principles and key considerations of Dynamic Mooring Analysis for predicting mooring line forces of large-scale vessels in port areas?

SQ3. How can a metamodel for Dynamic Mooring Analysis be developed using machine learning techniques to predict mooring line forces of large-scale vessels in port areas?

SQ4. What objectives and criteria are relevant for evaluating and selecting a metamodel for Dynamic Mooring Analysis?

SQ5. Which proposed machine learning technique provides the best metamodel for Dynamic Mooring Analysis?

SQ6. How to utilize the metamodel for estimating unknown input parameters?

SQ7. What specific field data should be collected by Port of Rotterdam to enhance applicability of machine learning models for mooring line force prediction, and what recommendations can be made for developing such models?

1.4. Scope limitations

This research investigates the development and evaluation of metamodels for predicting mooring line forces of large-scale vessels moored in port environments, applying the approach to a case study in the Port of Rotterdam. The study is conducted within the following scope and limitations:

- Only the period during which a ship is moored and thus physically secured at a berth is considered. Accordingly, berthing maneuvers are excluded.
- The environmental conditions included are constrained to time-varying wind. Other dynamic influences such as currents, waves, water level variations due to tides, and the effects of passing vessels are excluded.
- Mooring line failure is not explicitly modeled. Consequently, unrealistically high line forces may be predicted in certain scenarios, without accounting for force redistribution following a line failure.
- The case study is limited to a single berth and vessel. Bollard and fender layouts, as well as their mechanical properties, are fixed throughout the study. Similarly, the moored vessel type, draught, and mooring line arrangement remain constant.
- The machine learning scope is restricted to two regression algorithms: Linear Regression and Multi-Layer Perceptron. Other potentially relevant models are not explored.
- The metamodel based on the case study is designed to predict only two output variables: the mean mooring line force and the maximum mooring line force.

1.5. Outline

This thesis report addresses the research questions comprehensively. An overview of the structure is illustrated in Figure 1.4.

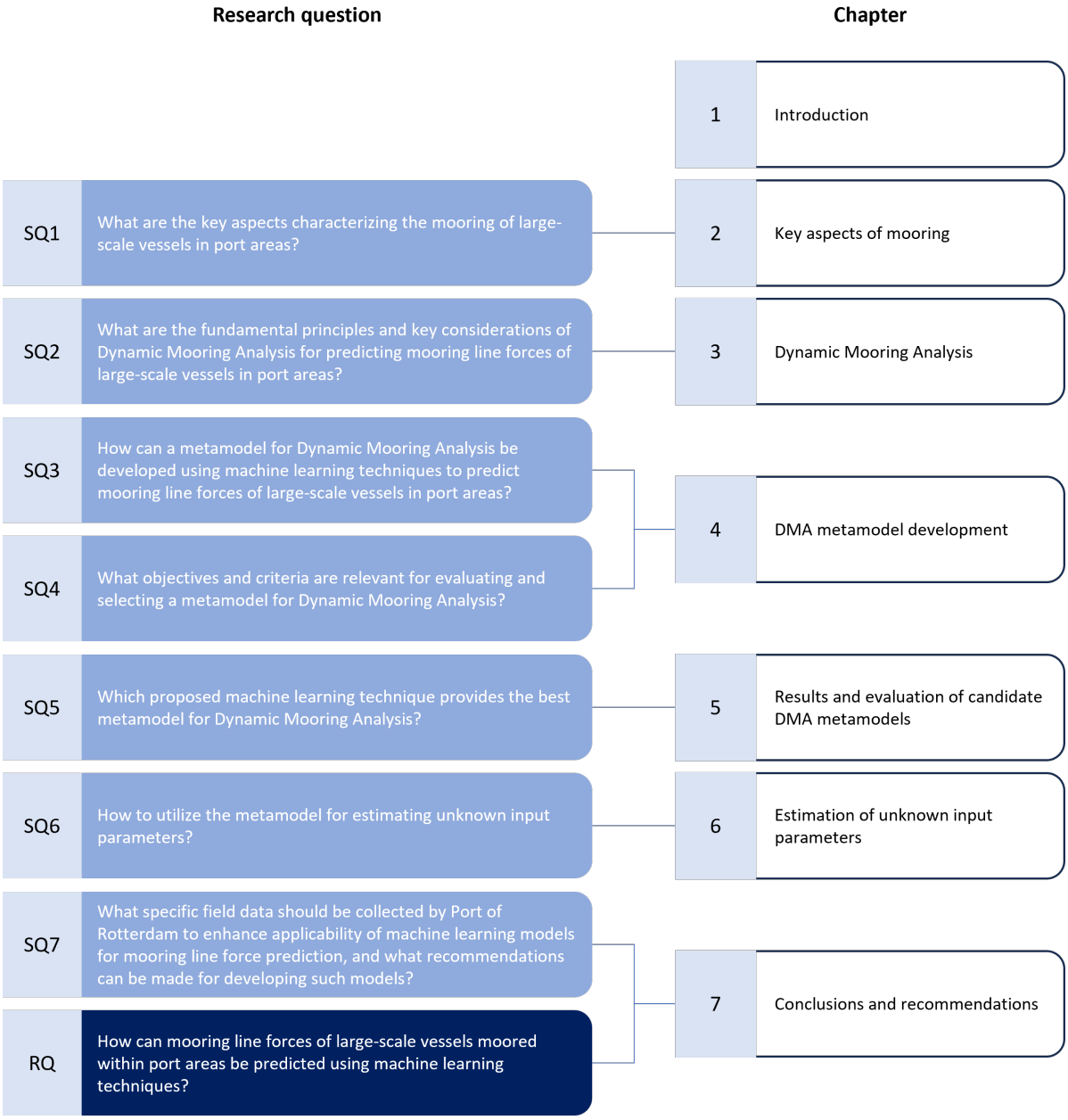

Figure 1.4: Overview of the report structure in relation to the research questions

Chapter 2 defines the key aspects that characterize the mooring of large-scale vessels in port areas via a literature review. Chapter 3 explains the fundamental principles of Dynamic Mooring Analysis (DMA) and its key considerations. Chapter 4 outlines the metamodeling approach, covering the general methodology, DMA metamodel development, and a case study application. Chapter 5 presents the results of the candidate DMA metamodels built and the selection of the optimal DMA metamodel. Chapter 6 proposes a method to estimate unknown parameters via measured field data using the DMA metamodel. Chapter 7 summarizes the conclusions to all sub-questions, addresses the main research question, and proposes several recommendations for future work as well as for field data collection to support the development of new ML models for mooring line force prediction at the Port of Rotterdam.

Appendix A presents a scientific research paper derived from this thesis report, titled *Prediction of mooring line forces using metamodeling*. Appendix B defines the case study scenarios used for numerical DMA simulations. Appendix C provides the data analysis performed on the complete set of DMA sim-

ulation results. Appendix E describes the measurement data used to update input parameters of the metamodel. Appendix F illustrates how the DMA metamodel can be applied to estimate the probability of bollard capacity exceedance during the operational design lifetime.

2

Key aspects of mooring

This chapter provides a literature-based exploration of SQ1: *What are the key aspects characterizing the mooring of large-scale vessels in port areas?*

A moored vessel is subjected to several forces resulting in a dynamic response. Its response is defined as the mooring force (mooring line tension and fender force) and moored vessel movement. It is characterized by three key aspects which are illustrated in Figure 2.1: environmental conditions, mooring system, and ship characteristics (Liu et al., 2020).

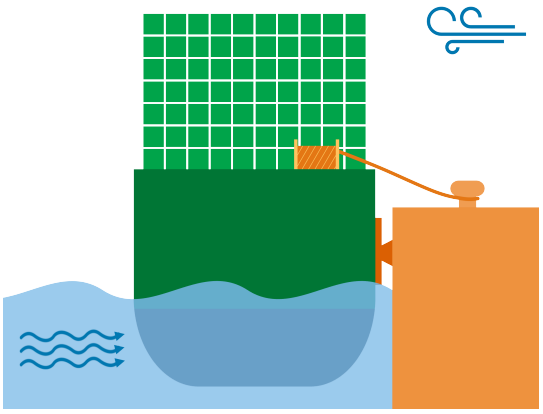

Figure 2.1: External conditions (blue), mooring system (orange), and vessel specifications (green) are the key aspects that influence mooring situations

Section 2.1 explores the environmental conditions that exert forces on a moored ship and consist of both natural phenomena and operational activities. Next, Section 2.2 discusses the components of the mooring system. Lastly, Section 2.3 focuses on the characteristics of the moored ship.

2.1. Environmental conditions

Moored vessels experience a variety of external loads arising from environmental conditions. They can be categorized into natural phenomena encompassing wind, currents, and waves, and operational influences including the effects of passing ship traffic (Abdelwahab et al., 2024; Van Zwijnsvoorde et al., 2018; Sáenz et al., 2023; Van Koningsveld et al., 2023). These environmental conditions are visualized in Figure 2.2.

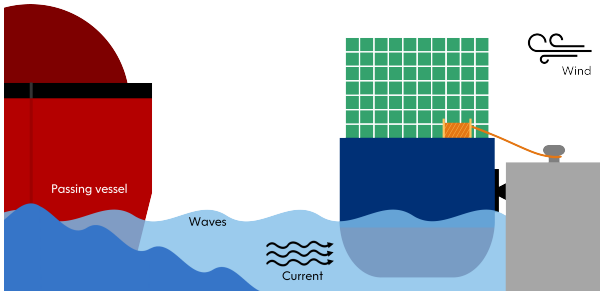

Figure 2.2: Wind, current, waves, tide, and passing ships generate external forces on a moored ship

The environmental forces can be categorized into two main components: static and dynamic. Static forces show minimal variation over short periods of time and include current, constant wind, and short-period waves. Dynamic forces fluctuate significantly within a short time, such as long-period waves, gusting wind, and passing ship effects (OCIMF, 2018).

The port configuration and terminal's layout directly impact the exposure of a moored vessel to environmental conditions and, consequently, on the magnitude of these forces (Sáenz et al., 2023; OCIMF, 2018). For example, solid quay walls and container stacks on shore can serve as windshields, breakwaters offer partial protection from waves, and terminals located along busy waterways may be subjected to frequent disturbances from passing vessels. Large-scale vessels in ports are typically moored at deep sea terminals close to deep water. As a result, these mooring locations are less sheltered, making them more exposed to environmental conditions than smaller ships (Schellin & Östergaard, 1995).

Moreover, the varying intensity and frequency of metocean aspects, including wind, short waves, and infragravity waves, across the globe result in significant differences in exposure levels at different geographical locations. This leads to a geographically diverse risk profile for port operability, including mooring. Areas of high operability risk are primarily concentrated around the southern capes, at exposed coastal locations, and within the "Roaring Forties", which is the region between 40 and 50 degrees south latitude known for frequent strong westerly winds. Locations on or near the equator generally experience a lower downtime risk compared to those further away. Inland seas tend to have lower risk as well due to reduced exposure to swell waves. Furthermore, the seasonal variations of the metocean factors significantly influence the risk profile throughout the year (Wiegel et al., 2021).

2.1.1. Wind

Wind acting on a vessel can be divided into two components: longitudinal wind, parallel to the longitudinal centerline of the ship, and transverse wind, perpendicular to the amidship line. The force induced by wind varies proportionally with the exposed area, as can be derived from the formulas for wind force and moment (K. Yan et al., 2023; OCIMF, 2018; Fernandes Ramos & Caprace, 2018; Ligteringen, 2022):

$$F_{\mathrm{Xw}} = \frac{1}{2} C_{\mathrm{Xw}} \rho_{\mathrm{a}} V_{\mathrm{w}}^2 A_{\mathrm{T}} \tag{2.1}$$

$$F_{\mathrm{Yw}} = \frac{1}{2} C_{\mathrm{Yw}} \rho_{\mathrm{a}} V_{\mathrm{w}}^2 A_{\mathrm{L}} \tag{2.2}$$

$$M_{\mathrm{XYw}} = \frac{1}{2} C_{\mathrm{XYw}} \rho_{\mathrm{a}} V_{\mathrm{w}}^2 A_{\mathrm{T}} L_{\mathrm{pp}} \tag{2.3}$$

Where

F_{Xw}	longitudinal wind force [N]
F_{Yw}	lateral wind force [N]
M_{XYw}	wind yaw moment [Nm]
C_{Xw}	longitudinal wind force coefficient [-]
C_{Yw}	lateral wind force coefficient [-]
C_{XYw}	wind yaw moment coefficient [-]
ρ_a	air density [kg/m^2]
V_w	wind speed [m/s]
A_T	transverse wind area [m^2]
A_L	longitudinal wind area [m^2]
L_{pp}	length between perpendiculars [m]

Following Equation 2.1, 2.2, 2.3, the wind forces and moment increase quadratically with wind velocity, as visualized in Figure 2.3.

Due to the reduced projected area of a vessel to longitudinal headwind compared to transverse beam wind, the resultant longitudinal wind force is of lower magnitude than the transverse force. Consequently, the resultant wind force acting on the vessel will deviate from the initial wind direction, except for pure head and beam winds (OCIMF, 2018; Schellin & Östergaard, 1995). This is illustrated in Figure 2.4.

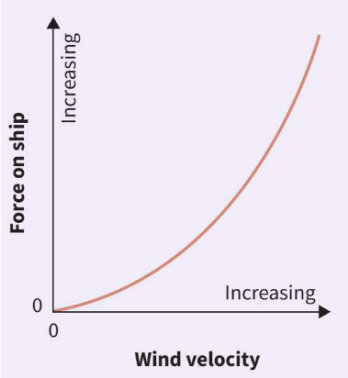

Figure 2.3: Wind force vs wind velocity (OCIMF, 2018)

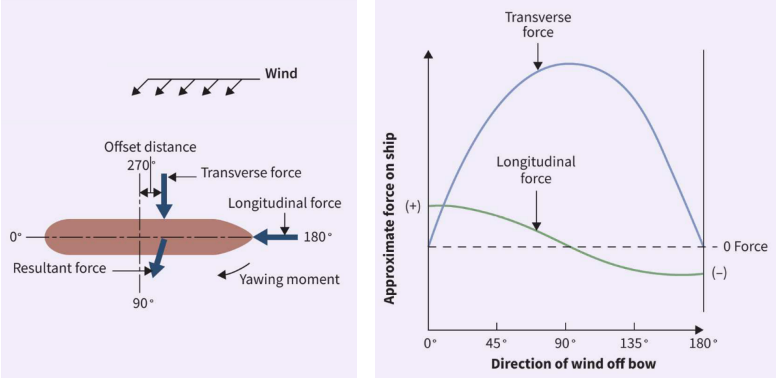

Figure 2.4: Wind forces on a ship (OCIMF, 2018)

The wind force coefficient, which indicates the magnitude of the wind forces acting on a ship, is determined through wind tunnel tests or numerical calculations (Ma et al., 2019; Schellin & Östergaard, 1995). The vessel's shape and the relative wind direction influence this coefficient (Molina-Sanchez et al., 2020). Further details can be found in Subsection 2.3.2.

Wind shielding impacts this wind force coefficient but is usually not directly accounted for. The effect of solid quays is viewed as a reduction of the vessel's lateral wind area. However, because of their unpredictable presence, wind shielding by large objects on the quay, such as buildings, cargo, and cranes, should not be taken into account according to IACS (2023), even though this simplifies the calculations and thereby affects the accuracy.

Besides wind shielding, ground-based obstacles in port areas, including cranes, container storage, other vessels, and buildings, significantly alter the wind profile, resulting in wind velocity and direction changes. Additionally, the average wind speed increases with elevation due to a reduction in the hindering effect of these barriers (Messe München, 2023).

2.1.2. Current

Current is the flow of water moving in a specific direction. Within ports, currents are generated by a variety of variables, including astronomical and meteorological tides, wind, industrial wastewater, and

fresh water influx from rivers. These currents can significantly impact moored vessels, causing ship motions with long periods, which results in increased tension in mooring lines (Molina-Sanchez et al., 2020).

The forces on vessels due to the current are proportional to the cross-sectional area under water and increase quadratically with the average current velocity. The force due current can be calculated using the following equation (Ligteringen, 2022; Natarajan & Ganapathy, 1995; OCIMF, 2018):

$$F_{Xc} = \frac{1}{2} C_{Xc} \rho_w V_c^2 L_{pp} T \tag{2.4}$$

$$F_{Yc} = \frac{1}{2} C_{Yc} \rho_w V_c^2 L_{pp} T \tag{2.5}$$

$$M_{XYc} = \frac{1}{2} C_{XYc} \rho_w V_c^2 L_{pp}^2 T \tag{2.6}$$

Where

F_{Xw}	longitudinal current force $[N]$
F_{Yw}	lateral current force $[N]$
M_{XYw}	current yaw moment $[Nm]$
C_{Xc}	longitudinal current force coefficient [-]
C_{Yc}	lateral current force coefficient [-]
C_{XYc}	wind yaw moment coefficient [-]
ρ_w	density of water $[kg/m^2]$
V_c	current velocity $[m/s]$
L_{pp}	length between perpendiculars $[m]$
T	draught of vessel $[m]$

The values of the current coefficients are based on model tank measurements (Schellin & Östergaard, 1995) and flume model tests (Gravesen, 2005). They depend on the direction of the wind relative to the moored vessel, on the under keel clearance (UKC), and on the shape of vessel's hull (Ligteringen, 2022). In Subsection 2.3.2 more details can be found.

Similarly to wind, the current speed and direction relative to the moored vessel determine the magnitude and direction of the force exerted on the vessel (OCIMF, 2018). A beam current generates a significantly larger force compared to a head current because of the greater area. Most terminals are aligned parallel to the current, minimizing this force (Schellin & Östergaard, 1995).

2.1.3. Waves

According to Van Koningsveld et al. (2023), motions of vessels are primarily the result of waves. Besides wave height, the wave period, and thereby the frequency, is of great influence. The response of a vessel to waves is significantly affected by its length. As visualized in Figure 2.5, large ships respond more to long waves, whereas small ships respond more to small waves.

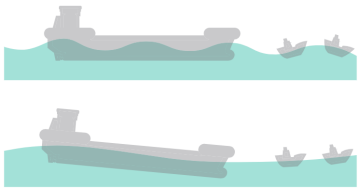

Figure 2.5: Response of vessels to waves depend on their length (Van Koningsveld et al., 2023)

Molina-Sanchez et al. (2020) identified three main wave types that contribute considerably to the motion of moored vessels: sea waves, swell waves, and infragravity waves. The natural frequency of vessel motions is of a similar order of magnitude as the frequencies of these wave types (Figure 2.6) (Van Koningsveld et al., 2023).

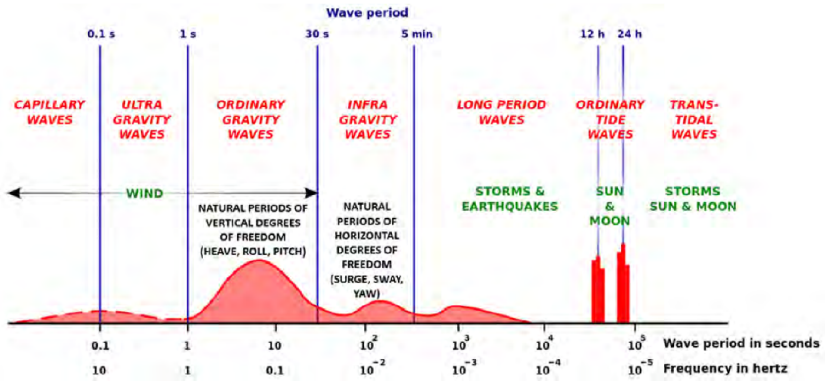

Figure 2.6: Wave periods and eigen periods of vessel motions at berth (Van Koningsveld et al., 2023)

Sea waves have a period of 4 to 10 seconds. They have short wavelengths and are induced by local wind. Their limited height and period are determined by the wind gust duration and the fetch, the unobstructed distance over which the wind blows. The natural periods of large-scale vessels are typically longer than the period of sea waves. Thus, they are not significantly affected by them (Molina-Sanchez et al., 2020). (Molina-Sanchez et al., 2020).

Swell waves have a period of 8 to 25 seconds and are caused by distant storms. Their periods may be close to the natural periods of moored ships, resulting in vertical vessel movements (heave, roll, pitch) (Molina-Sanchez et al., 2020).

Infragravity waves, also known as long waves, have a period of 30 to 300 seconds. They originate from three sources (Van Deyzen et al., 2015):

- Bound long waves generated by the grouping of swell waves
- Free long waves formed by the reflection of bound long waves after breaking on shallow water or induced by remote meteorological phenomena
- Harbor oscillations or seiches, which are standing waves associated with the natural resonance of a semi-enclosed body of water, like a harbor basin

Although the amplitudes of infragravity waves are generally low, they can cause large horizontal ship motions (surge, sway, yaw), especially for longer vessels (Molina-Sanchez et al., 2020; Van Deyzen et al., 2015). Besides, infragravity waves diffract around coastal defense structures (Wiegel et al., 2021), reducing the effectiveness of breakwaters which are designed to protect a port from waves and currents (Abdelwahab et al., 2024; Van Koningsveld et al., 2023; K. Yan et al., 2023).

2.1.4. Tide

Astronomical tides, driven by the gravitational attraction of the moon, sun, and other astral bodies, cause the periodic alternating fluctuations in seawater level (Puertos del Estado, 2007; NOAA, 2010b). These tidal movements of the water level in ports have a crucial effect on currents (Molina-Sanchez et al., 2020) as at high tide, water flows into ports, and ebb currents flow outward to sea during low tide (NOAA, 2010a).

In addition, the resulting changes in water level cause an alteration in ship elevation, affecting the relative position of moored vessels with respect to the port's mooring infrastructure (Natarajan & Ganapathy, 1995; Molina-Sanchez et al., 2020). This leads to fluctuations in mooring line tension, potentially resulting in slack lines that allow greater ship movements or excessive loads that induce the risk of parting lines. This issue must be addressed by managing the line length with the winch.

2.1.5. Passing ship traffic

In addition to natural phenomena, the passage of vessels in the proximity of a moored ship can generate significant peak loads in the mooring lines. When sailing, hydrodynamic pressure variations are developed along a ship's hull, inducing forces and moments on nearby moored vessels, referred to

as the passing ship effect. This interaction effect causes the moored ship to undergo motions (Van Zwijnsvoorde et al., 2018). Particularly passing vessels with deep draughts induce noticeable forces (Campbell et al., 2022).

Sreedevi and Nallayarasu (2023) stated that passing ship size, speed, water depth, and moored ship length are the passing ship interaction parameters.

Talstra and Bliek (2014) found the following basic properties that influence captive forces on moored ships due to other passing vessels: passing vessel speed, hull form of the moored vessel, lateral passing distance, under keel clearance of the moored vessel, moored vessel's displacement, and channel cross-section blocking ratio, which is the ratio between channel cross-section and ship cross-section area.

The model test study conducted by Remery (1974) showed the loads induced by a passing ship on a moored vessel increase proportionally with the square of the speed of the passing vessel and depend on the relative position of the vessels. These tests did not take into account the possible impact of the passing ship's propeller action.

2.2. Mooring system

The primary function of a mooring system is to ensure a vessel remains in a designated location during mooring (Wilson, 2003) by providing a secure connection between a vessel and a quay in port environments. The system is compromised of three main components, which can be seen in Figure 2.7: (1) the winch located on board the vessel which operates the mooring line, (2) the mooring line itself securing the vessel to shore, and lastly (3) the mooring point on the quay, known as a bollard (Broos et al., 2018). In addition to these three elements, other devices and structures are also involved during mooring. The mooring line leaves the ship through a fairlead, a guide mounted on deck. Besides, fenders are installed on the quay wall between the quay and the vessel to protect them both from damage (Roubos et al., 2024; PIANC, 2024; Broos et al., 2024; Eskenazi & Wang, 2015).

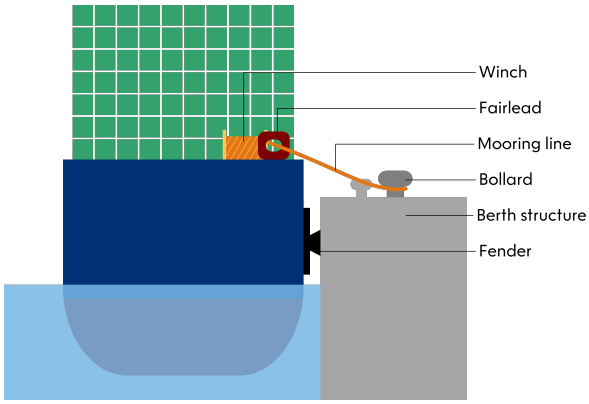

Figure 2.7: A mooring system consists of a winch onboard, mooring line, and berth structure with a mooring point and fender

The following subsections describe these main mooring system components, along with additional relevant elements, including different types of berth structures, fenders, and mooring points, the resulting mooring arrangement, and innovative alternative mooring systems.

2.2.1. Mooring lines

The purpose of mooring lines is to restrict ship movements. They are particularly effective in preventing movements in the horizontal plane (surging, swaying, and yawing) (Molina-Sanchez et al., 2020). The properties of mooring lines, including stiffness, are determined by material type, strand manufacturing technique, and rope construction (Lamont-Smith, 2019). Mooring lines in the same service, but preferably all lines, should be of the same type and have the same characteristics (IACS, 2023) to ensure the even distribution of mooring loads (Section 2.2).

Mooring lines are constructed from either synthetic ropes or steel wire. The five main used materials are steel, High Molecular PolyEthylene (HMPE), polyester, polypropylene, and nylon, listed from most stiff to most flexible (Van Zwijnsvoorde & Vantorre, 2017). Figure 2.8 shows these materials' load elongation curves of mooring lines. To absorb shock loads and facilitate line handling (Villa et al., 2018; OCIMF, 2018), synthetic rope tails can be added to stiff mooring lines such as wire ropes (Lamont-Smith, 2019) as can be seen in Figure 2.9.

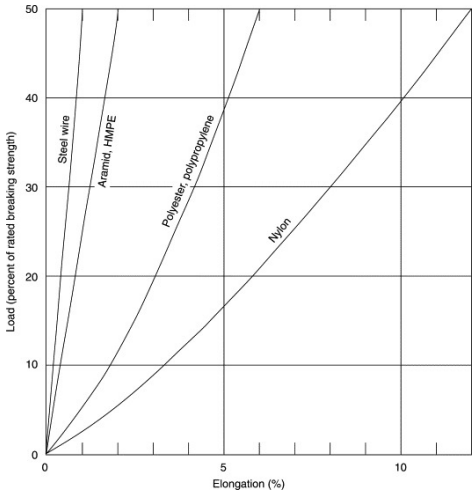

Figure 2.8: Typical load-elongation profiles for various ropes from 0 to 50% of MBL (McKenna et al., 2004)

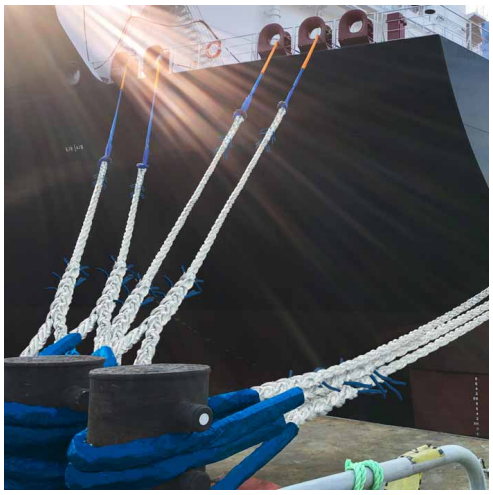

Figure 2.9: White mooring tails are connected to blue mooring lines (Samson Rope, 2024)

Steel wire ropes consist of steel strands laid around a steel or fiber core as illustrated in Figure 2.10 (OCIMF, 2018; US Department of Defense, 2020; Prasad et al., 2023). They exhibit high durability due to their high resistance to mechanical damage. However, their susceptibility to corrosion requires frequent maintenance, and their high weight poses handling challenges. Synthetic lines are manufac-

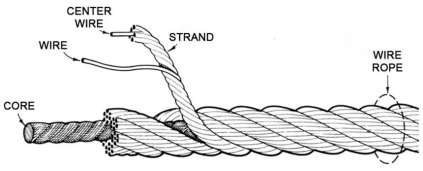

]

Figure 2.10: Wire rope and its components (Prasad et al., 2023)

tured in various constructions and arrangements (Figure 2.11) and can be jacketed at rope or strand level. An advantage of these lines over wire ropes is that they are relatively easy to handle by staff, and some types have lower stiffness (US Department of Defense, 2020; OCIMF, 2018).

IACS (2023) recommends a required minimum Minimal Breaking Load (MBL) of mooring lines based on the vessels lateral area. The ship fittings are designed using this theoretical Ship Design MBL (MBL_{SD}) (Broos et al., 2024). However, IMO (2020) outlines that the number and strength requirements for mooring lines depend on the vessel's Equipment Number (EN). The formula of EN is based on the ship's area below the water surface, the wind area in longitudinal direction defined by the beam and height from the waterline, and the lateral projected area subjected to wind (Oh et al., 2020). For vessels with EN $\leq$ 2000 are the number of mooring lines and required MBL defined by the EN. Large-scale vessels with EN > 2000, though, have these values determined solely by their side projected area:

$$MBL_{SD} = 0.1A_{side} + 350 \tag{2.7}$$

$$n = 8.3 \cdot 10^{-4} A_{side} + 6 \tag{2.8}$$

Where
MBL_{SD} Ship Design MBL [kN]

n general total number of mooring lines
A_{side} side projected area [m^2]

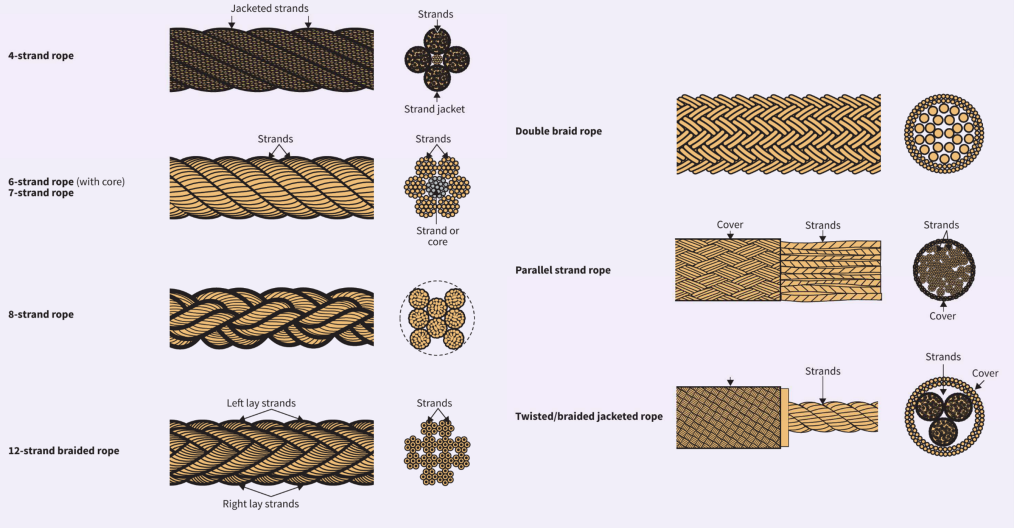

Figure 2.11: Constructions of synthetic fiber lines (OCIMF, 2018)

Both prototype and experimental model tests emphasize the importance of maintaining taut mooring lines (Gravesen, 2005). Pretension in the mooring lines by the winches has been observed to result in reduced vessel motions and forces, as seen in Figure 2.12. Gourlay (2017) further elaborates that higher pretension levels cause the vessel to be held against the fenders, leading to increased friction force and more energy dissipation. This contributes to more damping and lower motions, which result in lower peak loads in the mooring lines. However, excessive pretensioning diminishes the efficacy of the mooring system (OCIMF, 2018).

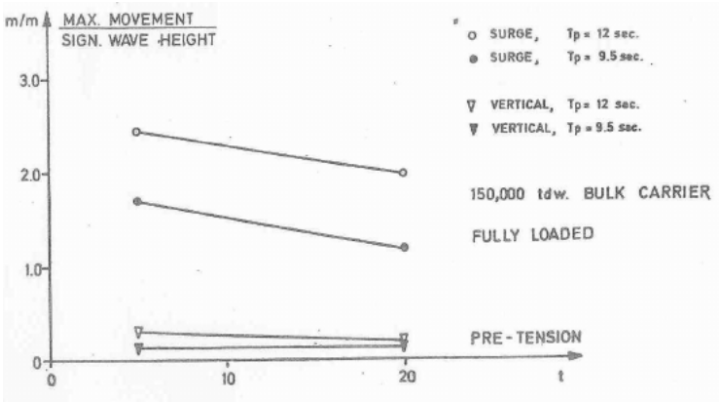

Figure 2.12: Effect of pretension on the movement of moored vessels due to waves (Gravesen, 2005)

When the mooring lines are attached to the mooring points on shore, an initial load, the so-called pretension, is applied to the lines by the winch. This establishes a stable initial condition for moored vessels. According to literature, the pretension of mooring lines typically ranges from 5% to 10% of the MBL (Lamont-Smith, 2019; Barros & Mazzilli, 2018; M. Yan et al., 2023; Van Zwijnsvoorde et al., 2018). However, the actual practice of mooring line pretensioning remains unclear, as it is not possible to directly determine the exact pretension level from the winch.

If the tension in the mooring lines exceeds the MBL, there is a risk of line failure. Parting of a mooring line may result in so-called snap-back: the broken ends recoil immediately after the line breaks. This phenomenon occurs because the potential energy stored in the line, which is related to the area under the plotted load-elongation curve (see Figure 2.8), is transferred into kinetic energy (Campbell et al.,

2022). The ends are thereby accelerated for longer than the rest of the line (OCIMF, 2018). Lines with lower stiffness can have more severe snap-backs, due to their increased amount of stored energy compared to those with high stiffness. Snap-backs can result in severe injury or fatalities among crew members, and damage to the ship or berth.

In order to mitigate these risks, various protective measures have been implemented. Physical mooring line barriers of all sorts (Campbell et al., 2022) are installed to provide some protection. Furthermore, Wilhelmsen (2022) developed a snap-back arrestor. This is a core of rope integrated into the mooring line. It serves as an energy absorber and lowers risks significantly, as seen in the pictures of the snapping of mooring lines in Figure 2.13.

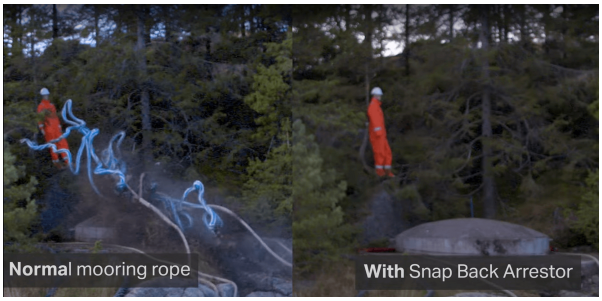

Figure 2.13: Comparison of mooring line snap-back with and without a snap-back arrestor. A regular mooring line recoils violently after breaking, while the mooring line equipped with a snap-back arrestor demonstrates a substantial reduction in recoil distance (Wilhelmsen, 2022).

Additionally, hydraulic shore tensioning systems, which will be discussed in more detail in Subsection 2.2.7, can prevent line failure by preventing the lines from reaching their MBL. It is not recommended to mark snap-back zones on deck as this creates a false sense of safety for personnel outside these areas (OCIMF, 2018; UK P&I, 2009). On board, the crew should protect the line from performance degrading factors such as chafing, UV exposure, induced twists in the line, and exposure to industrial chemicals.

2.2.2. Winch

Mooring winches are installed on deck (Figure 2.14, Figure 2.15) and handle the mooring line (Broos et al., 2018) by rotating its drum, thereby releasing or retrieving line (Villa et al., 2018; Couce et al., 2015). Proper line tending is necessary to accommodate changes in ship elevation due to tidal fluctuations in water level as stated in Subsection 2.1.4 or vessel loading operations (Villa et al., 2018). Winches typically use electric power, or more commonly, hydraulic or pneumatic power (Villa et al., 2018).

Mooring winches are supposed to apply a pretension load to the mooring lines, effectively pulling the vessel to the quay against the fenders. This decreases ship motions and mooring line loads due to fender friction and the energy absorption capacity of both fenders and lines (Rosa-Santos et al., 2014).

Conventional winches rely on manual operation, requiring crew intervention to regularly monitor and tend mooring tensions (Villa et al., 2018; Couce et al., 2015). Conversely, auto-tension winches can be employed in auto-tension mode in moderate conditions (Broos et al., 2018; Villa et al., 2018). In this mode, the winch automatically tends the mooring line to maintain a preset tension (Villa et al., 2018; Couce et al., 2015) and has a pull capability of 33% of the MBL_{SD} (IACS, 2023). Under severe environmental conditions, all winches can be placed on their brakes, increasing the holding capacity.

According to OCIMF (2018), the Brake Holding Capacity (BHC) is 60% of the MBL_{SD}, but this is not a certified value (Broos et al., 2018; De Gijt & Broeken, 2013). When the BHC is reached, the winch should start rendering line (Broos et al., 2024; OCIMF, 2018).

Winches can have a single drum into which the mooring line is wound, resulting in a varying linear speed across different layers. The alternative is a split drum wherein a drum separator divides the tension drum from the storage drum. In this configuration, the mooring line is reeled into one layer on

Figure 2.14: Winch with a split drum (Wilhelmsen, 2023)

Figure 2.15: Forecastle deck with mooring lines and winches (Broos et al., 2018)

the tension drum, providing a constant speed, while the remaining line is stored on the storage drum (Villa et al., 2018). Ideally, winches can to store the entire length of the mooring line.

2.2.3. Berth structure

Ships can moor at berth structures in ports that are equipped with mooring points. These structures are the physical interface between land and water (De Gijt & Broeken, 2018) and facilitate the loading and unloading of cargo or boarding and disembarking of passengers (Puertos del Estado, 2019).

The type of berth structure significantly influences vessel motions (Gravesen, 2005). Furthermore, the height of these structures affects the length of the mooring lines and their angles and, thus, the line forces and moored ship motion.

2.2.3.1. Quay wall

Quay walls are earth-retaining structures and facilitate cargo handling by cranes or other moving heavy equipment (De Gijt & Broeken, 2013). Most container transshipment operations are conducted on quay walls (De Gijt & Broeken, 2018). Their functions (De Gijt & Broeken, 2013) are twofold: firstly, to provide bearing capacity to carry the loads imposed by the freight, stored goods, and transshipment equipment; and secondly, to retain the soil for the area behind the quay (Ligteringen, 2022). Additionally, they may function as water retaining walls.

The four basic quay wall types are illustrated in Figure 2.16 (De Gijt & Broeken, 2013):

(a) Gravity walls

(b) Sheet pile walls

(c) Structures with relieving platforms

(d) Open berth quays

Vertical solid quays lower the ship response due to increased damping and added mass and can shield the moored vessel from wind compared to open quay structures (IACS, 2023).

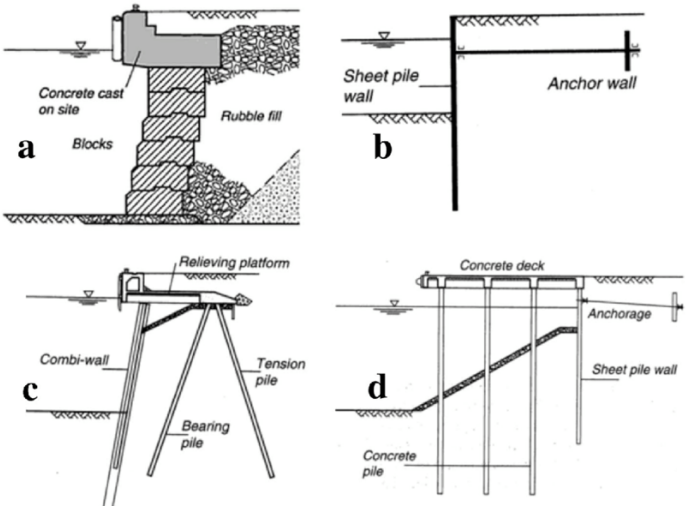

Figure 2.16: Classification of quay walls (Nguyen et al., 2021): (a) gravity wall, (b) sheet pile wall, (c) structures with relieving platform, (d) open berth quay

2.2.3.2. Jetty

Jetties are commonly used for the storage and transshipment of light cargo and RoRo traffic. These structures can either be fixed, typically with an open design as in Figure 2.17, or floating platforms. Fixed jetties feature a deck supported by a pile foundation (De Gijt & Broeken, 2018). The deck is usually closed to prevent cargo spillage in the surrounding water. Jetties may be isolated or connected to shore through gangways or bridges or an extension of the structure (Puertos del Estado, 2019).

Figure 2.17: T-shaped jetty in Port of Rotterdam (Donker, 2018)

Liquid bulk terminals typically do not require heavy cranes due to pipeline transportation. This allows for using jetties as berthing structures, representing a more cost-effective alternative to quay walls. Besides, jetties facilitate the positioning of vessels away from other terminal operations, making them particularly suitable for LNG and LPG terminals with high safety standards (Van Koningsveld et al., 2023).

2.2.3.3. Dolphin

Mooring dolphins (Figure 2.18) are isolated offshore structures (Puertos del Estado, 2019). They can be positioned to form a berthing line or incorporated into mixed mooring solutions with jetties. Tankers are frequently moored at a combination of a jetty and mooring dolphins.

2.2.3.4. Buoy

Mooring buoys (Sijberden, 2006) are floating mooring structures (Puertos del Estado, 2019) fitted with eyes for connecting the mooring line (Figure 2.19). They are attached to an anchor system in the seabed by anchor chains. At low tide, the slack in the anchor chain increases, resulting in a larger range of movement for the moored vessel.

Figure 2.18: Mooring dolphins in the Port of Rotterdam (CROW, 2021)

Figure 2.19: Mooring buoys in Port of Rotterdam (Port of Rotterdam, 2015)

2.2.4. Fenders

Fenders are installed on marine structures as an interface. They absorb the kinetic energy of approaching or moored vessels and transmit the forces to the structure. This prevents damage to both the vessel and the mooring structure (Eskenazi & Wang, 2015; Roubos et al., 2024; PIANC, 2024).

The load-deflection curve of a fender depicts the fender deflection s and the corresponding reaction force F_R exerted by the fender as shown in the general curve in Figure 2.20. The area beneath the curve shows the absorbed energy E_f, and the energy absorption capacity is achieved at the maximum deflection s_{max} (HTG, 2015).

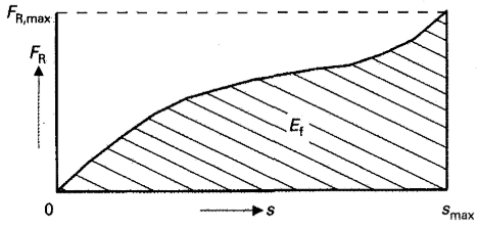

Figure 2.20: Load-deflection curve for a fender (HTG, 2015)

Fenders are categorized into two main groups according to their primary function (PIANC, 2024). The first category of fenders transmits impact forces directly to the supporting structure with minimal energy absorption. The second category absorbs the impact energy and is further separated into two subgroups: buckling and sideloaded fenders.

Buckling fenders consist of cone, cell, element, or leg fenders (Figure 2.21) and are typically equipped with a fender panel. They offer substantially greater energy absorption capacity than sideloaded fenders, as indicated by the load-deflection curve shown in Figure 2.22.

(a) Cone fender **(b)** Cell fender **(c)** Element or leg fender

Figure 2.21: Buckling fenders (PIANC, 2024)

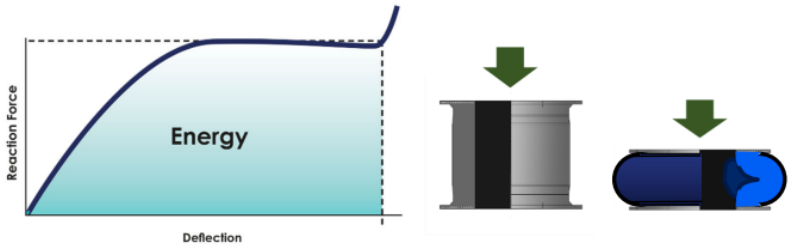

Figure 2.22: Typical indicative load deflection curve of buckling fenders (PIANC, 2024)

Sideloaded fenders include cylindrical, pneumatic, and foam fenders (Figure 2.23). Their fender deflection and reaction force increase almost linearly, as shown in the load-deflection curve in Figure 2.24.

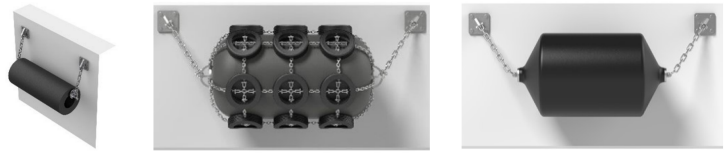

(a) Cylindrical fender **(b)** Pneumatic fender **(c)** Foam fender

Figure 2.23: Sideloaded fenders (PIANC, 2024)

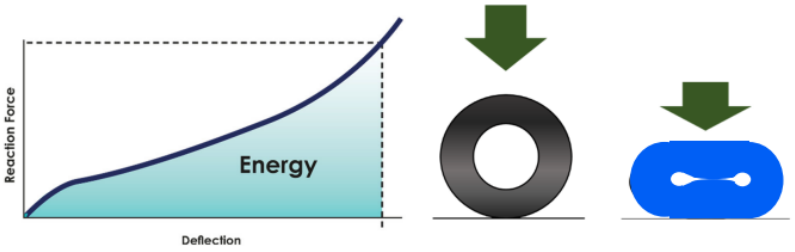

Figure 2.24: Typical indicative load deflection curve of sideloaded fenders (PIANC, 2024)

2.2.5. Mooring point

Mooring points are attachment points for mooring lines and are installed on berth structures.

2.2.5.1. Bollard

Bollards are fixed mooring points installed on berth structures. They are typically composed of cast iron, nodular cast iron, or cast steel (Sijberden, 2006). They consist of a shaft with a thicker head to prevent line slippage, particularly with large vertical angles, and a base plate that is anchored in the foundation. As illustrated in Figure 2.25, multiple bollard types exist. According to HTG (2015), bollards are characterized by their reliability and low maintenance requirements.

At least two people are required to handle the fastening and releasing of mooring lines to and from bollards, and this can only be done when the line is slack (OCIMF, 2018). Multiple mooring lines can be secured to one bollard. So, a bollard's Safe Working Load (SWL) should be higher than the forces in the lines (Broos et al., 2018).

According to the EAU guidelines (HTG, 2015), the displacement of the ship determines a bollard's required pull force capacity. However, this approach does not account for the wind-induced forces on the vessel, which are related to the windage area (Broos et al., 2018). Following BS 6349-4 (2014),

the maximum mooring loads should be calculated for vessels larger than 20,000t displacement to determine the nominal bollard loading.

Figure 2.25: Tricorn, T-head, K-head, Quad-head, and T-horn bollard (left to right) (QuayQuip Technical Solutions BV, 2019)

Figure 2.26: Quick Release Hook (QRH) arrangement on a mooring dolphin in Amsterdam (Straatman, 2020)

2.2.5.2. Quick release hook

A Quick Release Hook (QRH) (Figure 2.26) is a common mooring point as well and is designed to accommodate only one mooring line. A maximum of five hooks can be installed on a single base (OCIMF, 2018). Unlike bollards, they allow for rapid and easy release of mooring lines even when under tension as they are hydraulically operated (Sijberden, 2006). This reduces line handling effort during berthing (OCIMF, 2018) and is helpful in emergency situations to limit damage to port infrastructure and the environment, making them particularly crucial for berths handling hazardous cargo (HTG, 2015). QRHs are typically installed on mooring dolphins and commonly used for mooring tankers (OCIMF, 2018).

2.2.6. Mooring arrangement

The mooring arrangement refers to the geometrical configuration of mooring lines between vessel and berth, and depends on the vessel characteristics and the port infrastructure.

The layout typically consists of spring, breast, and head and stern lines for large-scale vessels as illustrated in Figure 2.27 (Villa et al., 2018; OCIMF, 2018; IACS, 2023). Spring lines are orientated parallel to the amidships line, preventing longitudinal surge motions, while breast lines ideally lead perpendicularly ashore and are positioned at stern and bow, restraining sway movement in an off-berth direction. The head and stern lines are deployed diagonally, restricting motions in off-berth and in the fore or aft direction. The pattern in which the lines are deployed influences the load distribution along these lines and is the responsibility of the vessel's captain.

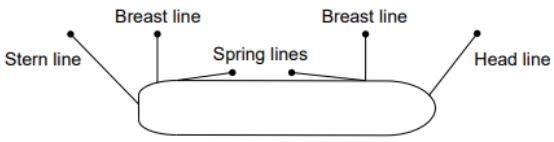

Figure 2.27: Vessels are often moored using spring, breast, head, and stern lines (IACS, 2023)

While preferably all deployed lines should have similar characteristics, mooring lines used in the same service absolutely are required to be of the same length and type and have the same characteristics (OCIMF, 2018; IACS, 2023). This ensures that forces are distributed evenly among them. In addition, the vertical angle of the mooring line relative to the pier deck, and the horizontal angle relative to the ship's side should be minimized OCIMF (2018).

The combination of a jetty and mooring dolphins usually provides a better mooring pattern than quays, which are equipped with bollards arranged linearly along the quay edge due to crane rail requirements.

The following factors determine the specific mooring arrangement of a vessel:

- Position and amount of mooring points
- Amount of mooring lines
- Position of fairleads, which guide mooring lines from the vessel to shore
- Ship's elevation
- Presence of alternative mooring techniques (Subsection 2.2.7)

2.2.7. Alternative mooring techniques

Besides the conventional mooring system involving lines and winches, which is most commonly used for mooring (Kuzu & Arslan, 2017), alternative innovative systems have been developed to enhance safety and efficiency.

2.2.7.1. Vacuum mooring

Vacuum mooring systems offer an alternative to conventional mooring lines (Sijberden, 2006; Kołakowski et al., 2023). Vacuum pads are attached directly to the flat hull of a vessel and act as hydraulically operated suction cups. The system does not require any modifications to the mooring vessels (Abdelwahab et al., 2024). MoorMaster (Cavotec, 2024) (Figure 2.28) and AutoMoor (Trelleborg, 2024) are both shore-based automated vacuum systems which minimize human error through automation and reduce personnel involvement. Ship motions are restricted in the horizontal plane (surge, sway, yaw) (Abdelwahab et al., 2024) by the dynamic hydraulic computer control (Van den Boom et al., 2014; BS 6349-4, 2014) and the speed of the mooring operation is much higher compared to using mooring lines (K. Yan et al., 2022). However, the system is limited by the thickness of the hull, maximum fender force, and the restricted movement of the system (K. Yan et al., 2022), and it has a high maintenance level, especially in a saline environment of seaports (De Bont et al., 2010). Vacuum mooring is a widely accepted technology with applications on various ship types, including ferries, general cargo ships, large container ships, and bulk ships (Jørgensen et al., 2023).

Figure 2.28: MoorMaster units in Port of Salalah, Oman (Cavotec, 2020)

Figure 2.29: Magnetic mooring on ferry in London (Christy, 2018)

2.2.7.2. Magnetic mooring

Magnetic mooring systems (Sijberden, 2006; Kuzu & Arslan, 2017; Abdelwahab et al., 2024; Kołakowski et al., 2023) use magnetic pads connected to hydraulic arms replacing mooring lines to dampen the ship motions actively. An electric current generates the magnetic field. The system requires hull modifications in the form of integrated plates with which the pads can interact as seen with the Docklock (Van Reenen, 2013), an automatic magnetic mooring system on a ferry in London (Jørgensen et al., 2023) which is installed on the quayside (Abdelwahab et al., 2024) (Figure 2.29). Using magnetic mooring systems enhances the efficiency compared to conventional mooring as it reduces the time required for berthing operations (Kołakowski et al., 2023). In contrast to vacuum-based mooring, this technology is not widely operational, partly due to the complex integration with existing ship designs.

2.2.7.3. Hydraulic mooring line tensioning

ShoreTension (Van der Burg, 2011) is a widely used hydraulic, dynamically controlled (Van den Boom et al., 2014) mooring system in ports around the world (ShoreTension, 2024). The system dampens ship motions in severe conditions by automatically managing mooring line tension without exceeding the MBL, thereby preventing it from breaking (Abdelwahab et al., 2024; Kołakowski et al., 2023). It

does not require an external energy source, except to bring the mechanism to the correct setting. The unit consists of a hydraulic cylinder with a 3-meter long piston, one end of which is fixed to a quay bollard, and the moving end of which is connected to a high-strength mooring line which is guided to the moored vessel by a second bollard (Figure 2.30). During peak loads, the mechanism pays out the line.

Onboard auto-tension winches can prevent mooring lines from breaking as well by managing the line tension. However, these winches require considerable of energy and cannot provide the same benefits as a ShoreTension unit (Kołakowski et al., 2023).

Figure 2.30: ShoreTension unit (VNO-NCW Regio Rotterdam, 2023)

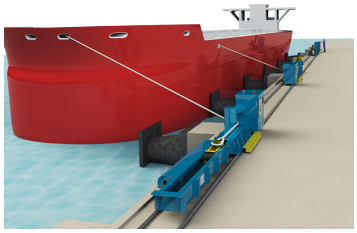

Figure 2.31: DynaMoor unit (Trelleborg, 2021b)

DynaMoor (Trelleborg, 2021a) is a shore-based constant tensioning system similar to ShoreTension. It is a linear unit anchored independently at the quay edge (Figure 2.31). The ship's mooring line is connected to the system's quick release hook via the built-in fairlead, which controls the direction and angle of the mooring line and reduces rope friction. The electronically controlled hydraulic damper manages the line tension, reducing vessel movement and minimizing snap-back zones on the quay.

These hydraulic mooring line tensioning devices can be easily integrated in the conventional mooring systems with lines and ropes, directly enhancing safety and reducing vessel motion.

2.3. Ship characteristics

The ship characteristics influence the environmental forces' impact and are a key factor characterizing mooring. They include the dimensions and load state, which are illustrated in Figure 2.32, and the current and wind coefficients of the moored vessel.

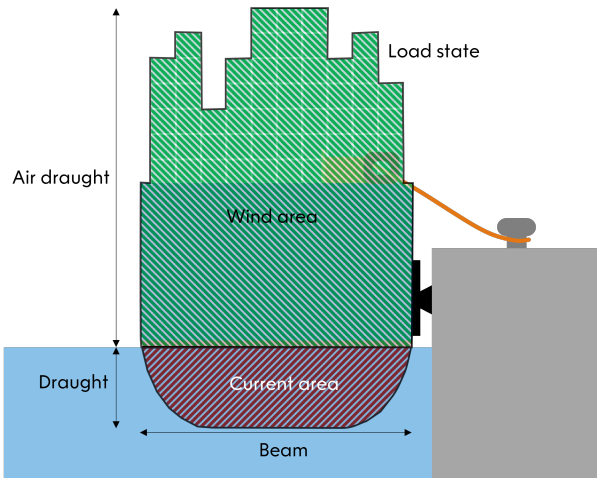

Figure 2.32: The ship characteristics include the load state and the dimensions of the moored vessel

2.3.1. Dimensions and load state

As outlined in Subsection 2.2.1, the equipment number (EN) defined by IMO (2020) depends on the vessel dimensions and determines the MBL_{SD} of the mooring lines. All shipboard fittings and equipment are designed using this particular value of MBL_{SD}. Thus, the capacity of the mooring lines and winches is directly related to the vessel size.

The size of a vessel influences its susceptibility to waves. As already stated in Subsection 2.1.3, larger ships are more responsive to long waves with low frequencies, whereas smaller ships are more sensitive to short waves. This phenomenon is attributed to the natural frequency of vessels, which can be close to the frequencies of those specific waves.

The load condition of a vessel affects the draught and air draught. When fully loaded, a vessel typically sits deeper in the water due to increased weight, consequently reducing the exposed area above the waterline. This principle applies to RoRo vessels and gas tankers, where the overall dimensions remain constant regardless of the loading state. Conversely, fully loaded container ships present a significantly larger projected area than empty ones due to the substantial proportion of the containers stacked above the deck (PIANC, 2024). Furthermore, according to Blendermann (1997), the configuration of containers affects wind force. Variations in bay height and the random stacking of containers on the deck contribute to increased wind force.

A vessel's air draft, the vertical distance between the waterline and the highest point, including deck cargo, determines the projected area exposed to wind, along with the vessel's length and beam. Vessels with large air drafts are more susceptible to wind due to their increased windage area (Molina-Sanchez et al., 2020), as wind forces are directly proportional to the exposed area as can be read in Subsection 2.1.1.

The draught of a ship is defined as the vertical distance between the waterline and the lowest point of the hull (Barden, 2018) and changes with the weight a vessel carries. A fully laden cargo vessel has a large water displacement, resulting in a deeper draught. The draught of a vessel determines the UKC, which both influences the impact of current (Subsection 2.1.2) and the effect of passing vessels (Subsection 2.1.5).

2.3.2. Force coefficients

2.3.2.1. Wind coefficients

Wind coefficients determine the impact of wind on moored vessels. They depend on relative wind direction and the vessel's shape (Molina-Sanchez et al., 2020) as mentioned in Subsection 2.1.1.

The value varies according to ship type, size, and loading condition (IACS, 2023), but wind coefficients from similar vessel shapes can be interchangeably used for wind calculations. Wind force and moment coefficients of a tanker are provided in Figure 2.33 according to OCIMF (2018) and based on data from wind tunnel tests.

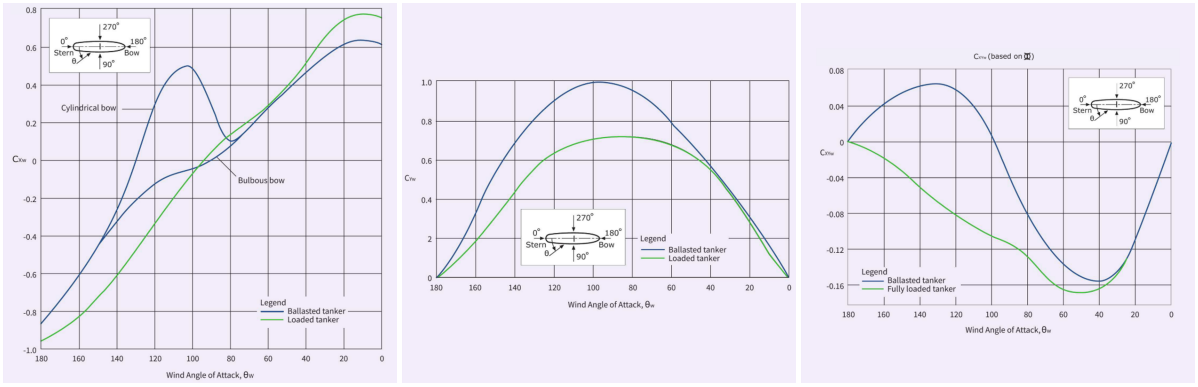

(a) Longitudinal wind coefficients C_{Xw} **(b)** Lateral wind coefficients C_{Yw} **(c)** Wind yaw moment coefficients C_{XYw}

Figure 2.33: Wind coefficients of tankers (OCIMF, 2018)

2.3.2.2. Current coefficients

The current coefficients of vessels are based on model tank measurements (Schellin & Östergaard, 1995) and flume model tests (Gravesen, 2005). The values are influenced by the hull profile (Molina-Sanchez et al., 2020), UKC (OCIMF, 2018), and the relative wind direction as stated in Subsection 2.1.2.

The UKC, the distance between the ship's keel and seabed, has the largest influence on current coefficients (OCIMF, 2018), as a small UKC amplifies the effect of current (Andrés & Piniella, 2017). The current coefficients of tankers at loaded draught are shown in Figure 2.34. For tankers moored in shallow water, a proportionately larger volume of water passes around the tanker than under due to the blockage effect. The lateral current coefficients for a water depth to draught ratio (Wd/T) of 1.05 are thereby approximately three times larger than coefficients for (Wd/T) of 3.0 (OCIMF, 2018).

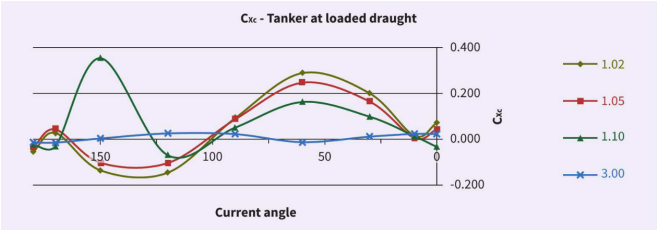

(a) Longitudinal current coefficients C_{Xc}

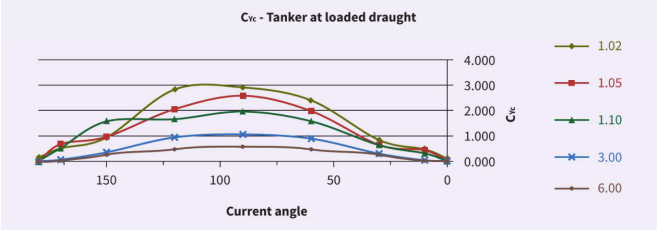

(b) Lateral current coefficients C_{Yc}

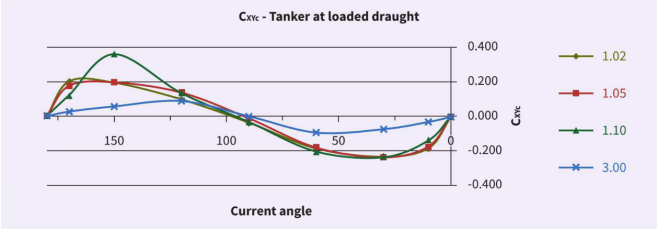

(c) Current yaw moment coefficients C_{XYc}

Figure 2.34: Current coefficients of tankers at loaded draught for different Wd/T (OCIMF, 2018)

2.4. Conclusion

This chapter answers SQ1: *What are the key aspects characterizing the mooring of large-scale vessels in port areas?*

Figure 2.35 provides an overview of the key aspects of mooring covered in this chapter.

Environmental conditions induce external forces on a moored vessel, the mooring system restricts the movement of the vessel, and the ship characteristics determine the impact of these forces and define the capacity of the mooring equipment on board.

It is essential to understand these key aspects to ensure the safety and efficiency of mooring operations.

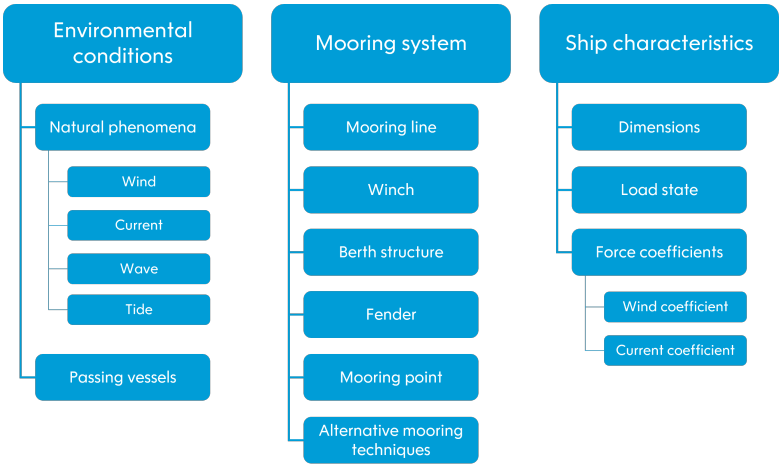

Figure 2.35: Overview of the key aspects that characterize the mooring of large-scale vessels

3

Mooring force prediction using DMA

With the increasing scale of vessel sizes, accurate tools to evaluate mooring forces and vessel motions have become essential to ensure mooring safety. Dynamic Mooring Analysis (DMA) offers a physics-based computational approach to simulate the responses of moored vessels under time-varying loads.

This chapter answers SQ2: *What are the fundamental principles and key considerations of Dynamic Mooring Analysis for predicting mooring line forces of large-scale vessels in port areas?*

DMA is introduced in Section 3.1 and Section 3.2. Section 3.3 outlines the necessary input files, the resulting output files, and model assumptions of the DMA package aNySIM. Section 3.4 describes some practical use cases of DMA.

3.1. Numerical simulation

Computational simulation is a model-based technique that can be used to estimate ship responses under various environmental conditions by numerically solving the equations of motions for moored vessels. This method is widely used and often involves a series of coupled models (Romano-Moreno et al., 2022). The availability of numerical models has led to a decline in the use of physical modeling (Gaythwaite, 2014).

Numerical simulation offers several advantages in terms of costs, flexibility, and time consumption compared to physical model testing. However, its results can be limited by the complexity of multivariate and nonlinear modeling (Liu et al., 2020; Taveira Pinto et al., 2008). Additionally, the requirement for a wide range of input parameters often leads to the use of hypothetical or standardized values, introducing uncertainty into the results (Romano-Moreno et al., 2023).

3.2. Dynamic Mooring Analysis

A DMA is a numerical simulation model used to evaluate the behavior of moored vessels under various environmental conditions. DMA simulations are typically conducted in the time domain, enabling the modeling of nonlinear effects (Van Koningsveld et al., 2023).

The input data of for a DMA includes environmental conditions, vessel characteristics, and mooring configuration. Environmental conditions consist of a combination of wind, waves, and currents. Vessel characteristics include dimensions, mass properties, and coefficients for calculating forces and moments due to environmental conditions. Mooring configuration encompasses mooring line properties and deployed pattern, fender characteristics, and additional motion-damping devices (Van Koningsveld et al., 2023).

Several (commercial) DMA packages are available and employed in studies: Quaysim (De Bont et al., 2010; Van der Molen et al., 2016), Vlugmoor (Van Zwijnsvoorde & Vantorre, 2017), MoorMotions (Gourlay, 2017, 2023, 2019a, 2019b), SHIP-MOORINGS (Romano-Moreno et al., 2023; Sáenz et al., 2023), MIKE 21 Mooring Analysis (M. Yan et al., 2023), Optimoor (Sundar et al., 2019), TERMSIM (Weiler et al., 2009).

For this study, the DMA software package aNySIM is used. This software was developed by Mar-

itime Research Institute the Netherlands (MARIN) and is used by Haskoning, a leading engineering consultancy. aNySIM is well-suited for modeling complex mooring scenarios involving nonlinearities in mooring systems and vessel behavior.

3.3. aNySIM software

The DMA software aNySIM mathematically models the response of moored vessels subject to time-varying environmental forces such as wind, waves, and currents. It is capable of simulating moored vessels at various structures, including quays, jetties, or alongside other ships.

It predicts mooring lines forces, fender forces, and ship motions in 6 DoF by solving the equation of motion in Equation 3.1 (Bunnik & Veldman, 2010) in the time domain, accounting for nonlinear effects in fenders and mooring lines (Van Deyzen, Nguyen, & Eggermont, 2024; Cross & Van Deyzen, 2023; Van Deyzen, Nguyen, & Van de Sande, 2024; Eggermont & Van Deyzen, 2023).

$$\sum_{j=1}^{6}(M_{kj}+m_{kj})\ddot{x}_j+\int_{-\infty}^{t}R_{kj}(t-\tau)\dot{x}_j(t-\tau)d\tau+C_{kj}x_j=F_k(t) \tag{3.1}$$

Where

k, j	indices representing the six degrees of freedom: surge, sway, heave, roll, pitch, and yaw
x_j	displacement in motion mode j
$\dot{x}_j$	velocity in motion mode j
$\ddot{x}_j$	acceleration in motion mode j
$F_k(t)$	external force in motion mode k
M_{kj}	solid inertia matrix
m_{kj}	added inertia matrix
R_{kj}	matrix of retardation functions
C_{kj}	matrix of hydrostatic restoring forces

Typically, the simulation length of each run is set at 3.5 hours. However, the statistical analysis of maxima and minima only includes the last 3 hours to ensure a representative vessel response, excluding the initial 30 minutes due to transient effects (Schweter et al., 2023; Van Deyzen, Nguyen, & Eggermont, 2024; Van Deyzen, Nguyen, & Van de Sande, 2024; Naciri et al., 2007; Fleer et al., 2024; Cross & Van Deyzen, 2023). The resulting 3-hour simulation duration was determined to provide a reliable representation of wind patterns within the modeled time frame (Eggermont, 2024).
A single run requires approximately 30 seconds of computational time.

3.3.1. Model input description

aNySIM requires three key inputs (MARIN, 2022):

- XMF file: Defines simulation setup, environmental forcing, body dynamics, and output parameters
- Fender mesh: Specifies the shape and layout of the contact surface used to model fender interactions (MARIN, 2021)
- Hyd file: Contains hydrodynamic properties

3.3.1.1. XMF

The DMA model aNySIM is constructed on the Extensible Modelling Framework (XMF), a C++ software toolkit developed by MARIN to facilitate time-domain simulations (MARIN, 2022). The XMF file serves as the main input file and defines the overall computational model. It is a structured text file and provides a hierarchical representation of the simulation environment, the simulation setup, and the system components through nodes and properties as visualized in Figure 3.1.

An XMF file typically contains information on global environmental conditions such as wind, waves, and current characteristics, along with references to global databases like the hydrodynamic database. The integrator object performs the actual time-domain simulation and includes sub-objects representing gravity, the fenders, the mooring lines, and the body involved. The body is further described by parameters such as the vessel's dimensions, mass, and draught, wind and current coefficients, subjected

areas, and linear and quadratic damping. Lastly, the timetrace logger object generates the output files, specifies the start-up transient time, and defines the output parameters (Zhi, 2013; MARIN, 2021).

The simulation process begins by reading the model from the XMF input file, loading the dynamic content libraries, and subsequently running the simulation (MARIN, 2022).

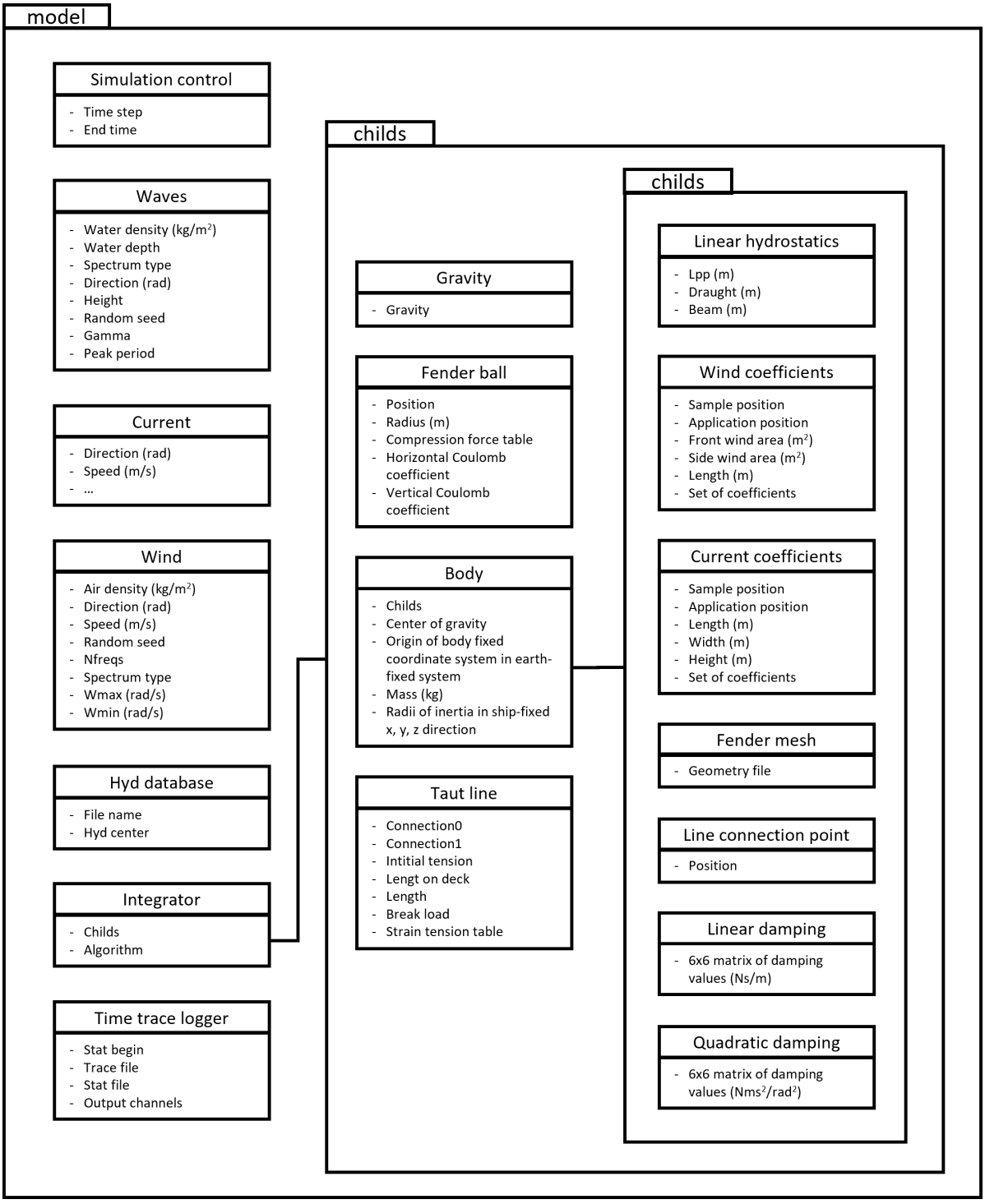

Figure 3.1: Overview of the nested structure of the XMF file of a vessel moored to a berth under waves, current, and wind, based on MARIN (2021)

3.3.1.2. Fender mesh
The fender mesh is provided as an .obj file and describes the geometry of the fender contact plane using a polygons, which can represent convex, concave, or non-contiguous surfaces (MARIN, 2021).

3.3.1.3. Hyd file
The Hyd file contains the hydrodynamic database and defines information about the hydrodynamic response and wave excitation of the floating body, including hydromechanic forces such as added mass, damping, and first- and second-order wave forces. It is computed using MARIN's 3D diffraction theory software DIFFRAC, although other diffraction software can also be used (Eggermont & Van Deyzen, 2023; Schweter et al., 2023; MARIN, 2021). The input for DIFFRAC includes the dimensions, weight, and draught of the moored vessel.

3.3.2. Model output description
The aNySIM simulation generates three main output files for analysis (MARIN, 2021). Firstly, a .csv file ("res") contains time-series data of simulation output variables over three hours. The following output channels can be activated in the .xmf input file:

- Mooring line stretch
- Mooring line tension
- Fender deflection
- Fender force
- Manifold motion at specified points
- Waveprobe
- Wind force
- Current force
- Total bollard load
- x, y, z components of the bollard load

Secondly, a .txt file ("rep") provides statistical summaries of these variables, such as mean, standard deviation, and extrema. Thirdly, an mst.log file documents warnings and errors encountered during the simulation, useful for debugging.

3.3.3. Model assumptions and limitations
Although aNySIM provides a powerful framework for simulating moored vessel behavior, it relies on several assumptions (MARIN, 2022). Such simplifications may affect the fidelity of the simulations.

3.3.3.1. Wave model assumptions
The wave model assumes a flat, infinite mean water surface with constant water depth, gravitational acceleration, and density throughout the domain. It neglects bathymetric variations and interactions between waves and currents, such as wave stretching. The model is not applicable in shallow water where the depth is less than approximately 10% of the wavelength. Breaking waves and the influence of physical obstructions are also not considered. Furthermore, viscous effects and surface tension are ignored, and wave behavior is modeled through linear superposition, which is considered an acceptable compromise between accuracy and simplicity.

3.3.3.2. Wind model assumptions
The wind is modeled as a horizontally uniform velocity field, constant in both direction and magnitude across the entire spatial domain and height. Forces due to wind are incorporated using predefined, dimensionless coefficients, and the effects of wind shielding are not taken into account.

3.3.3.3. Bathymetry Assumptions
For bathymetry, the model assumes a static seabed profile that does not change over time, despite possible real-world variations due to operations such as dredging. Although the water depth, which combines tide and bathymetry, and seabed slope significantly influence the behavior and configuration of mooring lines, they are held constant in the simulations.

3.3.3.4. Current model assumptions

Currents are represented as horizontal velocity vectors that are homogeneous within each layer. Currents are taken as constant both spatially and vertically within these layers, and shielding effects are not considered.

3.3.3.5. Hydrostatics assumptions

The hydrostatics component assumes linear behavior and is valid only for small vessel motions in heave, roll, and pitch. The influence of waves on hydrostatic forces is neglected, and the shape of the waterline area is assumed to remain unchanged. Additionally, the hull is modeled to intersect the waterline vertically.

3.3.3.6. Linear and quadratic damping assumptions

The linear and quadratic damping models are both formulated in a coordinate system fixed to the ship. Forces and moments are calculated with respect to the parent body's center of mass. The models rely on the assumption of a slender hull, with large length-to-beam and length-to-draft ratios. The submerged geometry is based on the instantaneous beam and draught. The water is considered incompressible and inviscid, and effects from the free surface are neglected.

3.3.3.7. Gravity assumptions

The internal load model assumes that the body of the ship is rigid and that internal loads do not affect its structure.

3.3.3.8. Taut line assumptions

The spring module calculates the reaction force between two attachment points and assumes that the connecting spring has no mass. Both linear and quadratic spring-damper configurations are supported, and a tension-only mode can be enabled or disabled depending on the application.

3.3.3.9. Fender assumptions

Finally, the fender (ball and mesh) model determines contact loads based on spherical fenders and a polygon mesh representation of contact geometry. Contact is updated at each time step, with dynamic friction and damping effects included. Hysteresis is not considered in this model.

3.4. DMA result applications

Generally, the results of DMA simulations are used to provide an indication of the critical conditions for a specified moored vessel in specified berth. For example, Figure 3.2 displays the limiting wind conditions for a specified vessel for four different types of mooring line.

By numerically calculating the ship motions in 6 DoF and the loads in all mooring lines, a DMA can identify potential problems associated with excessive forces or motions, such as line failure. By testing various mitigation measures, such as breakwaters or multiple mooring line configurations, a DMA allows for the evaluation of their effectiveness in reducing moored vessel response (Van Koningsveld et al., 2023).

Moreover, several studies demonstrate aNySIM's application for port design, mooring system optimization, and mooring safety prediction.

Van Deyzen, Nguyen, and Eggermont (2024) simulated the response of moored container ships in gusting wind, showing how the usage of tugs and application of ShoreTension can increase safe wind speed limits. Van Deyzen, Nguyen, and Van de Sande (2024) compared static and dynamic mooring analyses for container ships in wind using aNySIM. Eggermont and Van Deyzen (2023) carried out DMAs to optimize the orientation of a jetty exposed to waves for reduced downtime using. Fleer et al. (2024) investigated the effects of mooring line type on limiting wind speeds for a future 450m container ship using aNySIM simulations. Cross and Van Deyzen (2023) presented two DMAs: one for cruise ship mooring safety under varying wind, and another to determine limiting wind and wave conditions for a tanker at a new jetty. Van Deyzen et al. (2015) showed, through two case studies, how DMAs can improve port efficiency in swell conditions, using port design optimization and applying ShoreTension systems to reduce ship motions.

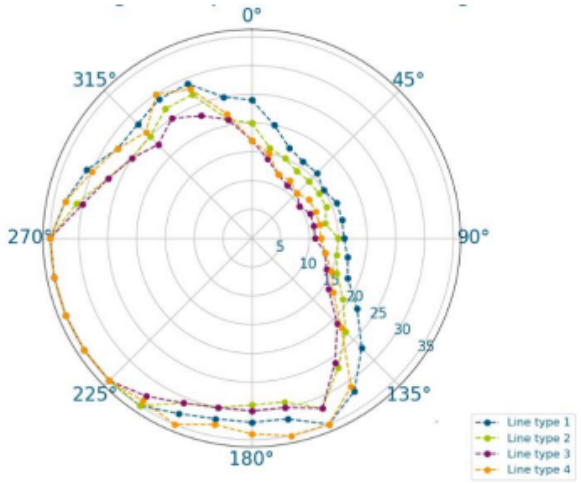

Figure 3.2: Example of DMA results for a future Ultra Large Container Ship: polar plot of the limiting wind speeds per wind directions for various line types (Fleer et al., 2024)

3.5. Conclusion

This chapter addressed SQ2: *What are the fundamental principles and key considerations of Dynamic Mooring Analysis for predicting mooring line forces of large-scale vessels in port areas?*

aNySIM is a simulation framework developed to analyze the dynamic behavior of moored vessels under varying environmental loads. It operates by solving the equations of motion for six DoF at each time step, capturing the vessel's response.

The simulation setup is primarily defined through an XMF file, which outlines the configuration of the simulation environment, including environmental conditions and system components. In addition to the XMF file, the simulation requires a Fender mesh file and a hydrodynamic database. The Fender mesh file defines the geometry of the contact plane used in the fender model. The hydrodynamic database, often referred to as the Hyd file, contains the vessel's hydrodynamic properties.

The modeling approach is based on several simplifying assumptions. Key assumptions include the use of linear wave theory on a flat, infinite water surface with constant environmental parameters, and the neglect of wave-current interactions and shallow water effects. Wind and current fields are treated as spatially homogeneous, and bathymetry is assumed static over time. Vessel hydrostatics are linearized and only valid for small motions, while both linear and quadratic damping models assume slender hulls and inviscid, incompressible water. The vessel is modeled as a rigid body, and internal loads are assumed not to influence its structural integrity. Mooring lines and fenders are simplified as massless or rigid components with idealized contact behavior.

4

DMA metamodel development

This chapter addresses SQ3: *How can a metamodel for Dynamic Mooring Analysis be developed using machine learning techniques to predict mooring line forces of large-scale vessels in port areas?*

It also covers SQ4: *What objectives and criteria are relevant for evaluating and selecting a DMA metamodel?*

A general overview of the metamodeling approach is outlined in Section 4.1. This is followed by a detailed description of the DMA-specific metamodel development using ML techniques in Section 4.2. Subsequently, Section 4.3 presents the implementation of this metamodeling process for DMA in a specified case study situated in the Port of Rotterdam.

The DMA simulations considered in this study are conducted using the aNySIM software package, which was introduced in Section 3.3.

4.1. Introduction to metamodeling

Metamodels, also known as surrogate models (Delage et al., 2022), represent the response surface of more complex simulation models, by providing simplified approximations. They map inputs to outputs when their underlying relationships are either unknown or computationally expensive to compute (Williams & Cremaschi, 2021). In essence, a metamodel is a “model of a model”, offering similar predictive capabilities but at a significantly reduced computational cost (Wang et al., 2014).

They are most commonly employed to enable fast predictions without requiring a complex and computationally expensive simulation for each scenario. Additionally, they offer valuable insight by facilitating analysis and interpretation of the behavior of the original complex model (C. Andriotis, 2024).

Two key requirements should be considered: Firstly, the metamodel must provide results significantly faster than the original simulation model. Secondly, the results must maintain a useful degree of accuracy. Achieving an optimal balance between these two factors is a challenge (Forrester et al., 2008).

The construction of metamodels typically involves three stages (Wang et al., 2014):

1. Sample design: selecting representative sample points
2. Model training: optimizing the model parameters
3. Model testing: evaluating the accuracy of the model

Any supervised learning method can be employed for metamodeling (C. Andriotis, 2024). Supervised learning is a type of ML in which a model is trained on a labeled dataset, where each sample consists of input features and corresponding target outputs. The algorithm learns a function that maps these inputs to the desired outputs (Nasteski, 2017).

Several algorithms can be used, including Linear Regression, Polynomial Regression, Gaussian Processes, Radial Basis Function Networks, Support Vector Machines, Decision Trees, Random Forests, and Neural Networks (De Bosscher, 2023; Wang et al., 2014; Williams & Cremaschi, 2019). Regardless of the chosen algorithm, the general objective is to generate predictions that approximate the true

values with minimal error. This relationship can be described by:

$$y = \hat{y} + \varepsilon \tag{4.1}$$

Where
y true output of the original model
$\hat{y}$ predicted output of the metamodel
ε prediction error

The typical workflow of training and testing ML models is illustrated in Figure 4.1

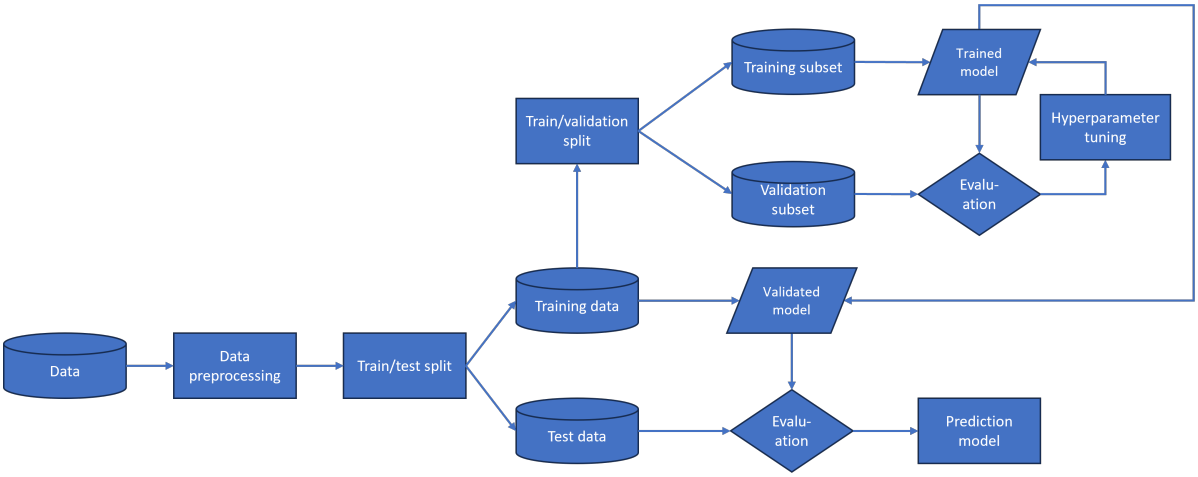

Figure 4.1: Complete workflow of a machine learning model

4.2. Methodology for developing a DMA metamodel

This section presents the general methodology for developing a metamodel that predicts mooring line forces based on DMA. The approach is grounded in supervised machine learning, where a large, simulated dataset, comprising inputs and corresponding DMA outputs, serves as the foundation for training and evaluating predictive models.

The development process includes data generation, data preprocessing, algorithm selection, training and testing of models, and model interpretability analysis (Forrester et al., 2008). Finally the candidate models are evaluated against multiple objectives in order to select the best DMA metamodel.

While the methodology is introduced in a general form here, its application to a specific case study is detailed in Section 4.3.

4.2.1. Simulated DMA dataset

The synthetic DMA dataset comprises a collection of input scenarios and their corresponding outputs, generated using the numerical DMA model. The input parameters are used as features for the metamodel, while the DMA outputs serve as target variables. The metamodel is trained to predict these target values based on the given input features.

4.2.1.1. DMA input

These input scenarios are constructed in a structured three-step process. First, the input parameters to be varied are identified. Next, the design space for these parameters is defined. Finally, a sampling technique is applied to systematically generate the final set of input scenarios.

The numerical DMA model, aNySIM, requires a separate XMF file for each simulation run. Consequently, every input scenario must be converted into an individual XMF file. A dedicated workflow was developed to automate and standardize the generation of these files, ensuring consistency and efficiency in the simulation process.

Input parameters The varied input parameters used in the DMA simulations also serve as input for the metamodel. DMA model parameters that can be varied include:

- Berth characteristics: orientation, position of the bollards, water depth
- Moored vessel geometry: dimensions, deck plan
- Operational state of the vessel: loading condition, draught, wind area
- Mooring lines: line material, MBL, number of mooring lines, layout, pretension
- Environmental conditions: wind, water level, waves, current

Many of these parameters are interconnected and cannot be varied independently. For instance, the vessel's loading condition affects its weight and draught, which in turn influence its natural frequency and dynamic response to external forces. Similarly, changes in the number of containers on deck and the draught alter the wind-exposed surface area.

Design space The design space or design domain of the parameters, within which the metamodel will operate, should be defined. These parameter ranges should be included in the input scenarios for the numerical DMA model.

Sampling methods The input scenarios for the numerical DMA model should comprehensively cover the design space. Possible sampling methods include grid sampling and Latin Hypercube Sampling. Additionally, a hybrid approach, integrating different sampling techniques, can be employed to leverage the strengths of each method.

Grid sampling involves selecting a set of values for each parameter and systematically combining them to form a structured grid design (Figure 4.2, left panel). It ensures that all combinations of the specified values are included. This method offers the most simple design, is particularly useful for exploring the entire design space systematically, and enables single-parameter sensitivity analyses. By moving along a parameter axis while keeping other parameters constant, the influence of variations in a single parameter on the model response can be evaluated. However, grid sampling has several limitations, since multiple grid points share the same parameter value. First, the model is evaluated only on a limited set of values for each parameter. Second, the total number of grid points increases exponentially with the number of parameters. Third, models exhibit varying levels of sensitivity to different parameters. Including an insensitive parameter in the grid can lead to inefficient use of computational resources, as evaluating these parameter changes may have minimal or no impact on the model output (Urban & Fricker, 2010).

As an alternative, Latin Hypercube Sampling (LHS), or near-random or quasi-random sampling (C.-Q. Li & Yang, 2023), is widely adopted (Urban & Fricker, 2010). This statistical method ensures that the design space is explored more efficiently. It is particularly useful for reducing the number of samples needed while still covering the entire range of each variable. This technique divides the range of each parameter into evenly spaced hypercubes (bins), ensuring that the number of bins equals the total number of samples. Along each parameter axis, every bin contains a sample as seen in Figure 4.2, right panel (Forrester et al., 2008). LHS maintains memory of the samples taken, thereby ensuring that each sample is unique and well distributed (Ebbs-Picken et al., 2023). Moreover, the number of samples required does not increase with the number of variables (C.-Q. Li & Yang, 2023). This efficiency allows LHS to explore a larger design space more effectively than grid sampling while using the same number of samples (C.-Q. Li & Yang, 2023). A comparison of grid and LHS designs is illustrated in Figure 4.2.

Generation of DMA input files Haskoning developed an internal workflow for generating XMF input files used in DMA simulations. Due to the extensive parameter variations required for this project, the original workflow was revised to improve flexibility and automation.

The process begins with manually prepared Mooring Arrangement (MA) sheet templates, that are Excel files that define the mooring arrangement and calculate the vessel's eigenfrequency. These templates are adjusted for parameters that are easiest to modify manually, such as mooring line layout and force-stretch characteristics.

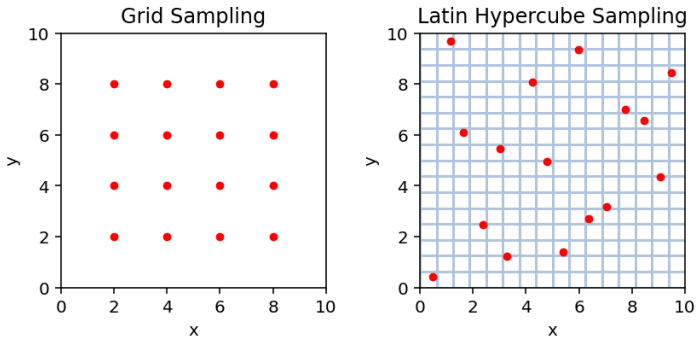

Figure 4.2: Sampling of 16 data points using grid sampling and LHS

Subsequent steps are automated using a Python script:

- MA sheets are generated for each base case, incorporating variations in parameters that impact the eigenfrequency of the moored vessel (e.g., water depth, mooring line material, MBL, pretension). The resulting eigenfrequency values from each template are extracted and temporarily stored.
- These MA sheets are then converted into XMF templates containing placeholders for additional parameters.
- Finally, the placeholders are systematically filled with scenario-specific values (e.g., wind area, wind speed, wind direction, viscous damping), resulting in a complete set of XMF files representing unique input scenarios.

4.2.1.2. DMA output

Each input scenario is executed using the generated XMF input files, with a simulation time step of 0.25 seconds, a total duration of 12,600 seconds, and a statistical analysis period beginning at 1,800 seconds.

The output of each DMA simulation consists of the minimum, mean, and maximum mooring line force for every individual mooring line. However, since the number of mooring lines may vary between scenarios, the resulting output dimensions are not uniform across the dataset. This poses a challenge for supervised machine learning algorithms, which require consistent output dimensions. To address this, a set of aggregated target variables must be defined and computed to standardize the line-specific results across all scenarios.

4.2.2. Data preparation

The development of a DMA metamodel begins with the careful preparation of the raw data generated from the simulation model. This dataset is synthetic by nature and does not contain missing values, which simplifies the initial data cleaning process.

The dataset is used to train and test the candidate metamodel and consists of features X, derived from the DMA input parameters, and targets y, calculated from the DMA output. While the raw input and output of the DMA simulations are informative, they may require preprocessing and transformation to become suitable input features and target variables for machine learning.

4.2.2.1. Encoding

DMA scenarios are generated by varying a set of model parameters that represent key mooring characteristics. These parameters form the features of the metamodel. However, some of these parameters require transformation to ensure compatibility with machine learning algorithms.

Categorical data Machine learning models typically require numerical input. Parameters that are already numeric can be directly used as features. However, categorical variables, which represent discrete, non-ordinal values, must be encoded to prevent introducing unintended hierarchies. One-hot

encoding effectively addresses this issue, creating binary indicator variables for each category and ensuring no false ordinal relationship is implied (Kosaraju et al., 2023).

Cyclic data Some input parameters are cyclical in nature, such as hour of the day, wind direction, or vessel heading. Since the cyclical structure is not inherently recognized by machine learning models, these features are transformed using sine and cosine functions to preserve their periodic properties (Mahajan et al., 2021). This allows the model to learn relationships across cyclic boundaries (e.g., 359° and 0°).

4.2.2.2. Data splitting

Once the features and targets have been prepared and formatted, the complete DMA dataset is split into training and test subsets, as illustrated in Figure 4.3 The training set is used for the purpose of training the algorithm, while the performance of the trained model is evaluated using the test subset (Shalev-Shwartz & Ben-David, 2014). Generally, the data are divided with 70% allocated for training and 30% for testing, or alternatively, 80% for training and 20% for testing (Sivakumar et al., 2024). Ensuring a balance in this ratio is important to avoid both overfitting and underfitting.

Overfitting leads to models that perform exceptionally well on training data, but poorly on new data as they memorize training examples instead of identifying the true relationships between input and output. On the other hand, underfitting results in models that perform poorly overall due to insufficient capacity or training to capture the underlying patterns in the data (Bashir et al., 2020).

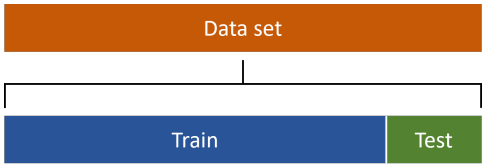

Figure 4.3: The complete synthetic DMA dataset is split in a training and test subset

To prevent data leakage, the data splitting is performed before feature selection and data scaling, both of which are described in the following paragraphs. Data leakage occurs when unauthorized information is incorporated in the training data, causing biased model training (Apicella et al., 2024). This can lead to an overestimation of the model performance during evaluation. Unauthorized information may contain knowledge about out-of-training data, without directly including these specific data, such as the test subset.

4.2.2.3. Scaling

When values of features are closer in scale, ML models can often be trained more efficiently and effectively. In contrast, widely varying feature values can lead to slower training and may reduce the model's accuracy. To address this, scaling is applied to adjust the range of feature values while preserving their distribution, ensuring that their relative relationships remain unchanged. There are two main techniques for scaling: normalization and standardization (Sharma, 2022).

Normalization adjusts the data to a fixed range, typically between 0 and 1. This process involves transforming the smallest value of a feature to 0 and the largest to 1. Each value is scaled using the formula:

$$\text{Normalized value} = \frac{\text{Value} - \text{Min}}{\text{Max} - \text{Min}} \tag{4.2}$$

Standardization, on the other hand, centers the data around a mean μ of 0 with a standard deviation σ of 1. This transformation is achieved by subtracting the mean and dividing by the standard deviation:

$$\text{Standardized value} = \frac{\text{Value} - \mu}{\sigma} \tag{4.3}$$

Unlike normalization, standardization does not depend on the range (maximum and minimum) of the data. Instead, it relies on the mean and standard deviation to ensure that the scaled data follows a standard normal distribution.

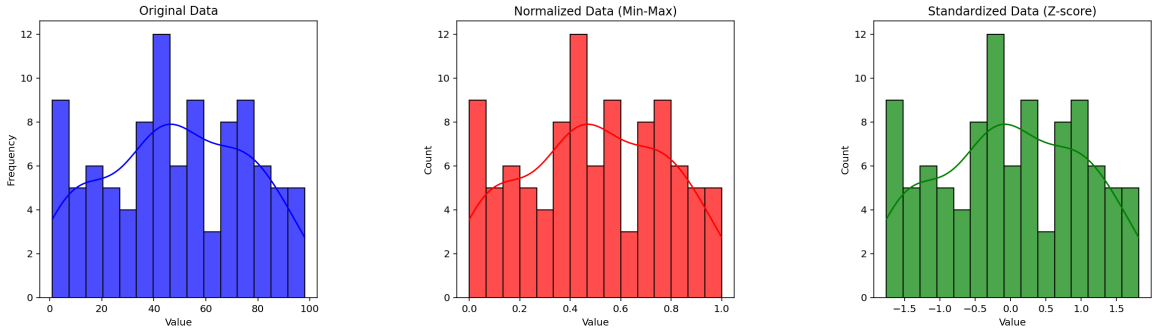

(a) Original data **(b)** Normalized data **(c)** Standardized data

Figure 4.4: Comparison of original, normalized, and standardized data of a random generated dataset

Data scaling is performed after data splitting to prevent data leakage (Apicella et al., 2024). The scaler is fitted to the training data and then used to transform both the training and testing data.

4.2.3. Machine learning algorithm selection

The prediction of mooring line forces simulated by DMA presents a Multivariate Multiple Regression problem, characterized by:

- **Multivariate input:** Multiple input features are used to describe the scenario.
- **Multivariate output:** The task involves predicting multiple output variables, representing various types of mooring line forces.
- **Continuous numerical output:** The target variables are continuous and numeric.

For this study, two different algorithms are considered for developing candidate metamodels for the DMA, both suitable for multivariate multiple regression tasks. Linear regression is selected due to its simple implementation and high interpretability, making it a strong baseline for comparison. In addition, a deep neural network model, specifically a multi-layer perceptron, is build to leverage its ability to capture complex, nonlinear relationships within the data.

The key advantages and disadvantages of these two algorithms are summarized in Table 4.1.

Table 4.1: Advantages and disadvantages of linear regression and deep neural networks

Algorithm	Advantages	Disadvantages	Reference
Linear Regression	Simple implementation; highly interpretable; low computational cost	Assumes linearity; limited in capturing complex patterns; sensitive to outliers	Sabouri et al. (2024) and Gzar et al. (2022)
Deep Neural Network	Capable of modeling complex, nonlinear relationships	Computationally intensive; requires careful hyperparameter tuning; prone to overfitting; difficult to interpret	Gzar et al. (2022), Vieira et al. (2020), and Yondo et al. (2018)

The following subsubsections provide a more detailed explanation of both algorithmic approaches.

4.2.3.1. Linear regression

Linear regression analysis is most likely the simplest and most frequently used technique for evaluating relationships between continuous variables (Hope, 2020). Multiple linear regression models the relationship between multiple input variables and a response variable by fitting a linear function (Hastie et al., 2009):

$$\hat{y} = \beta_0 + \sum_{i=1}^{n} x_i \beta_i \tag{4.4}$$

Where

$\hat{y}$ predicted output target
x_i input feature, for $i = 1, 2, \ldots, n$
β_0 intercept (bias term)
β_i coefficient corresponding to x_i , for $i = 1, 2, \ldots, n$

The model estimates the optimal values for β_0 and β_i by minimizing the sum of squared errors between the line and the actual data points. Ordinary Least Squares (OLS) is the most widely used method for this minimization problem, offering computational efficiency and, under certain assumptions, providing the best possible estimates (Hope, 2020).

In linear regression, the influence of each feature on the predicted output is reflected by the magnitude and sign of its corresponding coefficient. A larger absolute coefficient value indicates a stronger impact on the prediction, meaning the feature with the highest absolute coefficient exerts the most influence. A positive coefficient implies that an increase in the feature value leads to a higher predicted output, whereas a negative coefficient suggests the opposite effect.

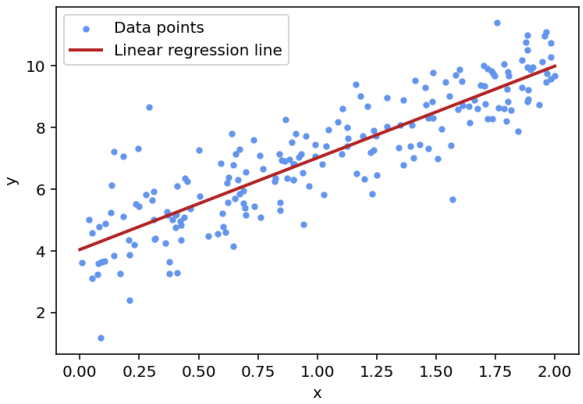

Figure 4.5: Example of a fitted linear function for a simple linear regression consisting of a single input variable x and an output variable y

Linear regression yields easily interpretable results, facilitating the understanding of the relationships between predictor and response variables. However, it does have the potentially invalid assumption that the relationships are linear. Furthermore, as the number of predictors increases, the model performance may decrease (Hope, 2020).

Even when the underlying relationships between variables are not believed to be strictly linear, linear regression algorithms often serve as a useful baseline model (Hope, 2020).

4.2.3.2. Multi-Layer Perceptron

One of the most popular and promising techniques in ML is Deep Learning (DL) (Vieira et al., 2020). The simplest DL model is the Multi-Layer Perceptron (MLP), which is a specific Deep Neural Network (DNN). MLPs, as illustrated in Figure 4.6, are inspired by the architecture of the human brain and are designed to learn complex patterns within data. This enables them to approximate nonlinear relationships between input and output variables.

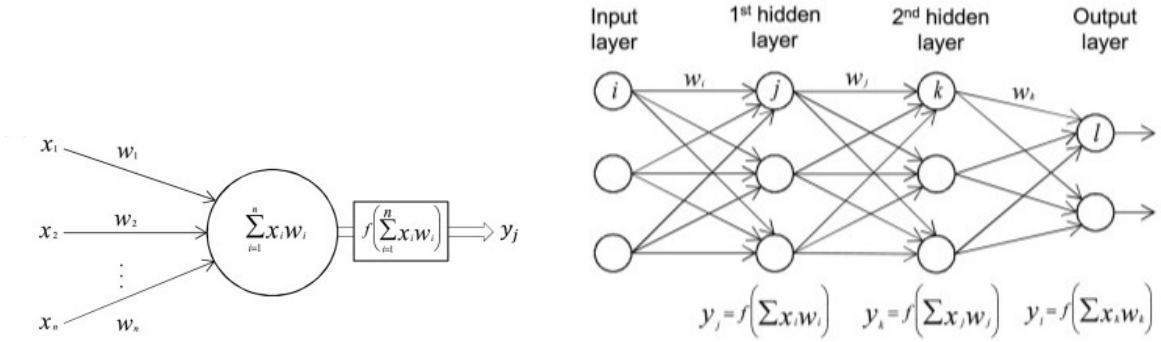

(a) Every input x_i has an associated weight w_i. The weighted sum of all inputs $\sum x_i w_i$ is transformed using a nonlinear activation function f to the neuron's output y_i.

(b) The input data is propagated through the network, transformed in every layer. The output layer generates the predicted values based on the input of the input layer.

Figure 4.6: Structure of a MLP (Vieira et al., 2020)

The architecture of a MLP is structured in three types of layers: the input layer, which receives the input data; the output layer, which produces the final prediction; and one or more hidden nonlinear layers in between, whose number determines the depth of the model. Each layer comprises interconnected neurons. These connections have associated weights that determine the strength and direction of influence between neurons. The input of a neuron computed as the weighted sum of the outputs from neurons in the preceding layer. A nonlinear activation function is then applied to this sum before the result is passed to the following layer (Vieira et al., 2020). The output of a hidden neuron is expressed as:

$$h_j = f(\sum_{i=1}^{n} w_{ji} x_i) \tag{4.5}$$

Where

h_j output of j^{th} hidden neuron
w_{ji} weight from input i to hidden neuron j
x_i input i, for $i = 1, 2, \ldots, n$
f activation function

The output of the neuron serves as input to the neuron in the next layer. This process is repeated in every subsequent hidden layer. Finally, the output layer generates the final output values, after receiving the values from the last hidden layer.

DL models are often considered "black boxes" due to their lack of interpretability in comparison to more transparent models, such as linear regression. The multiple layers of nonlinear transformations obscure the direct relationship between input and output, complicating the understanding of how predictions are made (Vieira et al., 2020).

The development of a MLP also involves selecting hyperparameters including the number of layers and neurons per layer, activation function, optimizer, learning rate, and regularization strategy. These settings are optimized through hyperparameter tuning (subsubsection 4.2.4.1). During training, the model learns by adjusting the weights to minimize the error (Vieira et al., 2020).

Number of layers and neurons Although hidden layers do not directly interact with the input or output domains, they significantly influence the model's predictive performance. Consequently, the determination of both the depth (number of layers) and width (number of neurons per layer) of these hidden layers should be carefully considered (Heaton, 2008). Unfortunately, no universally accepted method exists for determining the optimal number and size of hidden layers (Zendehboudi et al., 2017; Vieira et al., 2020).

However, Heaton (2008) recommends limiting neural network architectures to one or two hidden layers, as these configurations are capable of representing a wide range of complex functions. Besides, various rule-of-thumb methods exist for determining the appropriate number of neurons in the hidden layers of a neural network (Heaton, 2008). Common guidelines include:

- The number of hidden neurons should be within the range defined by the input and output layer dimensions.
- The number of hidden neurons should be two-thirds of the input layer size, plus the output layer size.
- The number of hidden neurons should not exceed twice the input layer size.

An insufficient number of neurons in the hidden layers can lead to underfitting, where the model fails to capture the underlying patterns in the data. Conversely, an excessive number of neurons may cause overfitting, where the model memorizes noise instead of learning generalizable features, or significantly increase training time. Therefore, an appropriate compromise between model complexity and generalization ability is necessary (Heaton, 2008).

Activation function To introduce nonlinearity, a nonlinear activation function is implemented. Common activation functions include the rectified linear unit, as well as the hyperbolic tangent and sigmoid functions (Vieira et al., 2020). These activation functions are detailed in Table 4.2 and shown in Figure 4.7.

Table 4.2: Common activation functions the MLP algorithm (Apicella et al., 2021)

Name	Function	Output range
Logistic sigmoid	$g(z) = \frac{1}{1+e^{-z}}$	$(0, 1)$
Hyperbolic tangent	$g(z) = \tanh z$	$(-1, 1)$
ReLU	$g(z) = \max(0, z)$	$(0, \infty)$

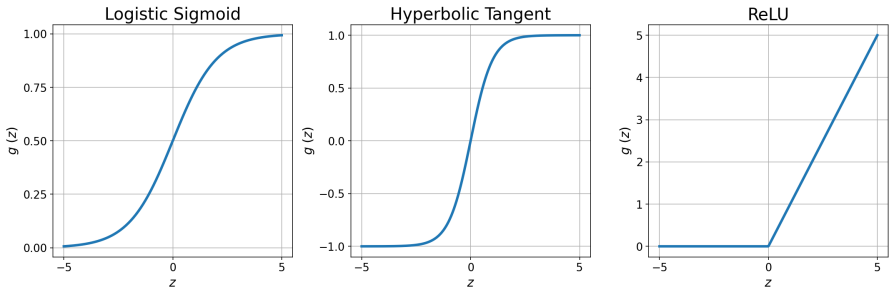

Figure 4.7: Common activation functions for the MLP algorithm

4.2.4. Training process of machine learning algorithms

The simulated DMA dataset is split into a training dataset and a test dataset. The test set is reserved exclusively for model testing purposes in the next stage and should be completely set apart.

Figure 4.8 visualizes the overall training process of machine learning algorithms. Within the training dataset, a portion is used to train the algorithm and develop a prototype model. The remaining portion is used for validation, allowing for iterative evaluation and hyperparameter tuning. Once the model and its hyperparameters achieve satisfactory performance on the validation set, the final model is retrained on the entire training set using the optimized hyperparameters. This results in the validated model used for testing in the next stage.

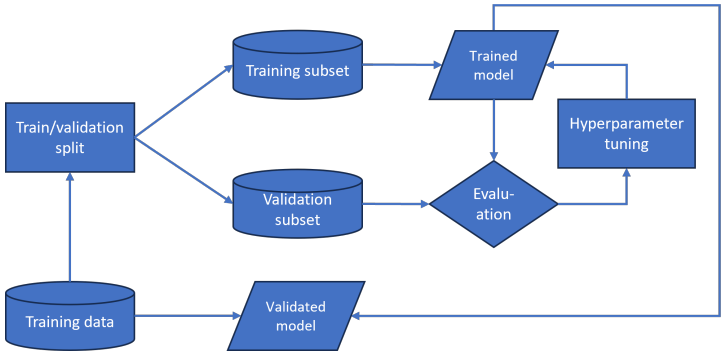

Figure 4.8: Flowchart of the training process of ML models

The linear regression model can be trained directly, whereas the MLP model requires careful hyperparameter tuning to achieve optimal performance.

4.2.4.1. Hyperparameter tuning

The initial ML algorithm represents a general model framework. However, the specific model performance of any ML algorithm are significantly dependent on its unique set of hyperparameters. These hyperparameters, which are specified prior to model training and are not learned from the data itself, require tuning in order to achieve optimal model outcomes.

Two common strategies employed for this crucial hyperparameter tuning, besides manual search, are grid search and random search.

Grid search Grid search is a widely used technique to solve the hyperparameter estimation problem, particularly in combination with cross-validation. The method systematically explores a predefined range or set of values for each hyperparameter. It constructs a grid containing all possible combinations of these values. For each combination, the model is trained and evaluated using a validation dataset or cross-validation. The hyperparameter combination that yields the highest validation performance is then selected as the optimal configuration and used for training the candidate metamodel. While effective, grid search can be computationally expensive, particularly when dealing with a large number of hyperparameter combinations (Shams et al., 2024).

Random search Random search offers an alternative approach with reduced computational cost (Shams et al., 2024). It involves randomly sampling hyperparameter values from a uniform distribution within a defined hyperparameter space. As demonstrated by (Bergstra & Bengio, 2012), a random search across the same hyperparameter space can identify models that perform equally well, or even better, but with significantly less computational effort, as compared to neural networks configured through a systematic grid search. Random search has been shown to be more efficient than grid search, especially in high-dimensional search spaces.

4.2.4.2. 5-fold cross-validation

Validation is used to estimate the performance of an ML model on unseen data and to tune its hyperparameters accordingly. An effective validation technique to avoid overfitting is 5-fold cross-validation which involves retraining the model with specified hyperparameter on different training sets.

The original training set is divided into five equal parts, or folds: over five iterations, every fold at a time is assigned as the validation subset and the model is trained on the remaining folds as illustrated in Figure 4.9. A loss function is calculated to measure the error between the prediction and the actual values in the validation subset. The errors from all five iterations are then summed to evaluate the model's overall performance. Based on the five validation results, the hyperparameters of the algorithm are tuned to optimize accuracy (Figure 4.8) (Forrester et al., 2008).

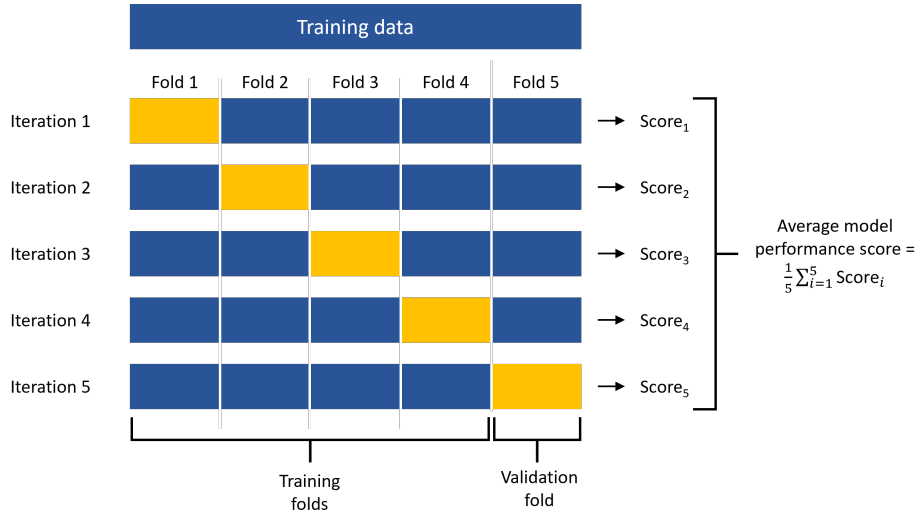

Figure 4.9: With 5-fold cross-validation the training set is divided into five folds. One fold serves as the validation set, while the remaining are used to train the model. This process is repeated over five iterations, with each fold taking a turn as the validation set. The model is retrained in each round. The overall performance score across all iterations forms the validation score, which is then used to finetune the hyperparameters.

4.2.5. Testing process of machine learning models

A randomly selected subset of the data is reserved exclusively for model testing purposes. Since these samples are solely used for evaluating the testing error after the model is constructed, they must remain untouched during the prior stages. The test error, defined by the difference between the true and predicted outputs at the test samples, is quantified using performance evaluation metrics to evaluate the performance of the model on the unseen test data (Forrester et al., 2008). The testing process is illustrated in the flowchart in Figure 4.10

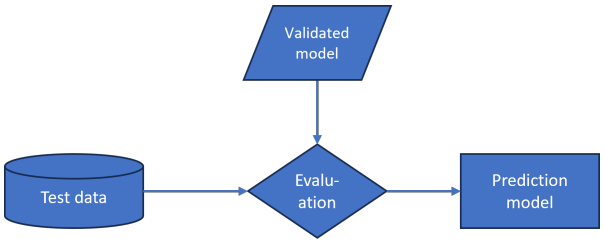

Figure 4.10: Flowchart of the testing process of ML models

4.2.5.1. Predictive performance evaluation metrics

Commonly used metrics for evaluating the predictive performance of regression models include MAE, MSE, RMSE, and R^2 (Plevris et al., 2022). Their expressions are listed in Table 4.3.

Table 4.3: Commonly used performance evaluation metrics for regression

Metrics	Formula	Value range	Ideal value
MAE	$\frac{1}{n}\sum_{i=1}^{n}\lvert y_i - \hat{y}_i\rvert$	$[0, +\infty)$	0
MSE	$\frac{1}{n}\sum_{i=1}^{n}(y_i - \hat{y}_i)^2$	$[0, +\infty)$	0
RMSE	$\sqrt{\frac{1}{n}\sum_{i=1}^{n}(y_i - \hat{y}_i)^2}$	$[0, +\infty)$	0
R^2	$1 - \frac{\sum_{i=1}^{n}(y_i - \hat{y}_i)^2}{\sum_{i=1}^{n}(y_i - \bar{y})^2}$	$(-\infty, 1]$	1

Mean Absolute Error (MAE) measures the average of the absolute differences between observed and predicted value. It indicates how closely the fitted line matches the test data points, with a positive value where closer to 0 signifies higher accuracy. The formula is given as:

$$\text{MAE} = \frac{1}{n}\sum_{i=1}^{n}|y_i - \hat{y}_i| \tag{4.6}$$

Where
n number of data points
y_i actual output value
$\hat{y}_i$ predicted output value by the model

Mean Squared Error (MSE) is the average squared difference between actual and predicted output values. Due to the squaring, larger errors have a much larger effect on the MSE than small ones, making it sensitive to outliers, unlike MAE which uses absolute differences. The formula is:

$$\text{MSE} = \frac{1}{n}\sum_{i=1}^{n}(y_i - \hat{y}_i)^2 \tag{4.7}$$

Where
n number of data points
y_i actual output value
$\hat{y}_i$ predicted output value by the model / predicted values

Root Mean Squared Error (RMSE) is derived by taking the square root of MSE, providing an error measure in the same unit as the output. It is calculated as:

$$\text{RMSE} = \sqrt{\text{MSE}} = \sqrt{\frac{1}{n}\sum_{i=1}^{n}(y_i - \hat{y}_i)^2} \tag{4.8}$$

Where
n number of data points
y_i actual output value
$\hat{y}_i$ predicted output value by the model

Coefficient of Determination (R^2) quantifies the proportion of variance in the dependent variable y_i explained by the model's independent variables x_i. R^2 is defined as:

$$R^2 = 1 - \frac{\sum_{i=1}^{n}(y_i - \hat{y}_i)^2}{\sum_{i=1}^{n}(y_i - \bar{y})^2} \tag{4.9}$$

Where
n number of data points
y_i actual output value
$\hat{y}_i$ predicted output value
$\bar{y}$ mean of the actual output values

The numerator $\sum_{i=1}^{n}(y_i - \hat{y}_i)^2$ corresponds to the sum of squared residuals (SSR), which measures the unexplained variance by the model. The denominator $\sum_{i=1}^{n}(y_i - \bar{y})^2$ represents the total sum of squares (SST), which quantifies the total variance in the dependent variable.

R^2 serves as an indicator of the model's goodness of fit, generally with values ranging from 0 to 1. A value of 1 indicates that the model perfectly predicts the dependent variable, while a value of 0 suggests that the model does not explain any of the variance in the data. However, R^2 can also take on negative values. This occurs when the model's predictions are consistently worse than simply predicting the mean of the dependent variable, indicating a poor fit.

4.2.5.2. Visualization

To understand the performance of a regression model, it is crucial to visualize its test results. Two key plots used for this purpose are the Actual vs predicted values plot and the Residual vs predicted values plots.

Actual vs predicted plot In an actual versus predicted plot (Figure 4.11), the true observed values of the target variable are plotted on the x-axis, while the corresponding values predicted by the model are plotted on the y-axis. A dashed diagonal line, representing the situation in which the predicted values perfectly match the actual values ($y = x$), serves as a reference point for ideal prediction. A perfect regression model would exhibit all data points lying precisely on this diagonal line. Consequently, the distance of the data points from this diagonal provides a visual representation of the model's prediction error. Points further away from the dashed line indicate larger differences between the actual and predicted values, implying a larger error for those particular instances.

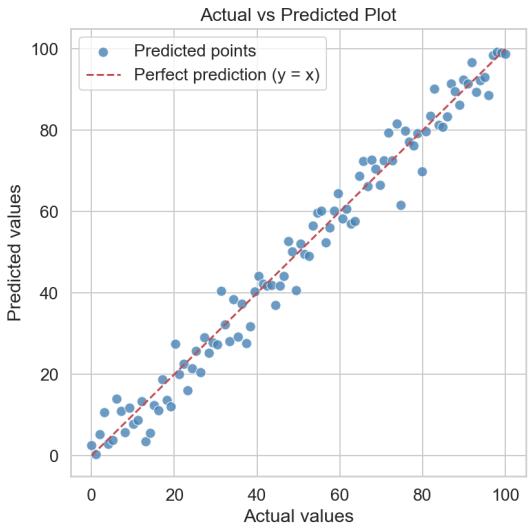

Figure 4.11: Example of an actual vs predicted plot

Residual vs predicted plot A residual versus predicted plot displays the difference between the actual observed value and the values predicted by the model (residuals) against the predicted values themselves. As highlighted by Faraway (2005), a well-fitting model will show uncorrelated residuals with constant vertical variance, symmetrically distributed around zero (Figure 4.12a).

Deviations from this ideal pattern can reveal issues with the model. If the vertical spread of the residuals is not constant, it suggests heteroskedasticity, meaning the variance of the errors changes with the predicted values (Figure 4.12b). Moreover, nonlinearity is indicated by a non-random pattern in the residuals, where the average of the residuals is not consistently zero across the predicted values (Figure 4.12c). This might suggest that some change in model could be more appropriate.

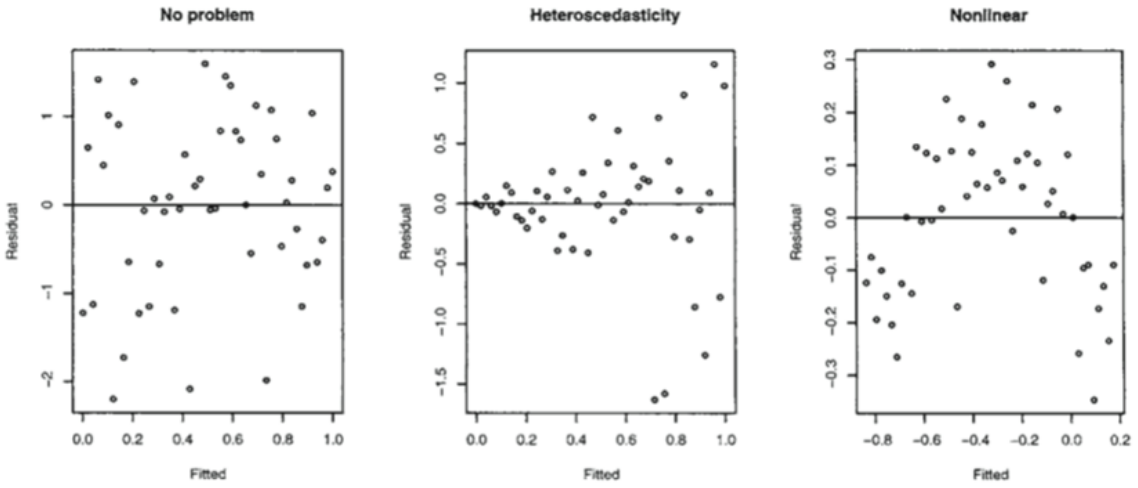

(a) Good fit

(b) Non-constant variance indicates heteroskedasticity

(c) Conditional mean of the residuals is not constant zero indicating nonlinearity

Figure 4.12: Residual vs. predicted plots (Faraway, 2005)

4.2.6. Model interpretability

For linear regression, the coefficients and intercept can be obtained, making it an interpretable algorithm. However, these coefficients do not necessarily accurately reflect feature importance due to their dependence on the scale of the features.

In contrast, a multi-layer perceptron is considered a black-box model, making them more challenging to interpret and understand. Model-agnostic interpretability methods offer a versatile approach to understanding machine learning models, as they can be applied regardless of the specific algorithm used. Two prominent techniques in this category are Permutation Importance and SHAP.

4.2.6.1. Permutation importance

Permutation importance measures the contribution of each feature to the prediction performance of the model (Molnar, 2025). This is achieved by shuffling the values of a single feature and observing the resulting decrease in model performance. The importance of the feature is quantified by the increase in this error compared to the model's original performance. Essentially, a feature is deemed important if its random shuffling leads to a higher error, indicating that the model relied on this feature for making accurate predictions. Conversely, if shuffling a feature's value has little to no effect on the error, it suggest that the model did not find that feature particularly useful and it is considered unimportant.

4.2.6.2. SHAP

SHAP (SHapley Additive exPlanations) offers an alternative perspective on feature importance, focusing on the magnitude of feature contributions to model predictions (Molnar, 2025). SHAP values, rooted in game theory principles, provide insights into how each individual feature influences a specific prediction. A negative SHAP value signifies that the feature's value contributes to a decrease in prediction value, while a positive SHAP value indicates a increase in prediction value. A SHAP summary plot serves as a visual tool to identify the most influential features and how their different values affect the model's output. In this plot, each point represents the SHAP value for a particular feature and specific instance, with the color gradient indicating the feature's value, ranging from blue for low values to red for high values. The features are ranked along the y-axis based on their overall importance.

4.2.7. Metamodel evaluation objectives

Metamodels, used as a competent replacement for simulation models, should provide fast and accurate predictions (Nejati et al., 2024). Therefore, there are two key objectives according to Forrester et al. (2008): significant speed increase in use and useful accuracy. Depending on the purpose of the

final metamodel, more objective can be added if necessary. After defining the criteria that the metamodel must meet, a multi-criteria analysis (MCA) is performed to support the selection of the optimal metamodel from the candidates.

MCA is a decision-making framework used to evaluate and rank different options based on multiple criteria (Dean, 2020). One of the most popular MCA techniques is simple additive weighting. First, the objectives are defined, which serve as the evaluation framework against which the options are assessed and compared. Criteria (at least one per objective) are then established to measure the degree to which options satisfy these objectives. Finally, each criterion is given a weight to indicate its relative significance compared to the other criteria, with criteria of high importance and preference receiving higher weights.

Simple rating, where each criterion is assigned a numerical value on a given scale based on its importance, is one of the simplest approaches for determining criteria weights. The weights are subsequently normalized to sum up to 1 by dividing each weight by the total sum of all weights. Point allocation is another weighting technique in which a fixed number of points need to be distributed among the criteria based on their perceived importance. This method becomes more challenging as the number of criteria grows. A more comprehensive weighting technique is pairwise comparison, that involves comparing each criterion to the others in pairs and labeling them with normalized weights based on these comparisons.

After determining the weights for each criterion based on its relative importance, the performance of each option against all criteria is evaluated by assigning a performance score. This score is a numerical value on a given scale, with high-performing options receiving higher scores. The weighted sum of the performance scores for each option clearly identifies the “best” choice. The results of MCA are typically presented in a performance table, as shown in the example in Table 4.4.

Table 4.4: Performance table example of MCA results using simple additive weighting, based on Dean (2020)

Criteria	**Weights (0-100%)**	**Option 1**		**Option 2**		**Option 3**	
		Score (0-10)	**Weighted score**	**Score (0-10)**	**Weighted score**	**Score (0-10)**	**Weighted score**
C1	25	5	1.25	8	2	10	2.5
C2	10	4	0.4	6	0.6	4	0.4
C3	25	3	0.75	7	1.75	8	2
C4	40	9	3.6	3	1.2	7	2.8
Total	**100%**	-	**6**	-	**5.55**	-	**7.7**
Preference rank		**2**		**3**		**1**	

4.3. DMA metamodel development for a case study

This case study applies the DMA metamodeling methodology introduced in Section 4.2 to the mooring of a 333-meter container vessel, the Cartagena Express, at the Delta Dedicated North (DDN) berth at the ECT Delta Terminal in the Port of Rotterdam (Figure 4.14). The vessel has a length overall of 333 meters, a breadth of 48 meters, and a draught of 12.25 meters, representative of large container ships currently serviced by the terminal (Sterkenbrug, 2024). The ECT Delta Terminal is a deep-sea container terminal located on the Maasvlakte with direct access to the North Sea. Its quay depth allows it to accommodate some of the world’s largest vessels (Hutchison Ports ECT Rotterdam, 2024), making it a relevant test case for mooring force analysis.

Figure 4.13: Cartagena Express (Scheepvaartwest, 2020)

Figure 4.14: Satellite photo of ECT DDN terminal, with the yellow square indicating the DDN berth (Google Earth, 2024)

The case study dataset consists of designed scenarios reflecting variations in several key parameters forming the basis for training and evaluating candidate DMA metamodels.

4.3.1. DMA dataset for case study

The case study is based on a systematically designed dataset including 11,520 scenarios. Each scenario has been numerically simulated using the DMA model aNySIM. The resulting synthetic dataset includes both the input parameters and the corresponding output mooring line forces. This DMA dataset serves as the foundation for training and evaluating the candidate DMA metamodels.

4.3.1.1. DMA input for case study

All scenarios are based on a fixed berth configuration and vessel type, as detailed in Appendix B. However, nine key parameters are systematically varied to reflect realistic operating conditions. These include:

- Water depth
- Number of mooring lines
- Mooring line material
- Minimum breaking load (MBL)
- Pretension
- Viscous damping
- Wind area
- Wind velocity
- Wind direction

For each input parameter, a set of possible values was defined based on expert consultation with the Port of Rotterdam, Royal Boatmen Association Eendracht (KRVE), and Haskoning, as detailed in Appendix B. A uniform distribution of values was not applied across all parameter axes. Given the higher accuracy of approximation models in the vicinity of given data samples (Forrester et al., 2008), the most relevant and representative values for this particular case study were selected.

By combining these parameter values, a total of 11,520 unique scenarios were generated, as summarized in Table 4.5.

The first seven parameters were varied systematically using grid sampling, generating 1,152 distinct “base cases”. Each base case was then duplicated 10 times, with a unique combination of wind velocity and direction added using LHS. This results in a total of 11,520 input scenarios.

The parameters are defined as input for the ML model and will serve as features to the ML models.

Table 4.5: Description of inputs in the DMA model

Model parameter	Value	Number of values	Number of combinations	Total number of scenarios
Water depth (m)	16.53, 18.48	2	1,152	11,520
Number of mooring lines	12, 16	2		
Mooring line material	nylon, polyester	2		
MBL (ton)	120, 130, 150	3		
Pretension (% MBL)	5, 10, 20, 40	4		
Viscous damping (%)	0, 2, 4	3		
Wind area (%)	100, 80, 60, 40	4		
Wind velocity (m/s)	5 - 18	27	1,274	
Wind direction (°)	173 - 263	90		

4.3.1.2. Output mooring force via DMA

The mooring line forces computed by the DMA are considered as output variables. The DMA output file provides, for each mooring line, the minimum, mean, and maximum force recorded over the entire simulation duration.

As the number of mooring lines varies across scenarios, the number of corresponding DMA outputs differs as well. To ensure consistency and comparability across all configurations, two aggregated target variables were defined:

- Mean mooring line force $\bar{F}_{\text{mean}}$: the average of the mean forces across all mooring lines in a simulation

$$y_1 = \bar{F}_{\text{mean}} = \frac{1}{N} \sum_{i=1}^{N} F_{i,\text{mean}} \tag{4.10}$$

  Where $F_{i,\text{mean}}$ is the mean force in line i during the simulation, and N is the total number of deployed lines.

- Maximum mooring line force F_{max}: the absolute peak force in any mooring line during the simulation

$$y_2 = F_{\text{max}} = \max_{i \in \{1,\ldots,N\}} F_{i,\text{max}} \tag{4.11}$$

  Where $F_{i,\text{max}}$ is the maximum force in line i during the simulation, and N is the total number of deployed lines.

These two aggregated values are used as target variables for the metamodels. Data analysis on output distribution and correlations with input features is available in Appendix C.

4.3.2. Data preparation

The DMA data set requires some data preparation.

4.3.2.1. Encoding

The categorical variable mooring line material is one-hot encoded, creating two features: Nylon and Polyester, as visualized in Table 4.6. Wind direction is encoded cyclically using sine and cosine transformations to reflect its circular nature as illustrated in Table 4.7.

Table 4.6: One-hot encoding

(a) Original line material data

Id	Mooring line material
1	nylon
2	polyester

(b) Converted data using one-hot encoding

Id	Nylon	Polyester
1	1	0
2	0	1

Table 4.7: Cyclic encoding

(a) Original wind direction data

Id	Wind direction [$^\circ$]
1	180
2	241

(b) Converted data using cyclic encoding

Id	Wind direction Sin	Wind direction Cos
1	sin(180)	cos(180)
2	sin(241)	cos(241)

4.3.2.2. Data splitting

The complete synthetic DMA dataset, consisting of 11,520 samples, is divided into training and test subsets using an 80/20 split. As a result, the training set comprises 9,216 samples and the test set contains 2,304 samples. To ensure reproducibility of the results, the split was performed with a fixed random state.

4.3.2.3. Data scaling

To ensure that all input features contribute equally to the model training process and to improve numerical stability, the all features and target variables were standardized as explained in subsubsection 4.2.2.3. A standard scaler was fitted to the training subset, and this fitted scaler was then used to transform both the training and test subsets.

The widely-used `StandardScaler` module from the Scikit-learn library was employed for this purpose.

Notably, the Wind direction is represented using both sine (x_{10}) and cosine (x_{11}) components to account for the circular nature of directional data, specifically over the range of 173° (southerly side wind, perpendicular to the vessel) to 263° (westerly headwind, parallel to the vessel and directed toward the bow). By standardizing these components, their interpretation is affected:

- Original sine values ranged from approximately -0.993 (at 263°) to 0.122 (at 173°). After scaling, this maps to [0, 1], with higher sine values indicating wind more perpendicular to the vessel and lower values indicating wind more parallel.
- Original cosine values ranged from -1 (at 180°, slightly past perpendicular) to about -0.122 (at 263°, headwind). After scaling to [0, 1], low scaled cosine values represent side wind, and high values represent headwind.

4.3.2.4. Feature and target sets

Table 4.8 and Table 4.9 list the final feature and target sets for the DMA metamodel.

Table 4.8: Feature variables

Feature	Parameter	Unit
x_1	Water depth	m
x_2	Number of mooring lines	-
x_3	Nylon mooring lines	-
x_4	Polyester mooring lines	-
x_5	MBL	ton
x_6	Pretension	% MBL
x_7	Viscous damping	%
x_8	Wind area	m^2
x_9	Wind velocity	m/s
x_{10}	Cosine of wind direction	-
x_{11}	Sine of wind direction	-

Table 4.9: Target variables

Target	Parameter	Unit
y_1	Mean mooring line force $\bar{F}_{\text{mean}}$	kN
y_2	Maximum mooring line force F_{max}	kN

4.3.3. Training of candidate DMA metamodels

As introduced in Section 4.2, the linear regression (LR) and multi-layer perceptron (MLP) algorithms were selected to serve as candidate DMA metamodels. Both algorithms were trained on the same dataset, comprising 9,216 samples.

LR does not require hyperparameter tuning. A linear relationship is fitted directly to the training data. The model is implemented using the `LinearRegression` module from the Scikit-learn library.

To identify the optimal hyperparameters for the MLP, a randomized grid search was performed with 1,000 iterations and 5-fold cross-validation. A fixed random seed was applied to ensure reproducibility of the results. The considered hyperparameters and their respective value ranges are presented in Table 4.10.

The network architecture was varied through the hidden_layer_sizes parameter, incorporating both shallow and moderately deep configurations. This enabled the exploration of models with different capacities to capture nonlinear relationships, while avoiding excessive complexity.

For the activation function, three commonly used nonlinear functions were considered: hyperbolic tangent (tanh), logistic sigmoid (logistic), and Rectified Linear Unit (relu). The linear activation function was excluded, as it effectively reduces the network to a linear regression model.

Both the adam and sgd solvers were tested. The lbfgs solver was excluded, as it frequently failed to converge for the dataset at hand. When the sgd solver was selected, the use of Nesterov momentum (nesterovs_momentum) was also explored to potentially enhance convergence speed and stability. Three learning rate schedules were considered: constant, adaptive, and invscaling. These schedules govern how the learning rate evolves during training and can significantly impact convergence behavior. The initial learning rate (learning_rate_init) was sampled from a range spanning one order of magnitude to explore both conservative and aggressive learning regimes. The regularization strength (alpha), corresponding to L2 weight penalty, was varied from 10^{-5} to 1.0. This range allowed evaluation of the trade-off between underfitting and overfitting. Early stopping was enabled throughout the search process to prevent overfitting and reduce training time. The maximum number of iterations was set to 1,000 to ensure convergence while maintaining practical computational limits.

After determining the optimal hyperparameters, the algorithm was retrained on the complete training dataset using this configuration. The implementation is based on the `MLPRegressor` module, in combination with `KFold` and `RandomizedSearchCV`, all from the Scikit-learn library.

Table 4.10: Defined hyperparameter space of MLP, with remaining hyperparameters set to default

Hyperparameter	Space
hidden_layer_sizes	(8,), (10,), (20,), (50,), (20, 10), (50, 20), (60,40), (100, 50), (100, 20)
activation	tanh, relu, logistic
solver	sgd, adam
alpha	0.00001, 0.0001, 0.001, 0.01, 0.1, 1.0
learning_rate	constant, adaptive, invscaling
learning_rate_init	0.001, 0.01, 0.05, 0.1
nesterovs_momentum	True, False
batch_size	64, 128, 256

4.3.4. Testing the candidate DMA metamodels

The predictive performance of both models is evaluated on the test set (2,304 samples) using standard regression metrics: MSE, RMSE, MAE, and R^2, as defined in subsubsection 4.2.5.1. These metrics are computed separately for each target variable, the mean and maximum mooring line force, as well as combined into a single global score, in which the performance across both targets is weighted equally to provide an overall assessment of the model.

4.3.5. DMA metamodel selection process

In addition to the two main primary requirements a metamodel must satisfy, further considerations were introduced in consultation with Port of Rotterdam. These include the development effort required to develop the model and its interpretability to ensure that results are transparent and understandable to stakeholders.

All considerations are grouped under three overarching objectives: *Accuracy*, *Efficiency* encompassing both speed and development effort, and *Interpretability*.

To support the selection of the final DMA metamodel from the developed candidate models, an MCA is employed. Each objective is assigned a weight to reflect its relative importance.

Accuracy receives the highest weight (55%) as the metamodel must reliably approximate mooring line forces in order to serve as a safe surrogate for numerical DMA. Within this objective, the RMSE is weighted 35% due to its sensitivity to large prediction errors, which are particularly important when estimating peak forces. RMSE values are normalized using a threshold value of 100 kN, corresponding to 10% of bollard capacity. The coefficient of determination R^2 contributes 20% as a complementary indicator of overall goodness-of-fit.

Efficiency is assigned a weight of 30% to reflect its significance in practical applications, where fast prediction enables batch processing or near real-time analysis. This objective includes two criteria: inference time (25%) and development effort (5%). Inference time, defined as the time required to produce a prediction, is prioritized due to the significant advantage it offers over the computationally intensive numerical DMA, which takes approximately 30 seconds per scenario. Scores for this criterion are normalized relative to this baseline. Development effort encompasses the time and resources needed for model design, hyperparameter tuning, and training. Model complexity, typically reflected in the number of parameters and architectural model structure, is therefore indirectly accounted for within this criterion, as it tends to influence both training effort and computational demands. Since it represents a one-time investment, it is given a lower weight. Although somewhat subjective, this criterion is scored manually.

Finally, *Interpretability* is assigned a weight of 15%. Although less critical than accuracy or speed, interpretability remains important for model validation and stakeholder confidence. It is evaluated based on transparency, reflecting the degree to which the influence of input features on predictions can be understood and explained.

The detailed weights and scoring metrics are presented in Table 4.11. All scores are scaled between 0 and 1, whit a score of 1 representing the best possible performance in that criterion.

By evaluating each candidate model against these weighted criteria, the MCA provides a structured and balanced foundation for selecting the final DMA metamodel.

Table 4.11: Objectives, criteria, and associated weights for the MCA to select the final DMA metamodel. All scores are normalized between 0 and 1, where 1 indicates best performance.

Objective	Weight (%)		Criterion	Description	Scoring
Accuracy	55	35	RMSE	Relative global RMSE	$1 - \frac{\text{RMSE}_{\text{model}}}{\text{RMSE}_{\text{threshold}}}$
		20	R^2	Global R^2	R^2_{model}
Efficiency	30	25	Inference time t_{inf}	Relative time to make a prediction for one new sample	$1 - \frac{t_{\text{inf,model}}}{t_{\text{inf,DMA}}}$
		5	Development effort	Effort taken to prepare, train, and finalize model	Manual score
Interpretability	15		Transparency	Feature importance interpretability	Manual score

4.3.6. DMA metamodel assumptions and limitations

The developed DMA metamodel is based on a set of assumptions and simplifications inherent to both the simulated scenarios used for training and the underlying numerical DMA. These factors result in a model that is limited and less detailed compared to real-world operations, affecting the accuracy and reliability of mooring line force predictions. Consequently, the metamodel may underestimate or overestimate actual mooring line forces.

4.3.6.1. General model limitations

Lack of physical constraints The DMA metamodel does not enforce physical bounds on the predicted mooring line forces. This allows for the prediction of both negative and unrealistically high mooring line forces exceeding the MBL. Consequently, line breakages and the resulting redistribution of forces among the remaining lines are not considered. Additionally, winch rendering, which typically occurs at 60% of the MBL and limits the actual force in a line (Subsection 2.2.2), is not accounted for.

Peak force representation The maximum mooring line force is reported as the highest instantaneous value observed during the simulation. No statistical processing is applied over time.

4.3.6.2. Limitations from the training dataset

The model was trained within a defined input parameter space. Therefore, its predictive reliability is limited to interpolation within this range. Predictions made for scenarios outside the training boundaries may be inaccurate or physically implausible.

Vessel and berth specificity The metamodel is trained using exclusively simulation data of the Cartagena Express moored at the DDN berth, with fixed bollard and fender positions. Therefore, its predictive accuracy is limited to this vessel-berth configuration. Application to other ships or berths requires retraining.

Mooring configuration Only two mooring configurations, one with 12 lines and an extended version with 16 lines, are included in the training dataset. The DMA metamodel is therefore limited to scenarios that exactly match these predefined patterns, as it cannot accurately predict load distributions for alternative mooring arrangements.

Pretension Mooring lines are modeled as fixed-length elements with constant pretension, assuming no winch rendering or dynamic line adjustments during tidal or operational changes. Furthermore,

all mooring lines are initialized with identical pretension values, which oversimplifies real operational variability caused by line handling, cargo operations, tidal change, or winch-specific behavior.

Viscous damping A uniform viscous damping percentage is applied equally across all three translational degrees of freedom: surge, sway, and heave. This simplification ignores directional variations in viscous damping characteristics, which can affect mooring line force predictions.

Mooring line properties All mooring lines are assumed to be identical, in perfect condition, and made of synthetic materials limited to nylon or polyester. No distinction is made for line wear, use of tails or specific material properties, even though such factors affect the behavior of mooring lines.

Passing ships The influence of passing ships has not been included. This may result in an underestimation of mooring line forces in busy waterways.

Currents The metamodel assumes no currents.

Tidal variation Water level is held constant throughout each simulation scenario due to DMA limitations. This neglects the effects of tidal cycles, which alter the vertical angles in the mooring lines and pretension over time.

Wind The DMA model applies a uniform wind field, assuming constant wind speed and direction at all heights, neglecting the vertical wind gradient typically present in the atmospheric boundary layer. This oversimplifies wind loading, especially for vessels with high superstructures and container stacks.

Wind shielding by quay structures is approximated via geometric reduction of wind-exposed areas. However, complex airflow effects, turbulence, and influences from nearby vessels, cranes, buildings, or breakwaters are not included, potentially underestimating or misrepresenting actual wind loads.

Wind coefficients were assumed fixed across simulations, despite variations in vessel loading and cargo configurations that affect aerodynamic profiles. Moreover, the coefficients are derived from wind tunnel tests on a vessel similar, but not identical, to the Cartagena Express, introducing uncertainty in predicted wind forces and, by extension, mooring line loads.

4.4. Conclusion

This chapter provided answers to SQ3: *How can a metamodel for Dynamic Mooring Analysis be developed using machine learning techniques to predict mooring line forces of large-scale vessels in port areas?* and SQ4: *What objectives and criteria are relevant for evaluating and selecting a DMA metamodel?*

A structured methodology was established for developing metamodels of Dynamic Mooring Analysis (DMA) using machine learning techniques. The approach outlines how metamodels can be constructed to approximate the output of numerical DMA simulations, in particular, the mean and maximum mooring line forces.

The general metamodeling workflow was introduced and subsequently applied to a case study involving a 333-meter container vessel moored at the ECT Delta terminal in the Port of Rotterdam. This included the design of a simulation dataset, the preparation and structuring of input and output variables, namely the mean and maximum mooring line force, and the training procedures for two candidate algorithms: Linear Regression (LR) and Multi-Layer Perceptron (MLP).

A structured model selection approach was proposed, considering accuracy, efficiency, and interpretability. This framework forms the basis for the comparative evaluation of candidate models in the next chapter, where their performance will be assessed.

5

Results and evaluation of candidate DMA metamodels

This chapter presents the performance and evaluation of the two developed candidate DMA metamodels: LR and MLP, based on linear regression and MLP regression algorithms, respectively. Section 5.1 and Section 5.2 describe the outcomes of the training and testing phases for each model, as well as analyses of feature importance and learning behavior. Both models were trained on the same training dataset, consisting of 9,216 samples, and evaluated on a shared test set of 2,304 samples. Finally, Section 5.3 compares the two candidate models across multiples objectives, including accuracy, efficiency, and interpretability, and identifies MLP as the most suitable metamodel for DMA.

5.1. Linear regression

5.1.1. Training LR

The LR model was trained on a dataset comprising 9,216 samples. The training process was completed in 0.002 seconds.

5.1.2. Testing LR

The LR model was tested on a test set containing 2,304 samples, with this batch prediction taking 0.001 seconds in total. Its performance is evaluated using various metrics in subsubsection 5.1.2.1, followed by the predicted outcomes illustrated in subsubsection 5.1.2.2.

5.1.2.1. Predictive performance metrics

The performance of the LR model is evaluated using the performance metrics MSE, RMSE, MAE, and R^2. These metrics are computed separately for each target variable and additionally combined into a uniform average to provide an overall measure of the model's predictive performance. The results are presented in Table 5.1.

Table 5.1: Performance evaluation of the LR model using metrics

Metric	Target variable		Uniform average
	$\bar{F}_{\text{mean}}$	F_{max}	
MSE (kN^2)	455	12,374	6,414
RMSE (kN)	21	111	66
MAE (kN)	16	78	47
R^2	0.9827	0.6883	0.8355

The LR model fits the mean line force $\bar{F}_{\text{mean}}$ very well but shows significantly worse performance on the maximum line force F_{max}, as indicated by the lower R^2 and higher errors.

This discrepancy is partially explainable: the mean force is an average over time and across all mooring lines, making it a relatively stable and less sensitive target. In contrast, the maximum force represents the instantaneous peak force observed on any individual mooring line, which is more susceptible to transient dynamics and local extremes. As such, F_{max} is inherently more variable and harder to predict using a linear model.

5.1.2.2. Prediction plots

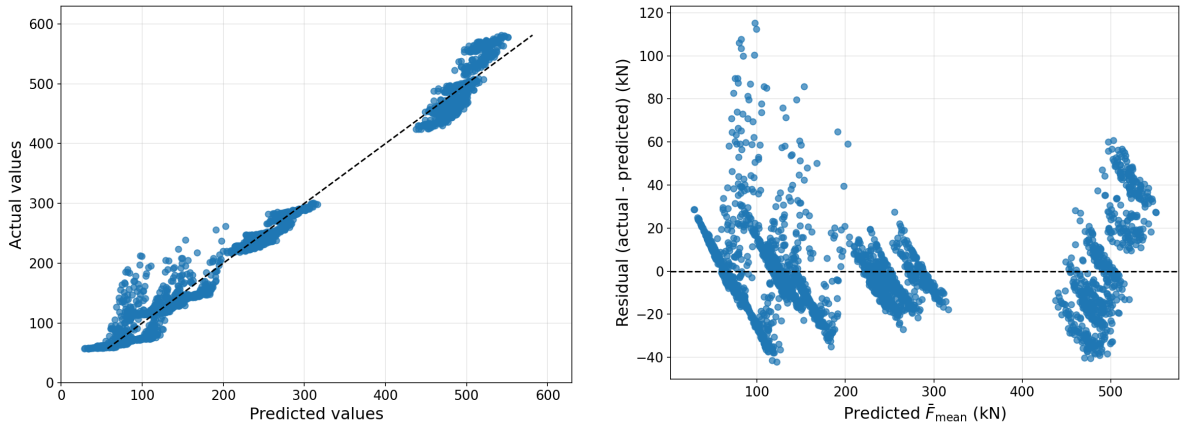

(a) Actual vs Predicted values plot

(b) Residual vs Predicted values plot

Figure 5.1: y_1: Mean line force $\bar{F}_{\text{mean}}$

According to the Actual vs Predicted values plot in Figure 5.1a, the LR model captures the overall trend quite well. However, there are slight deviations at the extremes (lower and higher ends), where predictions tend to under- or overshoot actual values. The model tends to underpredict higher actual values. The Residual vs Predicted values plot in Figure 5.1b shows a clearly nonrandom pattern in the residuals. The U-shaped curve implies underestimation (positive residuals) at the extremes (low and high predicted values) and overestimation (negative residuals) in the middle range. Additionally, the residuals are not spread around zero. This indicates nonlinearity.

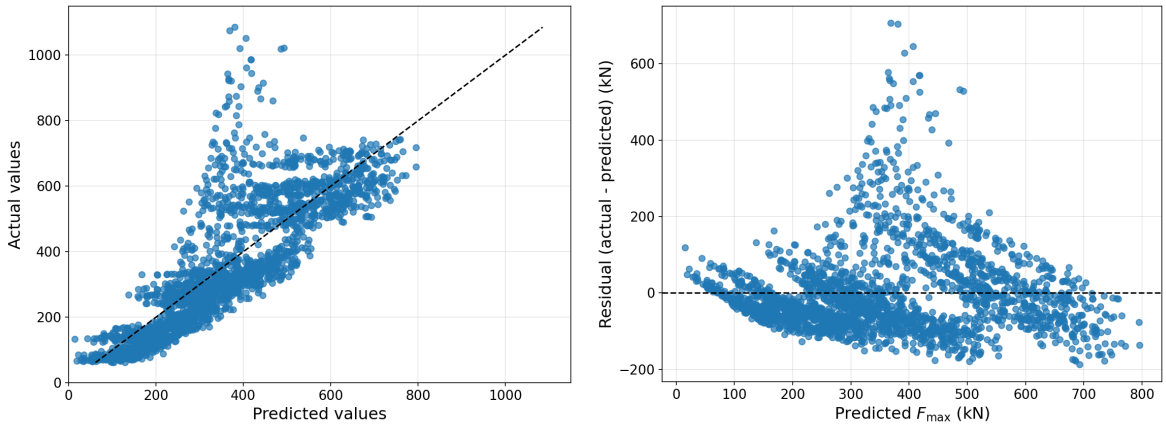

(a) Actual vs Predicted values plot

(b) Residual vs Predicted values plot

Figure 5.2: y_2: Maximum line force F_{max}

The Actual vs Predicted values plot in Figure 5.2a shows an underestimation for higher values of y_2, suggesting that the trained LR model is struggling to capture extreme values accurately. In the Residual vs Predicted values plot in Figure 5.2b a funnel shape is observed, suggesting heteroskedasticity.

5.1.3. Feature importance of LR

The feature importance of the LR model is analyzed using its coefficients, as well as model-agnostic methods: permutation importance and SHAP values.

5.1.3.1. Coefficients

The coefficients and intercepts obtained from the LR model are summarized in Table 5.2 and visualized in Figure 5.3, facilitating comparative analysis of feature influence. Since all features were standardized prior to model training, the magnitudes of the coefficients indicate the relative importance of each feature in predicting the target variables.

Table 5.2: Coefficients and intercept of the LR model

Feature	Coefficients	
	$\bar{F}_{\text{mean}}$	F_{max}
x_1 Water level	-0.001499	0.026998
x_2 Number of lines	-0.028043	-0.040348
x_3 Nylon lines	0.014359	-0.014103
x_4 Polyester lines	-0.014359	0.014103
x_5 MBL	0.120385	0.084778
x_6 Pretension	0.979948	0.665266
x_7 Wind area	0.015347	0.080227
x_8 Viscous damping	-0.002422	-0.032195
x_9 Wind velocity	0.065932	0.432430
x_{10} Wind direction sin	0.013136	0.038855
x_{11} Wind direction cos	-0.024672	-0.116377
Intercept	0.000000	0.000000

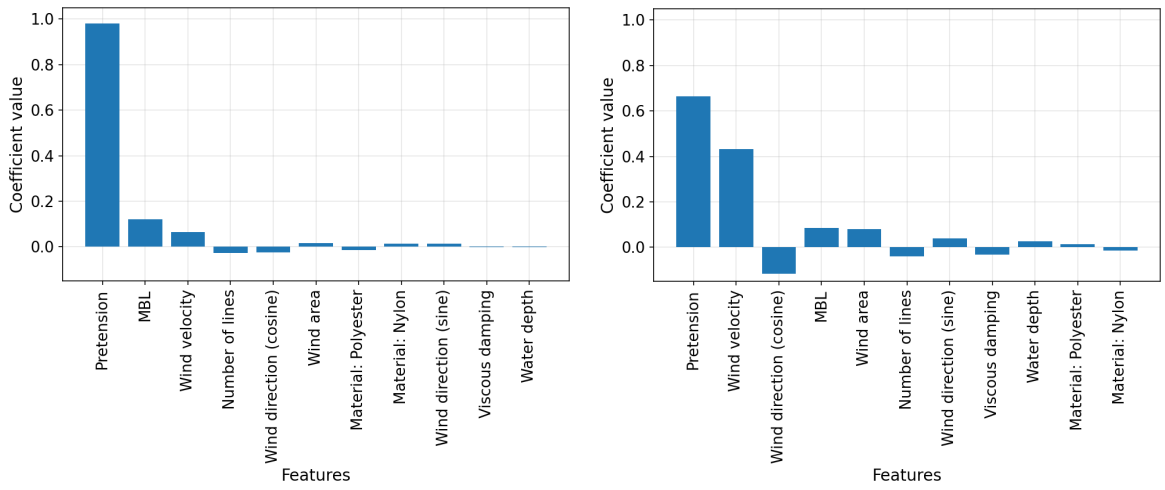

(a) Target y_1: $\bar{F}_{\text{mean}}$ **(b)** Target y_2: F_{max}

Figure 5.3: Visualization of the fitted LR model coefficients for each feature per target

The most influential feature for both the mean ($\bar{F}_{\text{mean}}$) and maximum (F_{max}) mooring line force is pretension, with coefficients of 0.98 and 0.67 respectively. This suggests that pretension has a dominant positive effect on both outputs.

Wind velocity and, MBL also show a positive and consistent influence, especially for the maximum line force, where wind velocity has a relatively high coefficient (0.43). This indicates that stronger winds and higher line strength correlate with increased mooring line forces.

The positive coefficient of x_{10} (sine) and the negative coefficient of x_{11} (cosine) for both targets suggest that mooring line forces increase as the wind direction shifts from headwind (high cosine, low sine) to side-on wind (low cosine, high sine). This trend aligns with physical expectations: wind striking the side of the vessel exposes a larger projected area than headwind, resulting in greater wind force and thus higher mooring line forces.

The number of lines has a negative coefficient for both outputs, possibly reflecting the load distribution effect: more lines sharing the total force lead to lower individual line loads.

The material type of the mooring lines, captured by Nylon (x_3) and Polyester (x_4), shows mirrored but relatively minor effects, suggesting material choice has limited direct influence when compared to pretension or environmental factors.

Lastly, viscous damping shows a small negative effect, especially on y_2, but consistent with expectations that damping reduces peak dynamic responses.

5.1.3.2. Permutation importance

Permutation importance was computed for both targets on the test set to evaluate the impact of each feature on the performance of LR and is presented in Figure 5.4.

Pretension emerges as the most influential feature by a wide margin, with a permutation importance of 1.41, far exceeding that of any other input. The next most impactful feature is wind velocity (0.19), followed distantly by MBL (0.023), cosine component of wind direction (0.014), and wind area (0.0085). These features contribute marginally to the model's predictive performance.

The remaining input variables, such as water depth, number of lines, mooring material, and viscous damping, show negligible permutation importance values (all below 0.0015). This implies that their linear association with the target variables is either weak or redundant in the presence of more dominant predictors.

Overall, the results reveal that the LR model's predictive performance is heavily concentrated in a small subset of features, particularly pretension, highlighting its critical role in mooring line force estimation.

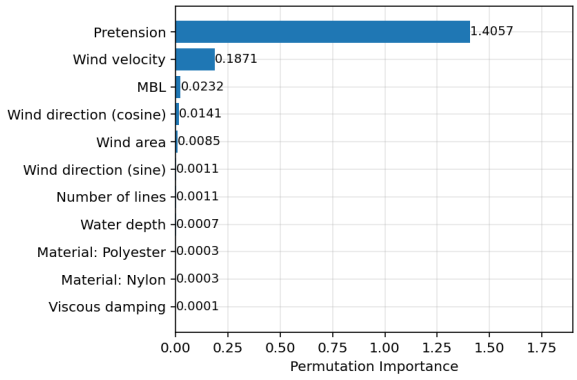

Figure 5.4: Permutation feature importance of the LR model for both target variables combined

5.1.3.3. SHAP feature importance

For both output targets, SHAP summary plots in Figure 5.5 provide insight into importance and directional influence of features within the trained LR model. The mean absolute SHAP value is indicated alongside the feature names in the plot.

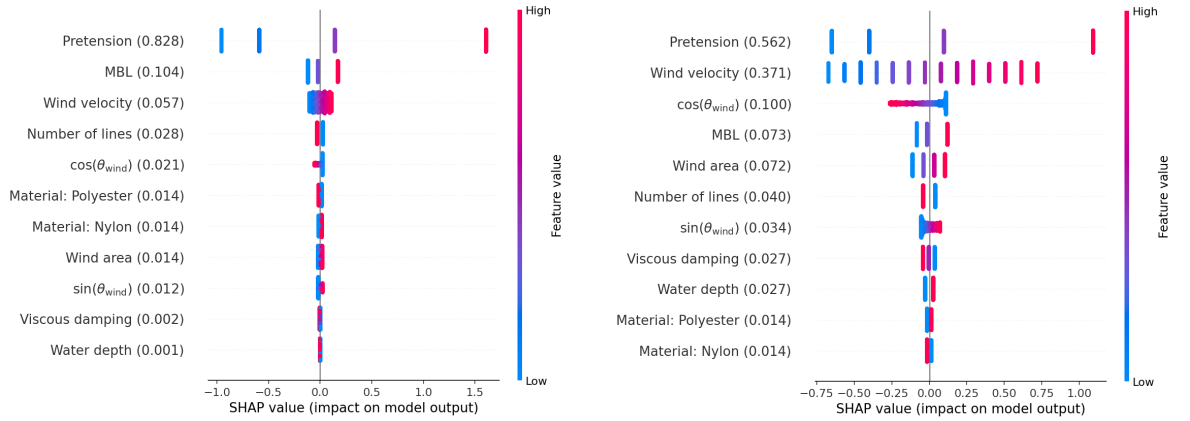

(a) Target y_1: $\bar{F}_{\text{mean}}$ **(b)** Target y_2: F_{max}

Figure 5.5: SHAP summary plots of the LR model

The SHAP plot (Figure 5.5a) indicates that pretension has by far the most dominant influence on $\bar{F}_{\text{mean}}$ with a mean absolute SHAP value of 0.828, followed by MBL (0.104) and wind velocity (0.057), which both contribute substantially less.

- Higher values of pretension (red points) lead to positive SHAP values, indicating an increase in the mean force per line.
- MBL also shows a small positive correlation with $\bar{F}_{\text{mean}}$. Higher MBL values tend to slightly increase predicted mean forces.
- Wind velocity contributes modestly; higher wind speeds lead to slightly higher predicted forces, as expected from increased wind loading.
- The number of lines and wind direction (cosine) have only marginal effects.
- Material type, sine of wind direction, wind area, viscous damping, and water depth have negligible influence.

This suggests that the pretension is the main driver for mean mooring line force in this model, with MBL and wind effects acting as secondary contributors.

For the F_{max} target (Figure 5.5b), the feature importance is more distributed:

- Pretension and wind velocity are most influential, with mean absolute SHAP values of 0.562 and 0.371, respectively. For both features, high values tend to increase the predicted maximum mooring line force.
- Wind direction (cosine) is the third most influential feature. It shows that wind parallel to the vessel (high cosine values) leads to lower predicted forces, while perpendicular wind (low cosine values) results in higher forces, due to greater wind exposure.
- MBL, wind area, and number of lines have moderate influence, while viscous damping and water depth have relatively small effects.
- Material type again plays a minor role.

Overall, while $\bar{F}_{\text{mean}}$ is primarily governed by pretension, the F_{max} is more dynamic, driven by both pretension and wind speed in LR.

5.1.4. Learning behavior of LR

Figure 5.6 presents the learning curve of the LR model for both target variables. These curves plot the R^2 scores for the training and test sets against the number of training samples, using 5-fold cross-validation for reliable performance estimation. For easier comparison, Figure G.1 presents plots with standardized y-axes.

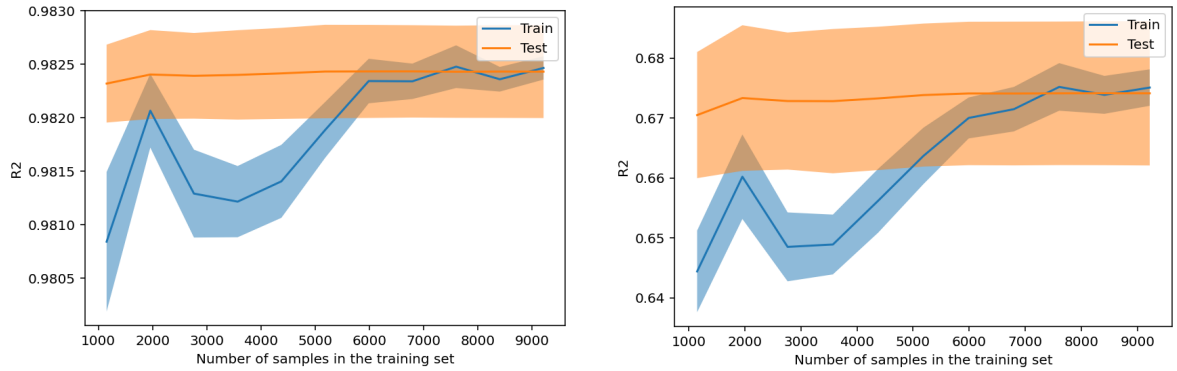

(a) Target y_1: $\bar{F}_{\text{mean}}$ **(b)** Target y_2: F_{max}

Figure 5.6: Learning curves of the LR model

As shown in Figure 5.6a, for $\bar{F}_{\text{mean}}$ the training score starts lower and gradually increases with more data, suggesting that the model benefits from additional training samples. The test score remains relatively high and stable throughout, indicating consistent generalization. The small and slightly narrowing gap between training and test scores suggests low variance and no overfitting. These trends imply that the LR model performs reliably for this target, capturing the dominant linear relationships present in the data.

For F_{max} (Figure 5.6b), both training and test R^2 scores range roughly between 0.64 and 0.68. The test score remains stable while the training score is consistently lower, with the gap narrowing as the training set size grows. The modest R^2 values indicate that the LR model struggles to accurately capture the relationship for this target, likely due to nonlinearities in the data that a linear model cannot represent effectively. This justifies exploring nonlinear models such as the MLP.

Interestingly, the test R^2 scores are slightly higher than the training scores, particularly for F_{max}. This is probably caused by underfitting on smaller training subsets and variance from the cross-validation folds, where the model may occasionally generalize better on certain test splits by chance.

Both curves show signs of convergence, indicating that increasing the training set size further will likely not improve model performance. The limited gains suggest that feature engineering or increasing model complexity would be more effective than simply adding more data.

5.2. MLP Regression

5.2.1. Training MLP

Hyperparameter tuning for the MLP model was performed using randomized search with 1000 iterations and 5-fold cross-validation on the training set of 9,216 samples. Following the tuning phase, the MLP model was trained on the full training set using the optimal hyperparameters. This overall process required 1 hour.

The hyperparameter space for the MLP model was defined to explore a broad yet computationally feasible range of model configurations. A randomized search was employed to efficiently sample this space using 1,000 iterations, combined with 5-fold cross-validation to identify the optimal hyperparameter set. The results are presented in Table 5.3. Subsequently, the model was retrained using the best-found configuration on the full training dataset to maximize generalization.

Table 5.3: The optimal hyperparameter set from this grid was identified through randomized search using 5-fold cross-validation

Hyperparameter	Space	Optimal value
hidden_layer_sizes	(8,), (10,), (20,), (50,), (20, 10), (50, 20), (60,40), (100, 50), (100, 20)	(50, 20)
activation	tanh, relu, logistic	tanh
solver	sgd, adam	sgd
alpha	0.00001, 0.0001, 0.001, 0.01, 0.1, 1.0	0.01
learning_rate	constant, adaptive, invscaling	adaptive
learning_rate_init	0.001, 0.01, 0.05, 0.1	0.1
nesterovs_momentum	True, False	True
batch_size	64, 128, 256	64

5.2.2. Testing MLP

The MLP model's predictions on the 2,304 test samples required 0.008 seconds. The model performance is evaluated using various metrics in subsubsection 5.2.2.1 and in subsubsection 5.2.2.2 the predicted results are visualized.

5.2.2.1. Predictive performance metrics MLP

The performance of the MLP model is evaluated using the performance metrics MSE, RMSE, MAE, and R^2. These metrics are computed separately for each target variable and additionally combined into a uniform average to provide an overall measure of the model's predictive performance. The results are presented in Table 5.4.

Table 5.4: Performance evaluation of the MLP model using metrics

Metric	Target variable		Uniform average
	$\bar{F}_{\text{mean}}$	F_{max}	
MSE (kN^2)	6	310	158
RMSE (kN)	2	18	10
MAE (kN)	2	9	6
R^2	0.9998	0.9922	0.9960

Compared to LR, the MLP shows a significant reduction in error metrics and higher R^2, especially on the maximum force F_{max}. This demonstrates the added value of a nonlinear model in capturing the complex relationships between input parameters and the resulting peak mooring forces.

Still, the MLP performs better at predicting $\bar{F}$mean than Fmax. This is again most likely because F_{max} represents instantaneous peak forces, which are more variable and harder to predict, whereas $\bar{F}_{\text{mean}}$ is averaged over time and therefore much more stable.

5.2.2.2. Prediction plots

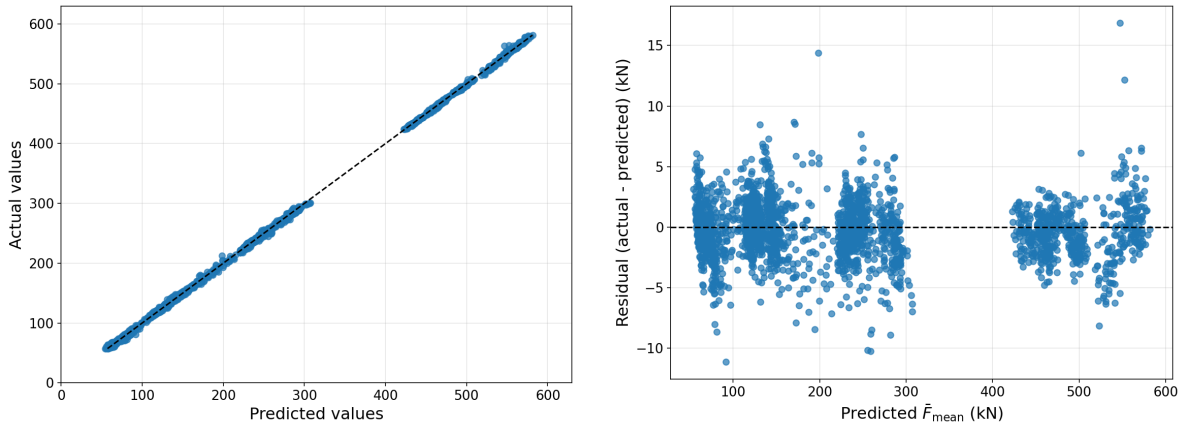

(a) Actual vs Predicted values plot

(b) Residual vs Predicted values plot

Figure 5.7: y_1: Mean mooring line force $\bar{F}_{\text{mean}}$

The Actual vs Predicted values plot for $\bar{F}_{\text{mean}}$ in Figure 5.7a shows that the points align very closely with the diagonal line, indicating a strong fit. The Residual vs Predicted values plot in Figure 5.7b suggests a homoscedastic, but slightly biased model, due to a curved pattern in the deviation of the residual mean from zero across the predicted value range.

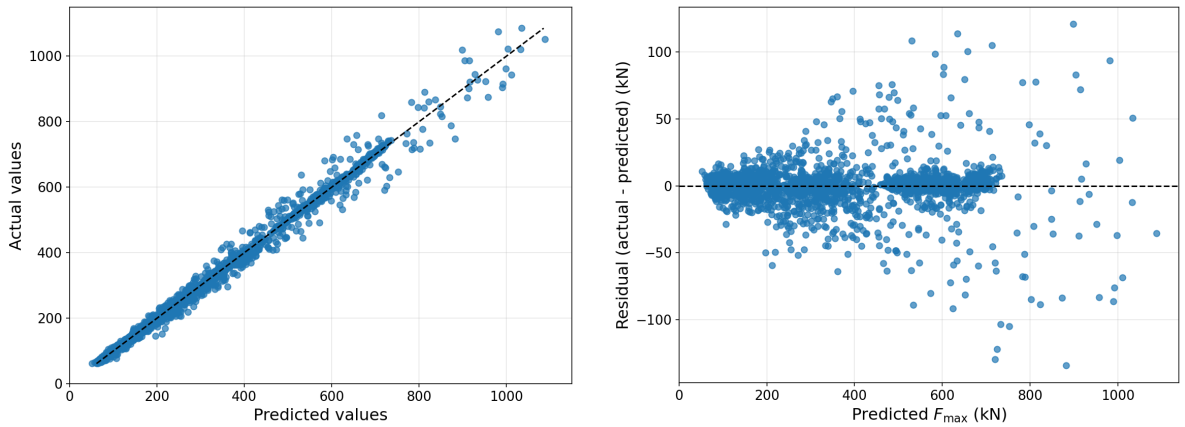

(a) Actual vs Predicted values plot

(b) Residual vs Predicted values plot

Figure 5.8: y_2: Maximum mooring line force F_{max}

The Actual vs Predicted values plot for F_{max} in Figure 5.8a presents good alignment of the predictions with the actual values. The Residual vs Predicted values plot in Figure 5.8b suggests an unbiased model as there is no average residual trend, however the cone-shaped spread of residuals reveals heteroskedasticity.

5.2.3. Feature importance of MLP

Due to the complex nonlinear nature of MLP, direct interpretation of feature importance from weights is not feasible. Permutation importance and SHAP values were used to interpret the model (Figure 5.9 and Figure 5.10).

5.2.3.1. Permutation importance

The permutation importance results for the MLP model (Figure 5.9) show a similar pattern to the LR model, with pretension being the most important feature by a large margin (1.66).

However, compared to the LR model, the MLP assigns more importance to several other features. Notably, wind velocity has a much higher importance (0.40), followed by wind direction (cosine component) (0.11) and MBL (0.046). Features like number of lines (0.034) and wind area (0.032) also contribute more to the MLP predictions than they did for the LR model.

The remaining features, including water depth, mooring material, viscous damping, and the sine component of wind direction, have relatively low importance values (all below 0.01), indicating a minor influence on the model's output.

Overall, the MLP model captures a broader range of feature effects compared to the LR, reflecting its ability to model more complex, nonlinear relationships. Nevertheless, pretension still dominates.

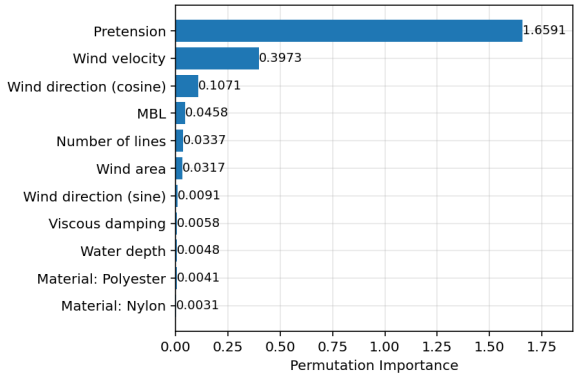

Figure 5.9: Permutation feature importance of the MLP model for both target variables combined

5.2.3.2. SHAP feature importance

For the MLP model, SHAP summary plots in Figure 5.10 reveal the nonlinear feature importance and their effect on the predicted mooring line forces. The mean absolute SHAP value per feature is also denoted in the plot.

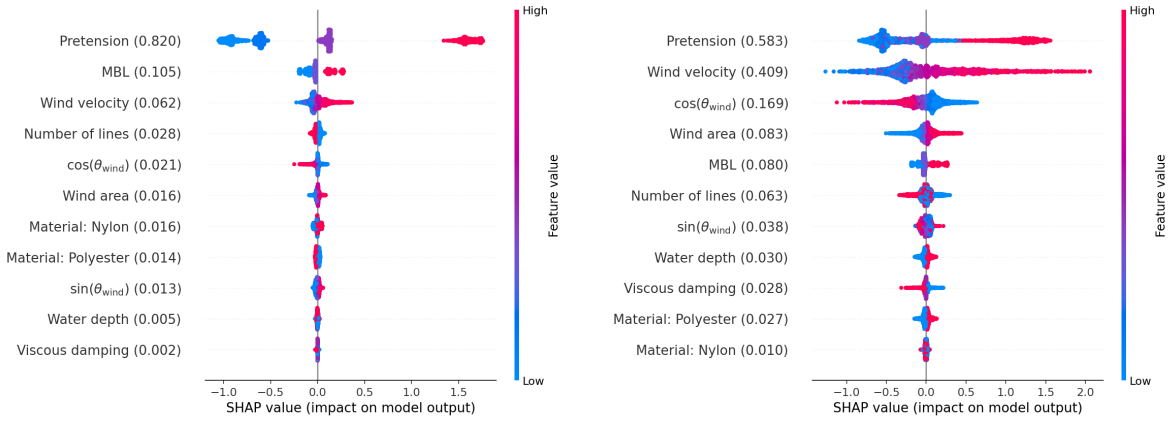

(a) Target y_1: $\bar{F}_{\text{mean}}$ **(b)** Target y_2: F_{max}

Figure 5.10: SHAP summary plots of the MLP model

The SHAP summary plot in Figure 5.10a shows that pretension is the most influential features for predicting the mean force per line $\bar{F}_{\text{mean}}$, with a mean absolute SHAP values of respectively 0.820.

- Pretension has a strong positive influence when high (red points with positive SHAP values), significantly increasing the predicted mean force. In contrast, low pretension reduces the mean line force.
- MBL also shows a clear pattern: higher MBL tends to slightly increase the predicted force.
- Wind velocity has a moderate positive impact, with higher wind velocities generally increasing the mean force.
- Number of lines and wind direction (cosine) show limited influence on the predicted mean force, but their effects align with expectations: more lines reduce the force per line due to load distribution, and side winds (low cosine values) slightly increase line forces due to greater exposed wind area.
- Wind area, material type, and wind direction (sine) have minimal influence on the predicted mean force. A larger wind area and high sine values (indicating side wind) lead to a slight increase in force, as expected due to higher wind loading.
- Water depth and viscous damping have near-zero SHAP values, indicating they are largely irrelevant for predicting the mean mooring line force.

According to Figure 5.10b, the MLP model emphasizes pretension (0.583) and wind velocity (0.409) to predict the maximum line force F_{max} with mean absolute SHAP values of 0.583 and 0.409 respectively, followed by the cosine of wind direction (0.169):

- Pretension remains the most dominant feature. High pretension values strongly increase the predicted maximum force.
- Wind velocity is the second most important factor. High wind speeds increase the output, while low speeds reduce it.
- Wind direction cosine exhibits a directional effect: lower values (parallel to the vessel) reduce the predicted force, while higher ones (perpendicular) increase it.
- Wind area shows a positive contribution to the predicted force, as expected.
- MBL, number of lines, and wind direction sine have smaller effects. Notably, the influence of the wind direction sine appears counterintuitive: higher sine values (side winds) tend to decrease the predicted force, while lower values (headwinds) tend to increase it.
- Water depth, viscous damping, and line material again play a minor role for this target.

In summary, the SHAP analysis for the MLP model confirms that pretension is the dominant feature for both mean and maximum mooring line forces. High pretension values generally lead to increased force predictions. Wind velocity and the cosine of wind direction also play a significant role in predicting the maximum force, while other features such as line material, viscous damping, and water depth contribute minimally.

5.2.4. Learning behavior of MLP

Figure 5.11 shows the learning curves of the MLP model for both targets. The curves display the R^2 score on the training and test sets as a function of the training set size. For easier comparison, Figure G.1 presents plots with standardized y-axes.

For $\bar{F}_{\text{mean}}$ (Figure 5.11a) both training and test scores increase rapidly with more training samples and converge to high values above 0.9995. The small and narrow gap between the training and test curves indicates strong generalization and minimal overfitting. The model benefits from additional data initially, but shows convergence beyond approximately 5000 samples.

In the learning curve of F_{max} in Figure 5.11b, the training score remains consistently high, while the test score starts lower and gradually improves, plateauing just below 0.993. A small but persistent gap between the training and test performance suggests slight overfitting. However, the overall test accuracy is high and stabilizes after around 6000 samples.

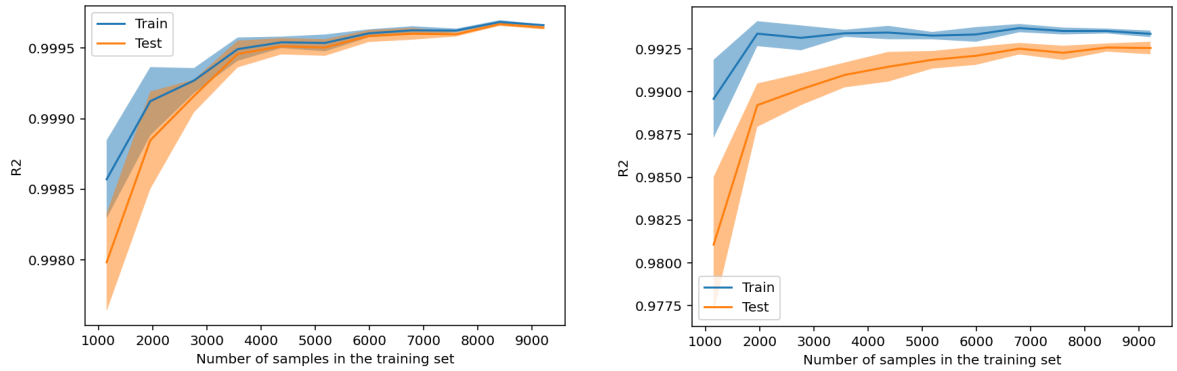

(a) Target y_1: $\bar{F}_{\text{mean}}$ **(b)** Target y_2: F_{max}

Figure 5.11: Learning curves of the MLP model

In summary, the MLP model effectively captures the underlying data relationships for both targets. For the mean mooring line force, the nearly overlapping curves and high R^2 scores indicate excellent generalization. For the maximum mooring line force, the slightly larger train-test gap points to minor overfitting, though overall performance remains strong. Further tuning could reduce this gap, but the model shows convergence beyond 6000 samples, suggesting it has already learned most relevant patterns.

5.3. Evaluation of the candidate DMA metamodels

To select the most suitable DMA metamodel among the developed candidates, a comprehensive evaluation was conducted based on three key objectives: accuracy, efficiency, and interpretability. This evaluation combines a qualitative assessment with a supporting MCA.

While the MCA provides a structured, quantitative framework for comparison, it is important to emphasize that it serves as a supporting tool rather than a strict decision-making mechanism. Due to the inherent subjectivity in assigning weights to the various objectives and criteria, the qualitative analysis plays a central role in interpreting the results and justifying the final selection.

5.3.1. Accuracy

Model accuracy is the most critical objective in the selection of the DMA metamodel. It was assessed using the global performance metrics RMSE and R^2, as described in the predictive performance evaluation. Both models demonstrated strong performance for the mean mooring line force $\bar{F}_{\text{mean}}$. However, Port of Rotterdam expressed particular interest in the maximum mooring line force F_{max}, as it represents the critical peak loads that impact bollard safety.

In this regard, the MLP model clearly outperformed the LR model, achieving a substantially lower RMSE and an almost perfect R^2 score for F_{max}. Based on the overall predictive performance, and especially its ability to accurately capture the maximum mooring line forces, the MLP is preferred model under the accuracy objective.

5.3.2. Efficiency

Efficiency is the second most important objective, particularly relevant for applications where large numbers of scenarios must be evaluated efficiently. Both models demonstrated extremely fast inference times, in the order of microseconds (0.000000-0.000013 seconds). This marks a significant improvement over to the numerical DMA simulations, which require approximately 30 seconds per run.

However, the development effort differed considerably between the models. The LR model is simple to implement and train, with no hyperparameters to tune, resulting in minimal development effort. By contrast, the MLP model required a much more involved process, including the design of a meaningful hyperparameter space and a randomized search procedure combined with 5-fold cross-validation. Additionally, training the MLP took more time due to its higher model complexity.

While both models fully satisfy the inference speed requirement, the LR model is preferred in terms of overall efficiency because of its significantly lower development effort.

5.3.3. Interpretability

Interpretability supports stakeholders trust and facilitates model validation by ensuring that predictions can be understood and justified. The LR model is inherently interpretable, owing to its simple linear structure. Its coefficients directly indicate the influence of each input feature, enabling straightforward transparency and explanation of model behavior.

In contrast, MLP has a complex architecture with multiple hidden layers and nonlinear activation functions, which obscure the internal decision logic. Understanding feature contributions requires post-hoc interpretability tools such as permutation importance and SHAP.

Therefore, under the interpretability criterion, LR is preferred due to its inherent transparency and simplicity.

5.3.4. Results of the multi-criteria analysis

The MCA was conducted to systematically compare the two candidate models based on the objectives and criteria defined in Table 4.11. The resulting scores, based on normalized values from the previous subsections, are presented in Table 5.5.

The analysis shows that the MLP model is ranked first overall, with a total weighted score of 83.00, compared to 73.70 for the LR model.

Table 5.5: Conducted MCA for the selection of the final DMA metamodel

Objective	**Criteria**	**Weights (0-100%)**	**LR**		**MLP**	
			Score (0-1)	**Weighted score**	**Score (0-1)**	**Weighted score**
Accuracy	RMSE	35	0.34	11.90	0.90	31.50
	R^2	20	0.84	16.80	1.00	20.00
Efficiency	Inference time	25	1.00	25.00	1.00	25.00
	Development effort	5	1.00	5.00	0.10	0.50
Interpretability	Transparency	15	1.00	15.00	0.50	7.50
Total		*100*	-	73.70	-	84.50
Preference rank			**2**		**1**	

It is important to note that changes in the assigned weights may affect the outcome of the acMCA, particularly in cases where candidate models perform similarly. To assess the robustness of the final ranking to changes in objective weights, a sensitivity analysis was conducted. This analysis confirmed that the MLP model consistently outperforms the LR model when accuracy is weighted at least as heavily as the combination of efficiency and interpretability, with efficiency prioritized over interpretability. The full results of this sensitivity analysis are provided in Appendix D.

5.3.5. DMA metamodel selection

Based on the combined evaluation of predictive accuracy, efficiency, and interpretability, the MLP model is selected as the final DMA metamodel. Accuracy is considered the most important criterion, and the MLP consistently outperformed the LR model in this regard. This is especially evident in predicting maximum mooring line forces F_{max}, which are a key safety concern for the Port of Rotterdam.

While the MLP entails higher development effort and offers less interpretability compared to the LR model, its substantially higher predictive performance justifies its selection. The model is therefore considered the most suitable choice for replacing numerical DMA.

5.4. Conclusion

This chapter presented the results of training, testing, and evaluating the two candidate metamodels, Linear Regression (LR) and Multi-Layer Perceptron (MLP), across multiple objectives, including accuracy, speed, and interpretability.

The LR model demonstrated reliable performance for mean mooring line force but showed limited accuracy for the maximum mooring line force, indicating its inability to capture nonlinear relationships in the data. In contrast, the MLP model achieved substantially higher predictive accuracy for both targets, with high R^2 scores and well-behaved learning curves.

Both models delivered excellent prediction speeds, enabling efficient batch predictions. However, the MLP required more development time and relies on model-agnostic methods such as permutation importance and SHAP values to interpret its behavior, while the LR model provides straightforward feature importance through its coefficients.

Considering that accuracy is the most critical objective, the MLP model is identified as the best metamodel for Dynamic Mooring Analysis in predicting mooring line forces, thereby answering SQ5: *Which proposed machine learning technique provides the best metamodel for Dynamic Mooring Analysis?*

6

Estimation of unknown input parameters

This chapter demonstrates how measurement data can be leveraged to estimate uncertain input parameters for the DMA metamodel, thereby addressing SQ6: *How can the metamodel be used to estimate unknown input parameters?*

To enhance the predictive accuracy of the DMA metamodel, a measurement-based estimation procedure is proposed for two uncertain inputs: pretension and viscous damping. These parameters cannot be directly measured, yet especially pretension has a pronounced impact on the predicted mooring line forces. Understanding the effective values of these parameters under operational conditions is crucial to improve the model's practical relevance. The approach presented here aims to estimate plausible values for these unknowns, enabling more realistic predictions in future applications.

6.1. Measurement data

A full-scale, in-situ measurement campaign was conducted on January 21–22, 2024, at the DDN berth in the Port of Rotterdam. The vessel *Cartagena Express*, identical to the one used in the DMA simulations, was moored with several mooring lines attached to Smart Bollards, allowing direct measurement of bollard loads and, consequently, mooring line forces.

In addition to line forces, relevant environmental and vessel-specific parameters were recorded, including wind speed and direction, water level, mooring line configuration, line type, MBL, and wind area. All data were aggregated into a representative sample over a selected 3-hour time window and are summarized in Table E.1. A detailed description of the data preprocessing can be found in Appendix E.

While most DMA input parameters could be derived from the measurement data, pretension (x_6) and viscous damping (x_8) remained unknown. These were estimated using the procedure outlined in the next section.

6.2. Parameter estimation methodology

To infer pretension and viscous damping, a grid-based calibration approach was applied. A total of 451 input combinations were generated by systematically varying pretension and viscous damping over predefined ranges, while keeping all other parameters fixed at their measured values.

- Pretension was varied from 0% to 40% MBL in 1% increments, resulting in 41 distinct values. This range covers typical literature values (5–10% MBL), while also accounting for potential deviations due to manually operated mooring systems.
- Viscous damping was varied from 0% to 5% in steps of 0.5% (11 values), based on practice of Haskoning.

Each of the 451 generated input sets was evaluated using the DMA metamodel to predict the mean and maximum mooring line forces ($\bar{F}_{\text{mean}}$ and F_{max}). The predicted values were compared with their measured counterparts, and absolute prediction errors were calculated.

The five input sets with the lowest absolute error were identified separately for each target. These sets are interpreted as the most plausible representations of the true, unmeasured input parameters.

6.3. Overview of parameter grid and measured values

Table 6.1 presents a complete overview of the measured inputs, unknown parameters, and measured output targets. It distinguishes between the values fixed from measurement data and the predefined ranges used for pretension and viscous damping in the sample generation.

Table 6.1: Overview of measured inputs and outputs and predefined parameter envelopes used for estimating pretension and viscous damping

Parameter	Value	DMA metamodel variable type		Data source	
		Input	Output	Measured	Predefined envelope
Water depth	17.40 m	x_1		✓	
Number of lines	16	x_2		✓	
Mooring line material	Polyester	x_3, x_4		✓	
MBL	163 ton	x_5		✓	
Pretension	[0, 40]% MBL	x_6			✓
Wind area	12%	x_7		✓	
Viscous damping	[0, 5]%	$x8$			✓
Wind velocity	16.49 m/s	x_9		✓	
Wind direction	194.64°	x_{10}, x_{11}		✓	
Mean mooring line force $\bar{F}_{\text{mean}}$	281.032 kN		y_1	✓	
Maximum mooring line force F_{max}	480.709 kN		y_2	✓	
Total number of samples	*451*				

6.4. Parameter estimation results

The predicted values from all 451 combinations ranged between:

- $\bar{F}_{\text{mean}}$: 55.942 – 572.161 kN
- F_{max}: 252.175 – 733.680 kN

The measured values (281.032 kN and 480.709 kN, respectively) fall within these bounds, confirming coverage of plausible parameter combinations.

6.4.1. Mean mooring line force

Table 6.2 lists the top five parameter combinations with the smallest absolute error in $\bar{F}_{\text{mean}}$. All five share a pretension level of 19% MBL, while viscous damping gradually increases from 0.0% to 2.0%. The optimal set, 19% MBL pretension and 0.0% viscous damping, achieved an error of only 0.358 kN (0.13%). The results indicate that the actual pretension during the selected time window was likely close to 19% MBL, with a low viscous damping value. These values are realistic.

However, the same sets of parameters underpredict the maximum force (F_{max}) by approximately 20%, highlighting that a single combination of pretension and damping may not accurately reproduce both targets simultaneously.

Table 6.2: Top five parameter combinations for pretension and viscous damping identified by minimizing the prediction error in mean mooring line force ($\bar{F}_{\text{mean}}$), along with corresponding prediction errors

Parameter	Variable type	Values				
		Top 1	**Top 2**	**Top 3**	**Top 4**	**Top 5**
Pretension (% MBL)	x_6	19	19	19	19	19
Viscous damping (%)	x_8	0.0	0.5	1.0	1.5	2.0
Measured $\bar{F}_{\text{mean}}$ (kN)	y_1^M			281.032		
Predicted $\bar{F}_{\text{mean}}$ (kN)	$\hat{y}_1$	281.390	282.160	282.810	283.342	283.759
Absolute error (kN)		0.358	1.127	1.777	2.309	2.725
Absolute percentage error (%)		0.13	0.40	0.63	0.82	0.97
Measured F_{max} (kN)	y_2^M			480.709		
Predicted F_{max} (kN)	$\hat{y}_2$	381.270	381.969	382.645	383.297	383.929
Absolute error (kN)		99.439	98.740	98.064	97.412	96.780
Absolute percentage error (%)		20.69	20.54	20.40	20.26	20.13

6.4.2. Maximum mooring line force

Table 6.3 presents the top five parameter sets to minimize the error in F_{max}. Unlike the mean force case, these combinations show substantial variation: pretension varies widely from 0% to 24% MBL, and viscous damping ranges from 0.5% and 5.0%.

The best result, 0% MBL pretension with 2.0% viscous damping, achieved an absolute error of 1.476 kN (0.31%). However, no clear pattern emerges among the top five results. The first two scenarios suggest minimal pretension, while the remaining three assume a much higher level of 24% MBL. Damping values also fluctuate inconsistently across the top combinations, with no obvious trend.

Although pretension is the most influential parameter in the metamodel, the wide spread among the top-performing results suggests that, in this case, the model struggles to resolve its true value. This lack of convergence contrasts with the results for $\bar{F}_{\text{mean}}$, where all top scenarios consistently indicated 19% MBL pretension.

Moreover, applying these top five parameter sets to the prediction of $\bar{F}_{\text{mean}}$ leads to systematic errors: low pretension combinations significantly underestimate the mean force, while the high pretension scenarios overestimate it. This further confirms that a single set of parameters may not simultaneously fit both targets accurately.

Table 6.3: Top five parameter combinations for pretension and viscous damping identified by minimizing the prediction error in maximum mooring line force (F_{max}), along with corresponding prediction errors

Parameter	Variable type	Values				
		Top 1	**Top 2**	**Top 3**	**Top 4**	**Top 5**
Pretension (% MBL)	x_6	0	1	24	24	24
Viscous damping (%)	x_8	2.0	0.5	5.0	4.5	4.0
Measured $\bar{F}_{\text{mean}}$ (kN)	y_1^M			281.032		
Predicted $\bar{F}_{\text{mean}}$ (kN)	$\hat{y}_1$	65.366	77.530	358.624	358.524	358.354
Absolute error (kN)		215.667	203.502	77.591	77.492	77.322
Absolute percentage error (%)		76.74	72.41	27.61	27.57	27.51
Measured F_{max} (kN)	y_2^M			480.709		
Predicted F_{max} (kN)	$\hat{y}_2$	479.233	476.349	475.791	475.490	475.206
Absolute error (kN)		1.476	4.360	4.918	5.219	5.504
Absolute percentage error (%)		0.31	0.91	1.02	1.09	1.14

6.5. Assumptions and limitations

The proposed estimation method involves several simplifying assumptions that may introduce error:

- A dynamic system (with time-varying parameters) was reduced to a single representative input snapshot for simulation, potentially overlooking transient behavior during the measurement window.
- The physical representation was simplified by assuming uniform pretension across all mooring lines and constant viscous damping for all motion directions. In reality, both parameters can vary considerably.
- Wind measurements were not taken directly at the berth. Instead, wind data from a nearby measurement station were used and translated to the berth location using conversion factors dependent on velocity and direction.
- Since not all mooring lines are monitored, the mooring line force targets are derived from limited measurement data. Consequently, calculated percentages from the DMA output were used to estimate these targets, introducing considerable uncertainty.
- Effects from current, changing water levels, or vessel loading conditions were not captured.

Due to these assumptions, the estimated parameters for pretension and viscous damping should therefore be viewed as effective parameters, those that best approximate real conditions under the constraints of the model.

6.6. Conclusion

This chapter demonstrated how measurement data can be used to estimate uncertain input parameters in the DMA metamodel. This directly addresses research question SQ6: *How to utilize the metamodel for estimating unknown input parameters?*

By systematically exploring a predefined parameter space and comparing predicted mooring line forces with measurements, effective values for pretension and viscous damping were identified. Key findings include:

- For $\bar{F}_{\text{mean}}$, all top results suggest pretension near 19% MBL and minimal viscous damping.
- For F_{max}, the results are less consistent, indicating higher uncertainty. The best ranked set featured no pretension and viscous damping value of 2%.

While each target could be individually approximated with high accuracy, no single parameter set minimized the error for both force metrics simultaneously. Parameter sets optimized for the mean force significantly underestimated the maximum force, and vice versa. This trade-off highlights a fundamental limitation of optimizing input parameters for a single target in isolation.

A potential improvement could involve identifying parameter sets that offer a good compromise between prediction accuracy for both targets. This multi-objective optimization approach is therefore recommended for further research.

The analysis in this study was based on a single measurement case. While it provided useful insights, additional measurements are essential to assess the robustness and generalizability of the proposed estimation approach. More data would help determine whether the observed trends are scenario-specific or reflect more universal conditions.

Despite the limitations, the proposed estimation method offers a practical and data-driven strategy for integrating measurement data into the DMA metamodeling process. This contributes to improving its reliability for operational decision-making and forecasting.

In conclusion, parameter estimation based on measurement data is a promising technique to improve DMA metamodel predictions when input parameters are uncertain. However, extending this approach to include multiple measurement campaigns is necessary for broader applicability and higher confidence.

7

Conclusions and recommendations

This thesis presents a novel, data-driven approach for predicting mooring line forces of large-scale vessels moored in port environments using machine learning techniques. The work is among the first to develop and evaluate metamodels based on 11,520 systematically generated Dynamic Mooring Analysis (DMA) simulations, offering a fast and accurate alternative to conventional numerical modeling. The resulting metamodel is not only able of replicating DMA outputs with high accuracy but also opens new opportunities for practical, probabilistic safety assessments.

This chapter answers the main research question in Section 7.1, summarizes the conclusions of the sub-questions in Section 7.2, and proposes several key recommendations to guide future work in this field in Section 7.4. Furthermore, Section 7.5 provides recommendations to the Port of Rotterdam regarding the development of an ML model for mooring line prediction, based solely on measurement data acquired within the port.

7.1. Main conclusion

The main research question of this thesis was:

How can mooring line forces of large-scale vessels moored within port areas be predicted using machine learning techniques?

To answer this, a metamodeling framework was developed, involving the generation of 11,520 DMA scenarios in a case study at the Port of Rotterdam, based on a 333-meter container vessel moored at the DDN berth. Two machine learning models, Linear Regression (LR) and Multi-Layer Perceptron (MLP) were trained on this dataset to predict mean and maximum mooring line forces. The models were assessed across three objectives: accuracy, efficiency measured in terms of prediction time and development effort, and interpretability.

The MLP model was selected as the final DMA metamodel, mainly due to its high accuracy (RMSE = 10 kN, R^2 = 0.9960) compared to the LR model (RMSE = 66 kN, R^2 = 0.8355). While the MLP required more development effort and is less interpretable than LR, it still offered sufficient transparency through feature importance analyses. Both models dramatically increased prediction speed compared to the numerical DMA, which requires approximately 30 seconds per simulation, achieving inference times on the order of microseconds.

Feature importance analysis revealed that pretension was the dominant factor for predicting mean mooring line force, while pretension and wind velocity were most influential for the maximum force.

7.2. Sub conclusions

To support the main research question, the preceding chapters addressed the sub-questions as defined in Section 1.3. This section summarizes the key findings from each.

7.2.1. Key aspects of mooring

SQ1: *What are the key aspects characterizing the mooring of large-scale vessels in port areas?*

Three key aspects have been identified: environmental conditions, the mooring system, and ship characteristics. Environmental conditions such as wind, current, waves, tide, and passing vessels apply external forces on the vessel. The mooring system, which includes mooring lines, winches, fenders, berth structures, mooring points, and alternative mooring techniques, is responsible for restraining vessel motions. Ship characteristics, including dimensions, load state, and force coefficients for wind and current, determine the impact of external forces and define the capacity of the mooring equipment.

These key aspects collectively impact the response of the moored vessel, including the mooring forces on lines and fenders, as well as the vessel's motions.

7.2.2. Dynamic Mooring Analysis

SQ2: *What are the fundamental principles and key considerations of Dynamic Mooring Analysis for predicting mooring line forces of large-scale vessels in port areas?*

Dynamic Mooring Analysis (DMA) is a numerical model that simulated the dynamic response of moored vessels under time-varying loads. The aNySIM framework implements this by solving the equation of motion in six degrees of freedom in the time domain, considering nonlinearities. It requires detail input on environmental conditions, vessel properties, and mooring system configurations. Key assumptions include linear wave theory, homogeneous environmental fields, and idealized mooring components, which introduce limitations.

7.2.3. Developing a DMA metamodel

SQ3: *How can a metamodel for Dynamic Mooring Analysis be developed using machine learning techniques to predict mooring line forces of large-scale vessels in port areas?*

A DMA metamodel can be built by training supervised machine learning algorithms on a systematically generated dataset of DMA simulations. The process involves defining relevant input parameters, generating synthetic data using the aNySIM software, and preparing the dataset through encoding, aggregation of target variables, and scaling. In this study, Linear Regression and Multi-Layer Perceptron (MLP) were trained as candidate metamodels. The MLP model requires hyperparameter tuning, which was performed using 5-fold cross-validation.

7.2.4. Evaluation criteria for metamodel selection

SQ4: *What objectives and criteria are relevant for evaluating and selecting a DMA metamodel?*

Metamodels should primarily meet the requirements of accuracy and speed. The selection of the best DMA metamodel in this work was based on three objectives: predictive accuracy, efficiency, and interpretability. Accuracy was assessed using metrics RMSE and R^2. Efficiency referred to both the prediction time and the development effort required to train and tune the model. Interpretability concerned the extent to which model behavior can be understood, either inherently or through model-agnostic tools. While the relative importance of these criteria may vary depending on the application, this study prioritized accuracy, followed by efficiency and then interpretability. A multi-criteria decision framework was used to systematically evaluate and compare the candidate models based on these objectives.

7.2.5. Best-performing model

SQ5: *Which proposed machine learning technique provides the best metamodel for Dynamic Mooring Analysis?*

The MLP model was identified as the best-performing DMA metamodel mainly due to its high predictive accuracy. Inference time was on the order of microseconds, comparable to LR and significantly faster than original DMA simulations, which require approximately 30 seconds per scenario. However, more development effort was required because of hyperparameter tuning. While the MLP model offered less transparency than the LR model, its interpretability was considered sufficient through the use of model-agnostic tools.

7.2.6. Estimating unknown input parameter

SQ6: *How to utilize the metamodel for estimating unknown input parameters?*

The proposed method systematically explored a parameter grid for the unknown inputs and compared predicted mooring line forces with field measurements in order to identify plausible parameter values. For a measurement case with unknown pretension and viscous damping, the approach successfully found values using the mean mooring line force. However, estimations based on the maximum force were less consistent, and did not correspond to the values found using the mean force. This highlighted the need for multi-objective optimization. Although the analysis was based on a single measurement campaign, the method offers a practical, data-driven approach to refine metamodel predictions. Applying this method to multiple measurement cases is necessary to assess its effectiveness and generalizability.

7.3. Contribution

This research contributes to filling a gap in the literature by introducing a metamodel specifically designed to predict mooring line forces for large-scale vessels in port environments. The metamodel provides valuable insight into the behavior of the numerical DMA and offers a faster, more accessible alternative to full numerical simulations, while maintaining a high level of predictive accuracy.

This increased computational efficiency allows for rapid scenario assessments and enhances usability in operational settings where some input parameters may be uncertain or unavailable. In such cases, the metamodel can be applied inversely, using known mooring line forces and input parameters to estimate and update the remaining unknown values. This improves the reliability and practicality of future predictions.

Furthermore, a key contribution of this work is the integration of the DMA metamodel into a probabilistic framework. By sampling from distributions of relevant input parameters, the metamodel can generate a distribution of mooring line force predictions. This enables the estimation of exceedance probabilities for critical infrastructure thresholds, such as bollard capacity, supporting more reliable risk assessment and data-informed decision-making for port design and maintenance. An illustrative application is provided in Appendix F.

7.4. Recommendations for future research

Due to the defined scope of this study and limitations of the developed DMA metamodel described in Subsection 4.3.6, several recommendations for future work are outlined in this section.

7.4.1. Extend DMA metamodel

The current DMA metamodel is trained on a dataset derived from a limited set of simulated scenarios. As such, its predictive capabilities are constrained by the specific scenario design space, including vessel type, mooring layout, berth configuration, and environmental conditions, used during dataset generation.

To improve the generalizability and applicability of the metamodel across a wider range of operational conditions, it is recommended to extend the input parameter space. This involves including additional parameters as well as broader value ranges.

Implementing such an extension requires adapting the workflow for generating XMF input files. Once the expanded set of DMA simulations is completed, the same data processing and modeling steps outlined in Chapter 4 can be applied to retrain the model.

To extend the applicability of the DMA metamodel beyond the current case study, the following directions are proposed:

- Alternative mooring layouts: Simulate alternative mooring configurations (e.g., different line patterns) and include layout parameters as input features in the model.
- Multiple berths: Integrate berth-specific characteristics such as quay geometry, bollard and fender locations into the simulation scenarios and include corresponding input parameters in the dataset.
- Different vessel classes: Incorporate vessel of various sizes in the scenarios and include vessel-specific features such as length, beam, displacement.

7.4.2. Alternative calculation of maximum mooring line force

The maximum mooring line force reported in the simulations represents an incidental peak value observed during the simulation period. While this approach identifies instantaneous extremes, it does not account for the statistical distribution of tensions over time. An alternative is to estimate the maximum force using statistical measures, by combining the mean force with a multiple of the standard deviation ($\mu + k\sigma$). This reduces sensitivity to single outliers and could provide a more robust estimate of the probable maximum loads.

7.4.3. Explore more algorithms

This research investigated the performance of two specific machine learning algorithms as candidates for a DMA metamodel. While these algorithms yielded promising results, other models may offer improved performance. Future research is encouraged to explore a broader spectrum of machine learning algorithms to determine whether higher accuracy or computational efficiency can be achieved.

In addition, the hyperparameter search space for the MLP model was deliberately limited due to computational constraints. Expanding this parameter grid in future studies may lead to the identification of more optimal configurations, potentially resulting in increased performance.

7.4.4. Reduce subjectivity in metamodel selection

The evaluation of metamodels using MCA is known to be highly sensitive to the assignment of weights, which introduces subjectivity into the decision-making process. Consequently, MCA is employed as a complementary tool rather than serving as the sole basis for selecting the optimal metamodel.

For future research, it is recommended to explore more rational, preference-based decision-making frameworks. One such approach is the use of decision-support tools such as Tetra (Scientific metrics, 2022), which aims to reduce subjectivity by implementing a mathematical framework for systematically combining and interpreting preferences.

7.5. Recommendations for measurement-based model

A DMA metamodel was developed that offers a reliable and significantly faster alternative to the numerical DMA, while maintaining high predictive accuracy. However, DMA is based on simplified representations of reality, involving assumptions. These simplifications introduce uncertainties that limit the reliability of both the numerical DMA and its metamodel in dynamic operational settings.

To overcome these limitations, it is recommended that the Port of Rotterdam develops a machine learning model trained entirely on field measurements. Such a measurement-based model would capture operational variability and human behavior more realistically, and can reduce the reliance on assumptions inherent to DMA. Prior research (subsubsection 1.1.3.2) has already demonstrated the potential of data-driven models for moored vessel response prediction.

Therefore, this section addresses SQ7: *What specific field data should be collected by Port of Rotterdam to enhance applicability of machine learning models for mooring line force prediction, and what recommendations can be made for developing such models?*

7.5.1. Measurement parameters

To build a reliable and accurate machine learning model for predicting mooring line forces, the variables listed in Table 7.1 should be collected. The model should treat mooring line forces (from smart bollards or load cells) as target variables, and the remaining parameters as features.

Many of the recommended parameters are already measured or recorded in the Port of Rotterdam. For those not yet automatically available, manual collection can offer an interim solution. The dataset should aim to reflect realistic operational conditions, including environmental factors, ship-specific characteristics, mooring configuration, and human-influenced decisions.

Table 7.1: Recommended measurements and sensors for an operational mooring force prediction model based on field data

Category	Parameter		Sensor type, Source
Mooring forces		Mooring line loads	Load cells
		Bollard loads	Smart Bollards
Environmental conditions	Wind	Wind speed, direction	Ultrasonic or cup anemometers with wind vanes
	Waves	Wave height, period, direction	Wave radar, ADCP, buoys
	Tide	Water level, flow direction	Tide gauges, pressure sensors, ADCP
	Current	Current speed, direction	ADCP, electromagnetic or acoustic current meters
	Passing vessel characteristics	Length, beam, draught, UKC, speed, distance	AIS, Port radar, LIDAR, Cameras
Vessel	Ship characteristics	Length, beam, draught, DWT, vessel type	AIS data
		loading condition, windage area	Ship manifest, camera-based estimation
	Mooring line	Material, MBL, diameter	Manual input via captain
	Human behavior	Shipping company, vessel name	AIS data
Mooring		Mooring line configuration	KRVE
		Ship heading	KRVE, AIS data
Berth	Fender	Position, layout	Port database, manual input
	Bollard	Position, capacity	Port design drawings
	Quay	Orientation	Satellite photo

7.5.2. Considerations for data collection

7.5.2.1. Pretension

Pretension is one of the most influential predictors of mooring line forces. It fluctuates throughout the berth visit due to tidal changes, vessel loading, and crew behavior. While current smart bollard data shows that lines are not always adjusted appropriately, indirect indicators, such as tide level and shipping company practices, can help infer pretension dynamics.

7.5.2.2. Mooring line properties

Line material and MBL affect mooring line forces. These mooring line properties are often unknown. Notably, mooring line types may vary even within a single vessel.

Communication with agents or captains should be encouraged to standardize and log this data. The shoremen of KRVE already records subjective assessments of the weight of the lines, categorizing them as lightweight, moderate, or heavy. This data can be used as a temporary substitute until more precise data becomes routinely available.

7.5.2.3. Mooring line pattern

KRVE currently documents the number of mooring lines and their type (spring and breast). While this helps, the exact mooring layout is often only captured through quickly taken photos. Future automation through camera-based detection of mooring patterns would enhance accuracy, but for now, structured manual input is sufficient.

7.5.2.4. Mitigating measures

Devices such as ShoreTension units are often used for the mooring of large-scale vessels as a precautionary measure, because they reduce the line forces. Their presence and approximate position should therefore be documented. The units are visible in mooring layout photos, and the number deployed is logged by KRVE.

In addition, tugboats may be temporarily deployed during periods of strong off-quay winds to help maintain the vessel's position by applying lateral force toward the quay. Recording the occurrence and duration of such tug assistance is recommended, as these actions also lower the forces in the mooring lines.

7.5.2.5. Vessel identification

Using AIS data and port booking information provided by the Rotterdam Port Authority, vessels moored at the DDN berth can be accurately identified. This allows the Smart Bollard load measurements to be

linked to the correct vessel, along with its relevant characteristics.

7.5.2.6. Passing vessels

Passing vessels induce loads on moored vessels. These can be detected using AIS data, which includes vessel speed, length, beam, and draught. AIS also provides vessel position, allowing for the calculation of the relative distance between the passing and moored vessels. These parameters should be included as time-varying input features to the model.

7.5.2.7. Mooring time

Mooring operations typically take up to an hour, during which bollard load measurements do not reflect the fully secured condition of the vessel. For this reason, data collected during this period should be excluded. Measurement should begin only after mooring is fully completed and stop before unmooring operations start.

7.5.2.8. Environmental delay

Wind gusts and wave forces have delayed effects on ship response. Therefore, it is advisable not to rely on measurements from a single moment in time, but rather to use a short time window to capture the full impact of environmental conditions on mooring forces.

In addition, when environmental sensors are not located directly at the berth, a time shift, either a lag or a lead, could be applied to better align environmental data with mooring force response.

7.5.2.9. Preprocessing

All time series data must be synchronized and combined into a single dataset of timestamped feature-target pairs. Careful preprocessing is critical for model performance and interpretability.

7.5.2.10. Mooring line force

A key challenge in using smart bollards to measure mooring line forces is that multiple lines may be attached to a single bollard. This leads to aggregate force measurements that do not represent individual line forces. Additionally, not all lines are necessarily connected to smart bollards, meaning not all line forces are measured. This depends on the mooring arrangement and available bollard positions along the quay.

As an alternative, load shackles can be temporarily installed on individual mooring lines to capture line-specific forces directly. While more accurate, this method is more intrusive and costly, making it less feasible for large-scale deployment. If individual line forces are unavailable, the model could instead be trained to predict bollard loads, which are directly measured and operationally relevant to the Rotterdam Port Authority.

7.5.3. Machine learning algorithm

Based on the results of the DMA metamodel selection in Section 5.3, a multi-layer perceptron (MLP) is recommended for the field-trained model. It achieved high predictive accuracy and fast inference times, both important for decision-making in port operations.

Learning curve analysis showed that the MLP model reached near-optimal performance with approximately 1,000 training samples. This indicates that the model is data-efficient and capable of learning meaningful patterns even from relatively small datasets. This property is particularly valuable for the proposed application, where the measured field data may initially be limited in size and quality.

7.5.4. Required number of measurements

Based on the findings, the MLP algorithm is expected to be more effective than LR when learning from limited measured data. In the context of the DMA metamodel, approximately 5,000 samples were sufficient to reach near-optimal (99.9%) performance for this algorithm. While this offers a preliminary indication of the data requirements for the operational model, it is important to recognize that the actual number of required samples will likely be significantly higher. This is due to differences in the number and type of input features, the presence of noise, and complexity of real-world measurement data compared to the simulated data used in this study.

References

1. Abdelwahab, H., Pinheiro, L., Santos, J., Fortes, C., & Soares, C. G. (2024). Experimental investigation of wave severity and mooring pretension on the operability of a moored tanker in a port terminal. *Ocean Engineering*, *291*, 116243. https://doi.org/10.1016/j.oceaneng.2023.116243
2. Alvarellos, A., Figuero, A., Carro, H., Costas, R., Sande, J., Guerra, A., Peña, E., & Rabuñal, J. (2021). Machine learning based moored ship movement prediction. *Journal of Marine Science and Engineering*, *9*(8), 800. https://doi.org/10.3390/jmse9080800
3. Andrés, S., & Piniella, F. (2017). An analysis of aids to navigation systems on inland waterways as an element of competitiveness in ulcv. *International Journal for Traffic and Transport Engineering (IJTTE)*, *7*, 1–18. https://doi.org/10.7708/ijtte.2017.7(1).01
4. Apicella, A., Donnarumma, F., Isgrò, F., & Prevete, R. (2021). A survey on modern trainable activation functions. *Neural Networks*, *138*, 14–32. https://doi.org/10.1016/j.neunet.2021.01.026
5. Apicella, A., Isgrò, F., & Prevete, R. (2024). Don't push the button! exploring data leakage risks in machine learning and transfer learning. *arXiv preprint arXiv:2401.13796*. https://arxiv.org/abs/2401.13796
6. Barden, L. (2018). *Glossary of nautical terms and abbreviations*. Retrieved May 23, 2024, from https://www.nomadsailing.co.uk/learning-zone/glossary.html
7. Barros, P. W., & Mazzilli, C. E. (2018). The nonlinear dynamic behaviour in an alongside berth mooring arrangement. *Journal of the Brazilian Society of Mechanical Sciences and Engineering*, *40*, 1–13.
8. Bashir, D., Montañez, G. D., Sehra, S., Segura, P. S., & Lauw, J. (2020). An information-theoretic perspective on overfitting and underfitting. In M. Gallagher, N. Moustafa, & E. Lakshika (Eds.), *Ai 2020: Advances in artificial intelligence* (pp. 347–358). Springer International Publishing.
9. Bergstra, J., & Bengio, Y. (2012). Random search for hyper-parameter optimization. *Journal of Machine Learning Research*, *13*(1), 281–305. https://dl-acm-org.tudelft.idm.oclc.org/doi/pdf/10.5555/2188385.2188395
10. Blendermann, W. (1997). *Messung der Windlast an zwei Containerschiffen in realem Ladezustand im Windkanal (Measurements of the Wind Loads on two Container Ships in Real Loading Conditions in Wind Tunnel)*. Institut für Schiffbau der Universität Hamburg.
11. Broos, E., Hoebee, W., Van Scherpenzeel, B., Burgers, J., Schweter, L., & Van Deyzen, A. (2018). Bollard loads on new port infrastructure, Port of Rotterdam Authority Policy. *Proceedings of the 34th PIANC World Congress: Panama City, Panama 2018*. https://pure.tudelft.nl/ws/portalfiles/portal/51686300/Position_paper_bollard_loads_on_port_infrastructure_PIANC_final.pdf
12. Broos, E., Pollmann, J., Dlugosch, J., Hoebee, W., & Kahl, A. (2024). What is a safe working load for your bollard? *Proceedings of the 35th PIANC World Congress: Cape Town, South Africa*.
13. BS 6349-4. (2014). *Maritime works - part 4: Code of practice for design of fendering and mooring systems* (3rd ed.). British Standards Institution.
14. Bunnik, T., & Veldman, A. (2010). Modelling the effect of sloshing on ship motions. *International Conference on Offshore Mechanics and Arctic Engineering*, *49095*, 279–286.
15. C. Andriotis, M. T., L. Mueller. (2024). *Surrogate models*. https://digipedia.tudelft.nl/tutorial/surrogate-models/?tab=chapter-0
16. Campbell, L. A., Butler, J. A., & Donaldson, R. J. (2022). Mooring line failures: Considerations for the installation of barrier protection. In *Australasian coasts & ports 2021: Te oranga takutai, adapt and thrive* (pp. 230–235). New Zealand Coastal Society.

17. Cavotec. (2020). Port of Salalah, Oman [Image]. Retrieved July 11, 2024, from https://www.cavotec.com/en/your-applications/ports-maritime/automated-mooring/container
18. Cavotec. (2024). *Moormaster: Automated mooring*. Retrieved July 11, 2024, from https://www.cavotec.com/en/your-applications/ports-maritime/automated-mooring
19. Christy, A. (2018). *Automated magnetic mooring system* [Image]. Retrieved July 11, 2024, from https://docklockandriver.wordpress.com/tag/automated-magnetic-mooring-system/
20. Couce, J., Carral, L., Formoso, F., & Villa Caro, R. (2015). Standardising the design and production of mooring winches through more cohesive regulations: A necessary step. *The International Journal of Maritime Engineering*, *Vol 157*, IJME 342. https://doi.org/10.3940/rina.ijme.2015.a4.342
21. Cross, J., & Van Deyzen, A. (2023). How ports and terminals can benefit from reduced operational downtime using dynamic mooring analysis. *PIANC COPEDEC X Conference: Manila, Philippines*.
22. CROW. (2021). *Flexible dolphins* (1st ed.). CRC Press.
23. De Boer, G., & Buchner, B. (2005). Viscous damping of vessels moored in close proximity of another object. *Proceedings of the 15th International Offshore and Polar Engineering Conference: Seoul, Korea 2005*, ISOPE-I-05–295.
24. De Bont, J. A. M., Van der Molen, W., Van der Lem, J. C., Mühlestein, D., Ligteringen, H., & Howie, M. (2010). Calculations of the motions of a ship moored with the Moormaster™ units. *Proceedings of the 32nd PIANC International Navigation Congress*, 622–635. http://resolver.tudelft.nl/uuid:c1c4acb0-a626-4eae-8c2a-63e78d493137
25. De Bosscher, B. (2023). *Towards a better understanding of agent-based airport terminal operations using surrogate modeling* [Master's thesis, Delft University of Technology]. http://resolver.tudelft.nl/uuid:e956b58c-1c27-43d2-a707-10006df9e3bc
26. De Gijt, J. G., & Broeken, M. (2013). *Quay walls* (2nd ed.). SBRCURnet.
27. De Gijt, J., & Broeken, M. (2018). *Jetties and wharfs*. SBRCURnet.
28. Dean, M. (2020). Chapter six - multi-criteria analysis. In *Standard transport appraisal methods* (pp. 165–224, Vol. 6). Academic Press. https://doi.org/10.1016/bs.atpp.2020.07.001
29. Delage, T., Zannane, S., & Neveux, T. (2022). Metamodeling of chemical engineering unit operations using kriging and prediction error estimation. In L. Montastruc & S. Negny (Eds.), *32nd european symposium on computer aided process engineering* (pp. 535–540, Vol. 51). Elsevier. https://doi.org/10.1016/B978-0-323-95879-0.50090-4
30. De Roo, F. (2023). *Met hun kleine bootjes leggen deze mannen immense schepen aan de kade: "Mooiste baan van de wereld"*. https://www.bndestem.nl/hoeksche-waard/met-hun-kleine-bootjes-leggen-deze-mannen-immense-schepen-aan-de-kade-mooiste-baan-van-de-wereld~ae5e02c2/
31. Donker, C. (2018). *Jetties and wharfs* [Image]. SBRCURnet.
32. Ebbs-Picken, T., Da Silva, C. M., & Amon, C. H. (2023). Design optimization methodologies applied to battery thermal management systems: A review. *Journal of Energy Storage*, *67*, 107460. https://doi.org/10.1016/j.est.2023.107460
33. Eggermont, C. (2024).
34. Eggermont, C., & Van Deyzen, A. (2023). To improve the orientation of a jetty exposed to swell and current to minimise operational downtime. *Proceedings of the ASME 42nd Internatinal Conference on Ocean, Offshore and Arctic Engineering: Melbourne, Australia 2023*, *Volume 2: Structures, Safety, and Reliability*, V002T02A039. https://doi.org/10.1115/OMAE2023-101382
35. Eskenazi, J., & Wang, J. (2015). Analysis of angular side berthing against a rubber cone fender. *Journal of Shanghai Jiaotong University (Science)*, *20*(5), 571–583. https://doi.org/10.1007/s12204-015-1664-1
36. Faraway, J. (2005). *Linear models with r*. Chapman; Hall/CRC.

37. Fernandes Ramos, R., & Caprace, J. (2018). Analysis of the behavior of moored ships when submitted to the wind force. *27th International Congress on Waterborne Transportation, Shipbeuilding and Offshore Constructions: Rio de Janeiro, Brazil*. https://doi.org/10.17648/sobena-2018-87599
38. Fleer, A., Nguyen, L., Van Deyzen, A., & Eggermont, C. (2024). The effect of mooring line type on mooring safety of Ultra Large Container Ships. *PIANC APAC 2024 Asia Pacific Conference: Sydney, Australia*.
39. Forrester, A., Sobester, A., & Keane, A. (2008). *Engineering design via surrogate modelling: A practical guide*. John Wiley & Sons. https://doi.org/10.1002/9780470770801
40. Gaythwaite, J. W. (2014). *Mooring of ships to piers and wharves*. American Society of Civil Engineers. https://doi.org/10.1061/9780784413555
41. Google Earth. (2024). DDN berth of ECT Delta terminal in Port of Rotterdam.
42. Gourlay, T. P. (2017). Moored ship motions in the Port of Geraldton. *Nautical Institute mooring session*. https://www.perthhydro.com/pdf/Gourlay2017NIMooring.pdf
43. Gourlay, T. P. (2019a). A Coupled Ship and Harbour Model for Dynamic Mooring Analysis in Geraldton Harbour. In *Australasian coasts and ports 2019 conference: Future directions from 40 [degrees] s and beyond, hobart, 10-13 september 2019* (pp. 471–477). Engineers Australia. https://search.informit.org/doi/10.3316/informit.797329177460561
44. Gourlay, T. P. (2019b). Comparison of WAMIT and MoorMotions with Model Tests for a Tanker Moored at an Open Berth. https://www.researchgate.net/publication/337160614_Comparison_of_WAMIT_and_MoorMotions_with_Model_Tests_for_a_Tanker_Moored_at_an_Open_Berth
45. Gourlay, T. P. (2023). Dynamic Mooring Analysis of 6-Buoy Spread-Moored Ships at Cape Cuvier. *Australasian Coasts & Ports 2023 Conference - Sunshine Coast, QLD*. https://www.perthhydro.com/pdf/GourlayPaynterSmith2023.pdf
46. Gravesen, H. (2005). *Moored vessels in ports and at offshore terminals. State of the art*.
47. Gzar, D. A., Mahmood, A. M., & Abbas, M. K. (2022). A comparative study of regression machine learning algorithms: Tradeoff between accuracy and computational complexity. *Mathematical Modelling of Engineering Problems*, *9*(5).
48. Hapag-Lloyd. (n.d.). *Cartagena express*. Retrieved January 11, 2025, from https://www.hapag-lloyd.com/en/services-information/cargo-fleet/vessels/vessel/cartagena-express.html
49. Hastie, T., Tibshirani, R., & Friedman, J. (2009). Overview of supervised learning. *The elements of statistical learning: Data mining, inference, and prediction*, 9–41. https://link.springer.com/content/pdf/10.1007/978-0-387-84858-7_2.pdf
50. Heaton, J. (2008). *Introduction to neural networks with java*. Heaton Research, Inc.
51. Heitmann, C. (2024). Statistics on line types on ultra large container vessels (ulcvs) calling at the port of hamburg [LinkedIn post]. https://www.linkedin.com/posts/christian-heitmann_exciting-insights-from-the-port-of-hamburg-activity-7150424406551433216-qq_Y
52. Hope, T. M. (2020). Chapter 4 - linear regression. In A. Mechelli & S. Vieira (Eds.), *Machine learning* (pp. 67–81). Academic Press. https://doi.org/10.1016/B978-0-12-815739-8.00004-3
53. HTG. (2015). *Recommendations of the Committee for Waterfront Structures Harbours and Waterways: EAU 2012* (9th ed.). John Wiley & Sons.
54. Hutchison Ports ECT Rotterdam. (2024). *Hutchison Ports ECT Delta*. Retrieved October 30, 2024, from https://www.ect.nl/en/terminals/hutchison-ports-ect-delta
55. IACS. (2023). Recommendation 10: Anchoring, Mooring and Towing Equipment. https://iacs.org.uk/resolutions/recommendations/1-20/rec-10-rev5-cln
56. Ides, S., Pauwels, C., & Torfs, P. (2018). Motions of moored vessels due to passing vessels: full-scale measurements at a container temrinal in the port of Antwerp. *PIANC-World Congress Panama City, Panama*.
57. IMO. (2020). Msc.1/circ.1175/rev.1: Revised guidance on shipboard towing and mooring equipment. https://wwwcdn.imo.org/localresources/en/Documents/MSC.1-Circ.1175-Rev.1.pdf

58. Institute for Trade and Transportation Studies. (2009, August). *Comparison between the largest Panamax container vessel and a Post-Panamax size vessel with 12,000 TEUs container capacity*. Retrieved November 5, 2024, from https://www.aapa-ports.org/files/Panamax%20vs%20Post-Panamax%20comparison%20article.pdf
59. Janssen, W., & Van Hell, B. (2023, October). *HydroMeteoBundel nr.5 2023: Statistiek van weer & getij in het rotterdams havengebied*. Havenbedrijf Rotterdam N.V. Retrieved November 1, 2024, from https://www.portofrotterdam.com/sites/default/files/2023-10/HydroMeteoBundel%202023.pdf
60. Jørgensen, U., Mørkrid, O. E., & Røstum Bellingmo, P. (2023). Automated mooring systems. *22nd Conference on Computer and IT Applications in the Maritime Industries (COMPIT' 23)*. https://www.researchgate.net/publication/371183913_Automated_Mooring_Systems
61. Kadhim, Z. S., Abdullah, H. S., & Ghathwan, K. I. (2023). Automatically avoiding overfitting in deep neural networks by using hyper-parameters optimization methods. *International Journal of Online & Biomedical Engineering*, *19*(5). https://doi.org/10.3991/ijoe.v19i05.38153
62. Kołakowski, P., Rutkowski, G., & Łebkowski, A. (2023). Ships-to-ship magnetic mooring systems - the new perspectives. *TransNav: International Journal on Marine Navigation & Safety of Sea Transportation*, *17*(4). https://doi.org/10.12716/1001.17.04.10
63. Kosaraju, N., Sankepally, S. R., & Mallikharjuna Rao, K. (2023). Categorical data: Need, encoding, selection of encoding method and its emergence in machine learning models—a practical review study on heart disease prediction dataset using pearson correlation. In M. Saraswat, C. Chowdhury, C. Kumar Mandal, & A. H. Gandomi (Eds.), *Proceedings of international conference on data science and applications* (pp. 369–382). Springer Nature Singapore.
64. Kuzu, A. C., & Arslan, Ö. (2017). Analytic comparison of different mooring systems. *Global Perspectives in MET: Towards Sustainable, Green and Integrated Maritime Transport*, 265–274.
65. Lamont-Smith, B. (2019). Mooring of dry bulk vessels-practical inputs to terminal mooring design and analysis. *Australasian Coasts and Ports 2019 Conference: Future directions from 40 [degrees] S and beyond, Hobart, 10-13 September 2019*, 728–732.
66. Li, C.-Q., & Yang, W. (2023). 2 - essential reliability methods. In C.-Q. Li & W. Yang (Eds.), *Time-dependent reliability theory and its applications* (pp. 51–119). Woodhead Publishing. https://doi.org/10.1016/B978-0-323-85882-3.00006-4
67. Li, S., & Qiu, Z. (2016). Prediction and simulation of mooring ship motion based on intelligent algorithm. *2016 Chinese Control and Decision Conference (CCDC)*, 1556–1560. https://doi.org/10.1109/CCDC.2016.7531231
68. Li, S., & Qiu, Z. (2017). Modeling and simulation of mooring force prediction based on improved GA-BP network. *Journal of System Simulation*, *29*(7), 1457–1463. https://doi.org/10.16182/j.issn1004731x.joss.201707009
69. Ligteringen, H. (2022). *Ports and terminals*. TU Delft Open. https://doi.org/10.5074/T.2021.005
70. Liu, B.-j., Chen, X.-y., Zhang, Y.-q., Xie, J., & Chang, J. (2020). Influence of regular wave and ship characteristics on mooring force prediction by data-driven model. *China Ocean Engineering*, *34*(4), 589–596. https://doi.org/10.1007/s13344-020-0053-1
71. Ma, K.-T., Luo, Y., Kwan, C.-T. T., & Wu, Y. (2019). *Mooring system engineering for offshore structures*. Gulf Professional Publishing.
72. Mahajan, T., Singh, G., Bruns, G., Bruns, G., Mahajan, T., & Singh, G. (2021). An experimental assessment of treatments for cyclical data. *Proceedings of the 2021 computer science conference for csu undergraduates, virtual*, *6*, 22.
73. MARIN. (2021). Introduction to anysim xmf.
74. MARIN. (2022). Anysim theory documentation.
75. McKenna, H., Hearle, J., & O'Hear, N. (2004). 4 - properties of rope. In H. McKenna, J. Hearle, & N. O'Hear (Eds.), *Handbook of fibre rope technology* (pp. 101–140). Woodhead Publishing. https://doi.org/10.1533/9781855739932.101

76. Mentes, A., & Yetkin, M. (2022). An application of soft computing techniques to predict dynamic behaviour of mooring systems. *Brodogradnja: An International Journal of Naval Architecture and Ocean Engineering for Research and Development*, *73*(2), 121–137. https://doi.org/10.21278/brod73207
77. Messe München. (2023). *Wind measurements by lidar - how does it work?* Retrieved June 7, 2024, from https://world-of-photonics.com/en/discover/photonics-industry-portal/detail/wind-measurements-by-lidar.html
78. Molina-Sanchez, R., Campos, Á., De Alfonso, M., De los Santos, F. J., Rodríguez-Rubio, P., Pérez-Rubio, S., Camarero-Orive, A., & Álvarez-Fanjul, E. (2020). Assessing operability on berthed ships. common approaches, present and future lines. *Journal of Marine Science and Engineering*, *8*(4). https://doi.org/10.3390/jmse8040255
79. Molnar, C. (2025). *Interpretable machine learning: A guide for making black box models explainable* (3rd ed.). https://christophm.github.io/interpretable-ml-book
80. Naciri, M., Waals, O., & de Wilde, J. (2007). Time domain simulations of side-by-side moored vessels: Lessons learnt from a benchmark test. *International Conference on Offshore Mechanics and Arctic Engineering*, *42673*, 801–811.
81. Nasteski, V. (2017). An overview of the supervised machine learning methods. *Horizons. b*, *4*(51-62), 56. https://doi.org/10.20544/HORIZONS.B.04.1.17.P05
82. Natarajan, R., & Ganapathy, C. (1995). Analysis of moorings of a berthed ship [Moored and Tethered Structures]. *Marine Structures*, *8*(5), 481–499. https://doi.org/10.1016/0951-8339(95)97305-R
83. Nejati, E., Ghaedy-Heidary, E., Ghasemi, A., & Torabi, S. A. (2024). A machine learning-based simulation metamodeling method for dynamic scheduling in smart manufacturing systems. *Computers & Industrial Engineering*, *196*, 110507. https://doi.org/10.1016/j.cie.2024.110507
84. *Eurocode – basis of structural and geotechnical design* (Standard). (2025) (European Committee for Standardization). NEN / CEN.
85. Nguyen, A.-D., Kim, Y. S., Kang, G., & Kim, H.-J. (2021). Numerical analysis of static behavior of caisson-type quay wall deepened by grouting rubble-mound. *International Journal of Geo-Engineering*, *12*. https://doi.org/10.1186/s40703-020-00130-3
86. NOAA. (2010a). *Tidal currents*. Retrieved October 15, 2024, from https://oceanservice.noaa.gov/education/tutorial_currents/02tidal1.html
87. NOAA. (2010b). *Tides and water levels*. Retrieved October 15, 2024, from https://oceanservice.noaa.gov/education/tutorial_tides/tides02_cause.html
88. OCIMF. (2018). *Mooring Equipment Guidelines (MEG4)* (4th). Oil Companies International Marine Forum.
89. Oh, M.-J., Ham, S.-H., & Ku, N. (2020). The coefficients of equipment number formula of ships. *Journal of marine science and engineering*, *8*(11), 898. https://doi.org/10.3390/jmse8110898
90. PIANC. (2024). *PIANC Fender Guidelines 2024, report of PIANC MarCom WG211*.
91. Plevris, V., Solorzano, G., Bakas, N. P., & Ben Seghier, M. E. A. (2022). Investigation of performance metrics in regression analysis and machine learning-based prediction models. https://doi.org/10.23967/eccomas.2022.155
92. Port of Rotterdam. (2015). Waalhaven boeien 2015 [Image]. Retrieved July 31, 2024, from https://www.portofrotterdam.com/en/sea-shipping/buoys-and-dolphins/rates-buoy-dolphin-and-public-quay-dues
93. Port of Rotterdam. (2023). *Voorkom losbreken van schepen (Prevent vessels from breaking loose)*. Retrieved October 14, 2024, from https://www.portofrotterdam.com/en/node/2217
94. Port of Rotterdam Authority. (2024a). *Half-Year Report 2024*.
95. Port of Rotterdam Authority. (2024b). *Highlights Annual Report 2023 - Port of Rotterdam Authority*. https://reporting.portofrotterdam.com/FbContent.ashx/pub_1018/downloads/v240305112534/PoR_AR_2023_Annual_Report_Highlights.pdf

96. Prasad, R. K., Ansari, A. R., Equbal, M. A., & Sahu, M. K. (2023). Study and analysis of failure analysis of wire rope [Image]. *Internation Journal of Technology and Emerging Sciences (IJTES)*, *3*, 15–20.
97. Puertos del Estado. (2007). *Rom 3.1-99: Recommendations for the design of the maritime configuration of ports, approach channels and harbour basins*. Retrieved October 15, 2024, from https://www.puertos.es/es-es/BibliotecaV2/ROM%203.1-99%20%28EN%29.pdf
98. Puertos del Estado. (2019). *Rom 2.0-11: Recommendations for the design and construction of berthing and mooring structures* (Vol. 1). Retrieved August 12, 2024, from https://widispe.puertos.es/rom/storage/public/docROM/ROM%202_0-11%20(EN).pdf
99. QuayQuip Technical Solutions BV. (2019). *Bollards & mooring systems* (tech. rep.) (Image). Retrieved August 13, 2024, from https://quayquipts.com/wp-content/uploads/2020/08/QTS-Catalogue-bollards-English-v25c.pdf
100. Remery, G. (1974). Mooring forces induced by passing ships. *Offshore technology conference*, OTC–2066. https://doi.org/10.4043/2066-MS
101. Rijnmond. (2021). “Slimme” bolders moeten ongelukken in de rotterdamse haven voorkomen (“smart” bollards should prevent accidents in rotterdam port) [Image]. https://www.rijnmond.nl/nieuws/203411/slimme-bolders-moeten-ongelukken-in-de-rotterdamse-haven-voorkomen
102. Rodrigue, J. (2024, March 26). *The geography of transport systems*. Routledge. https://doi.org/10.4324/9781003343196
103. Romano-Moreno, E., Diaz-Hernandez, G., Tomás, A., & Lara, J. L. (2023). Multivariate assessment of port operability and downtime based on the wave-induced response of moored ships at berths. *Ocean Engineering*, *283*, 115053. https://doi.org/10.1016/j.oceaneng.2023.115053
104. Romano-Moreno, E., Tomás, A., Diaz-Hernandez, G., Lara, J. L., Molina, R., & García-Valdecasas, J. (2022). A semi-supervised machine learning model to forecast movements of moored vessels. *Journal of Marine Science and Engineering*, *10*(8), 1125. https://doi.org/10.3390/jmse10081125
105. Rosa-Santos, P., Taveira-Pinto, F., & Veloso-Gomes, F. (2014). Experimental evaluation of the tension mooring effect on the response of moored ships. *Coastal Engineering*, *85*, 60–71. https://doi.org/10.1016/j.coastaleng.2013.11.012
106. Roubos, A., Iversen, R., & Oskamp, J. (2024). Background partial energy factors for fender design. *Proceedings of the 35th PIANC World Congress: Cape Town, South Africa 2024*.
107. Royal Institution of Naval Architects. (2017). *Significant ships of 2016*. RINA.
108. Saad, A. M., Schopp, F., Barreira, R. A., Santos, I. H., Tannuri, E. A., Gomi, E. S., & Costa, A. H. R. (2021). Using neural network approaches to detect mooring line failure. *IEEE Access*, *9*, 27678–27695. https://doi.org/10.1109/ACCESS.2021.3058592
109. Sabouri, Z., Gherabi, N., & Amnai, M. (2024). *Comparative study of supervised regression algorithms in machine learning* (N. Gherabi, A. I. Awad, A. Nayyar, & M. Bahaj, Eds.). Springer International Publishing.
110. Sáenz, S. S., Diaz-Hernandez, G., Schweter, L., & Nordbeck, P. (2023). Analysis of the Mooring Effects of Future Ultra-Large Container Vessels (ULCV) on Port Infrastructures. *Journal of Marine Science and Engineering*, *11*(4). https://doi.org/10.3390/jmse11040856
111. Samson Rope. (2024). *Mooring lines* [Image]. Retrieved August 1, 2024, from https://www.samsonrope.com/mooring
112. Scheepvaartwest. (2020). Cartagena Express - IMO 9777618. https://www.scheepvaartwest.be/CMS/index.php/containerships/9978-cartagena-express-imo-9777618
113. Schellin, T., & Östergaard, C. (1995). The vessel in port: Mooring problems. *Marine structures*, *8*(5), 451–479. https://doi.org/10.1016/0951-8339(95)97304-Q
114. Schweter, L., Van Deyzen, A., López, L., & Misiag, W. (2023). The behaviour of a moored ship in wind: The difference between a static and dynamic mooring analysis. *PIANC COPEDEC X Conference: Manila, Philippines*.

115. Scientific metrics. (2022). Tetra Online reference. https://scientificmetrics.com/TetraReference/

116. Shalev-Shwartz, S., & Ben-David, S. (2014). *Understanding machine learning: From theory to algorithms*. Cambridge Uiversity Press.

117. Shams, M. Y., Elshewey, A. M., El-Kenawy, E.-S. M., Ibrahim, A., Talaat, F. M., & Tarek, Z. (2024). Water quality prediction using machine learning models based on grid search method. *Multimedia Tools and Applications*, *83*(12), 35307–35334.

118. Sharma, V. (2022). A study on data scaling methods for machine learning. *International Journal for Global Academic & Scientific Research*, *1*(1), 31–42. https://doi.org/10.55938/ijgasr.v1i1.4

119. ShoreTension. (2024). *Projects*. Retrieved October 14, 2024, from https://shoretension.com/projects/

120. Sidarta, D. E., Auburtin, E., Ledoux, A., Lim, H.-J., Leridon, A., & Tcherniguin, N. (2023). Mooring line failure detection using artificial neural networks: An application to field data including artificial failure cases. *Offshore Technology Conference*. https://doi.org/10.4043/32181-MS

121. Sijberden, H. (2006). *Safe mooring: Bollards in the port of Rotterdam* (1st ed.). Arttechniek.

122. Sivakumar, M., Parthasarathy, S., & Padmapriya, T. (2024). Trade-off between training and testing ratio in machine learning for medical image processing. *PeerJ. Computer science*, *10*, e2245. https://doi.org/10.7717/peerj-cs.2245

123. Sreedevi, R., & Nallayarasu, S. (2023). Investigation on ship mooring forces including passing ship effects validated by experiments. *Ocean Engineering*, *283*, 115004. https://doi.org/10.1016/j.oceaneng.2023.115004

124. Sterkenbrug, S. (2024).

125. Straatman. (2020). *Quick Release Mooring Hooks and Solar systems for Port of Amsterdam*. https://mfstraatman.com/en/news-projects/port-of-amsterdam-becomes-sustainable

126. Sun, Q., Yan, J., Peng, D., Lu, Z., Chen, X., & Wang, Y. (2024). Research on replacing numerical simulation of mooring system with machine learning methods. *Applied Sciences*, *14*(11). https://doi.org/10.3390/app14114759

127. Sundar, K., Nandhini, V., & Nallayarasu, S. (2019). Passing vessel effect on mooring system of a berthed ship - A case study at Jawahar Dweep Berth no: 5, Mumbai Port. *Proceedings of the 4th International Conference in Ocean Engineering (ICOE2018)*, 217–257.

128. Talstra, H., & Bliek, A. (2014). Passing vessel effect on mooring system of a berthed ship. *PIANC World Congress: San Francisco, USA 2014*.

129. Taveira Pinto, F., Veloso Gomes, F., Rosa Santos, P., Guedes Soares, C., Fonseca, N., Santos, J. A., Moreira, A. P., Costa, P., & Bróglueira Dias, E. (2008). Analysis of the behavior of moored tankers. *International Conference on Offshore Mechanics and Arctic Engineering*, *48210*, 755–764. https://doi.org/10.1115/OMAE2008-58013

130. Trelleborg. (2021a). *DynaMoor: a dynamic mooring solution to improve throughput, efficiency and safety*.

131. Trelleborg. (2021b). Interactive DynaMoor Experience [Image]. Retrieved July 10, 2024, from https://www.trelleborg.com/en/media/products-and-solutions-news/interactive-dynamoor-experience

132. Trelleborg. (2024). *AutoMoor - Automated Mooring Solution*. Retrieved July 11, 2024, from https://www.trelleborg.com/en/marine-and-infrastructure/products-solutions-and-services/marine/docking-and-mooring/automated-mooring-systems/automoor

133. UK P&I. (2009). *Understandinge mooring incidents*. https://www.ukpandi.com/media/files/imports/13108/articles/24374-risk_focus5.pdf

134. UNCTAD. (2023, September 28). *Review of maritime transport 2023: Towards a green and just transition*. United Nations publication. https://unctad.org/system/files/official-document/rmt2023_en.pdf

135. Urban, N. M., & Fricker, T. E. (2010). A comparison of latin hypercube and grid ensemble designs for the multivariate emulation of an earth system model. *Computers & Geosciences*, *36*(6), 746–755. https://doi.org/10.1016/j.cageo.2009.11.004

136. US Department of Defense. (2020). *UFC 4-159-03, Moorings*. https://www.wbdg.org/FFC/DOD/UFC/ufc_4_159_03_2020.pdf

137. Van den Boom, H., Pluijm, M., & Pauw, W. (2014). Ropes; joint industry project on effect of passing ships on moored vessels. *PIANC World Congress, San Francisco, USA*.

138. Van der Burg, G. (2011). Shoretension: Secured to shore at all times. *Port technology international*, *52*, 43–46.

139. Van der Molen, W., Scott, D., Taylor, D., & Elliott, T. (2016). Improvement of Mooring Configurations in Geraldton Harbour. *Journal of Marine Science and Engineering*, *4*(1). https://doi.org/10.3390/jmse4010003

140. Van Deyzen, A., Beimers, P., Van der Lem, J., Messiter, D., & De Bont, J. (2015). To improve the efficiency of ports exposed to swell. *Australian Coasts & Ports Conference 2015: Auckland, New Zealand*.

141. Van Deyzen, A., Nguyen, L., & Eggermont, C. (2024). To a safe mooring of large container ships in wind. *35th PIANC World Congress, Cape Town, South Africa*.

142. Van Deyzen, A., Nguyen, L., & Van de Sande, J. (2024). The difference between a Static and Dynamic Mooring Analysis for large container ships in wind. *35th PIANC World Congress: Cape Town, South Africa*.

143. Van Koningsveld, M., Verheij, H., Taneja, P., & de Vriend, H. (2023). *Ports and waterways – navigating the changing world*. Delft University of Technology, Hydraulic Engineering, Ports; Waterways, Delft, The Netherlands. https://doi.org/10.5074/T.2021.004

144. Van Reenen, W. (2013). Dock lock: Automatic magnetic mooring. *United Nations Economic Commission for Europe. 23rd session*. https://unece.org/DAM/trans/doc/2013/dgwp15ac2/Dock_lock_presentation_1.pdf

145. Van Zwijnsvoorde, T., Donatini, L., Van Hoydonck, W., & Lataire, E. (2019). Wind modeling for large container vessels: a critical review of the calculation procedure. *International Journal of Transport Development and Integration*, *3*(4), 369–381. https://doi.org/10.2495/TDI-V3-N4-369-381

146. Van Zwijnsvoorde, T., Eloot, K., Vantorre, M., & Lataire, E. (2019). A mooring arrangement optimisation study. *11th International Workshop on Ship and Marine Hydrodynamics, Hamburg, Germany*. https://www.waterbouwkundiglaboratorium.be/sites/default/files/2022-03/Van%20Zwijnsvoorde_2019.pdf

147. Van Zwijnsvoorde, T., & Vantorre, M. (2017). Safe mooring of large container ships at quay walls subject to passing ship effects. *International Journal of Maritime Engineering*, *159*(A4). https://doi.org/10.3940/rina.ijme.2017.a4.441

148. Van Zwijnsvoorde, T., Vantorre, M., & Ides, S. (2018). Container ships moored at the Port of Antwerp: modelling response to passing vessels. *Proceedings of the 34th PIANC World Congress, Panama City, Panama*, 7–11. https://www.vliz.be/imisdocs/publications/343512.pdf

149. Vieira, S., Lopez Pinaya, W. H., Garcia-Dias, R., & Mechelli, A. (2020). Chapter 9 - deep neural networks. In A. Mechelli & S. Vieira (Eds.), *Machine learning* (pp. 157–172). Academic Press. https://doi.org/10.1016/B978-0-12-815739-8.00009-2

150. Villa, R., Carral, J. C., Fraguela, J., López, M., & Carral, L. (2018). A review of ship mooring systems. *Brodogradnja*, *69*(1), 123–149. https://doi.org/10.21278/brod69108

151. VNO-NCW Regio Rotterdam. (2023). KRVE: 'Rotterdamse lef geeft ons innovatiekracht'. Retrieved October 14, 2024, from https://rotterdamvnoncw.nl/krve-rotterdamse-lef-geeft-ons-innovatiekracht/

152. Wang, C., Duan, Q., Gong, W., Ye, A., Di, Z., & Miao, C. (2014). An evaluation of adaptive surrogate modeling based optimization with two benchmark problems. *Environmental Modelling & Software*, *60*, 167–179. https://doi.org/10.1016/j.envsoft.2014.05.026

153. Weiler, O., Cozijn, H., Wijdeven, B., Le-Guennec, S., & Fontaliran, F. (2009). Motions and mooring loads of an LNG-carrier moored at a jetty in a complex bathymetry. *International Conference on Offshore Mechanics and Arctic Engineering*, *43413*, 425–435. https://doi.org/10.1115/OMAE2009-79420

154. Wiegel, M., De Boer, W., Van Koningsveld, M., Van der Hout, A., & Reniers, A. (2021). Global mapping of seaport operability risk indicators using open-source metocean data. *Journal of Marine Science and Engineering*, *9*(7). https://doi.org/10.3390/jmse9070695

155. Wilhelmsen. (2022). *Towards safer mooring*. Retrieved August 3, 2024, from https://www.wilhelmsen.com/ships-service/ropes/the-new-era-of-safer-mooring/

156. Wilhelmsen. (2023). *Acera lng package* [Image]. Retrieved August 14, 2024, from https://www.wilhelmsen.com/product-catalogue/products/ropes/high-performance-mooring-rope/acera-lng-package/acera-lng-package/

157. Williams, B., & Cremaschi, S. (2019). Surrogate model selection for design space approximation and surrogatebased optimization. In *Proceedings of the 9th International Conference on Foundations of Computer-Aided Process Design* (pp. 353–358, Vol. 47). Elsevier. https://doi.org/10.1016/B978-0-12-818597-1.50056-4

158. Williams, B., & Cremaschi, S. (2021). Novel tool for selecting surrogate modeling techniques for surface approximation. In M. Türkay & R. Gani (Eds.), *31st European Symposium on Computer Aided Process Engineering* (pp. 451–456, Vol. 50). Elsevier. https://doi.org/10.1016/B978-0-323-88506-5.50071-1

159. Wilson, J. F. (2003). Offshore structures (marine engineering). In *Encyclopedia of physical science and technology* (Third Edition, pp. 161–168). Academic Press. https://doi.org/10.1016/B0-12-227410-5/00512-3

160. Xiao, C., Ye, J., Esteves, R. M., & Rong, C. (2016). Using spearman's correlation coefficients for exploratory data analysis on big dataset. *Concurrency and Computation: Practice and Experience*, *28*(14), 3866–3878.

161. Yan, K., Oh, J., & Seo, D.-W. (2023). Computational Analysis for Estimation of Mooring Force Acting on Various Ships in Busan New Port. *Journal of Marine Science and Engineering*, *11*(9), 1649. https://doi.org/10.3390/jmse11091649

162. Yan, K., Zhang, S., Oh, J., & Seo, D.-W. (2022). A review of progress and applications of automated vacuum mooring systems. *Journal of Marine Science and Engineering*, *10*(8), 1085. https://doi.org/10.3390/jmse10081085

163. Yan, M., Zheng, Z., Sun, Z., Ma, X., & Dong, G. (2023). Numerical evaluation of the tension mooring effects on the hydrodynamic response of moored ships under harbor oscillations. *Ocean Engineering*, *288*, 116127. https://doi.org/10.1016/j.oceaneng.2023.116127

164. Ye, X., Zheng, P., Qiao, D., Zhao, X., Zhou, Y., & Wang, L. (2024). Multi-objective optimization design of a mooring system based on the surrogate model. *Journal of Marine Science and Engineering*, *12*(10). https://doi.org/10.3390/jmse12101853

165. Yetkin, M., & Mentes, A. (2015). Optimization of spread mooring systems with artificial neural networks. In C. Guedes Soares, R. Dejhalla, & D. Pavletić (Eds.), *Towards green marine technology and transport* (pp. 233–238). Taylor & Francis Group.

166. Yondo, R., Andrés, E., & Valero, E. (2018). A review on design of experiments and surrogate models in aircraft real-time and many-query aerodynamic analyses. *Progress in Aerospace Sciences*, *96*, 23–61. https://doi.org/10.1016/j.paerosci.2017.11.003

167. Zendehboudi, A., Wang, B., & Li, X. (2017). Robust model to predict the migration ratios of nanoparticles during the pool-boiling process of nanorefrigerants. *International Communications in Heat and Mass Transfer*, *84*, 75–85. https://doi.org/10.1016/j.icheatmasstransfer.2017.03.012

168. Zhi, Y. (2013). *Physical modeling of the motions of a container ship moored to a dock with comparison to numerical simulation* [Master's thesis, Texas A&M University]. https://oaktrust.library.tamu.edu/items/4c41c7c0-8488-4205-8b21-dae023474757

A

Scientific research paper

Prediction of mooring line forces using metamodeling

N.K.S. Wilking

Abstract: The increasing size of cargo vessels poses significant challenges for ports in ensuring safe mooring, as larger ships result in higher mooring forces. Most existing port infrastructure and mooring equipment were designed for smaller ships, making accurate estimation of mooring line forces increasingly critical. Metamodels, machine learning models trained on numerically simulated data, offer a promising alternative to traditional, computationally expensive simulation-based methods by enabling rapid predictions with a useful level of accuracy. This study proposes a metamodeling approach for the numerical Dynamic Mooring Analysis (DMA) to predict mooring line forces from input parameters that describe environmental conditions, mooring systems, and ship characteristics. The methodology is demonstrated in a case study involving a 333-meter container vessel moored at a berth in the Port of Rotterdam. A total of 11,520 scenarios were simulated using the DMA model aNySIM and used to train and test two candidate metamodels: Linear Regression (LR) and Multilayer Perceptron (MLP). After evaluating both models on predictive accuracy, efficiency in terms of prediction speed and development effort, and interpretability, the MLP was selected as the preferred DMA metamodel. It achieved high predictive performance, with an RMSE of 10 kN and an R^2 of 0.996, while offering prediction times measured in microseconds. This is more than seven orders of magnitude faster than the numerical DMA, thereby enabling large-batch predictions.

Keywords: Mooring line forces, Dynamic Mooring Analysis (DMA), Metamodeling, Machine learning, Linear Regression, Multilayer Perceptron (MLP), Large-scale vessels

1. INTRODUCTION

The increasing size of cargo vessels [20] poses significant challenges for ports in ensuring safe mooring operations [24]. Larger ships are subjected to greater environmental forces [14, 23], resulting in higher mooring loads, including increased mooring line forces.

Excessive mooring line forces can lead to catastrophic outcomes. Line failures may cause severe injuries or fatalities to crew members and port personnel. In extreme cases, vessels may break free from their moorings, resulting in collisions with port infrastructure or other ships, causing substantial economic losses and potential environmental damage.

However, most existing port infrastructure and mooring equipment were originally designed for smaller vessels [24]. This growing disparity between vessel size and port infrastructure capacity raises concerns about the safe and efficient mooring of future ship generations. Accurately predicting mooring line forces is therefore essential to assess the operational safety and enable timely mitigating measures.

A moored vessel is subjected to several forces, resulting in a dynamic response involving mooring line tension, fender loads, and ship motion. This response is characterized by three key aspects: environmental conditions, mooring system configuration, and ship characteristics [9].

1.1 Dynamic Mooring Analysis

Dynamic Mooring Analysis (DMA) is a widely used technique to estimate ship response under varying environmental conditions. Based on numerical simulations, DMA solves the moored vessel's six degrees-of-freedom equations of motion in the time-domain (Equation 1), often relying on coupled sub-models [12].

$$F_k(t) = \sum_{j=1}^{6}(M_{kj} + m_{kj})\ddot{x}_j + \int_{-\infty}^{t} R_{kj}(t-\tau)\dot{x}_j(t-\tau)\,d\tau + C_{kj}x_j \quad (1)$$

Where k and j are indices representing the six degrees of freedom; $F_k(t)$ is the external force in mode k, x_j, $\dot{x}_j$, and $\ddot{x}_j$ are the displacement, velocity, and acceleration in motion mode j, respectively; matrix M is the solid inertia; m is the added mass, R is the retardation function modeling memory effects; and C is the hydrostatic restoring force matrix.

Numerous studies have demonstrated the application of numerical models for predicting moored vessel behavior. Weiler et al. [27] combined hydrodynamic scale model tests and time-domain computer simulations to analyze an LNG carrier moored at a jetty with complex bathymetry in Yemen. Van der Molen et al. [21] evaluated various mooring configuration improvements at Geraldton Harbour, which suffers from long wave-induced vessel motions, by

comparing numerical simulations. Van Zwijnsvoorde and Vantorre [22] numerically simulated an 18,000 TEU container vessel at berth, analyzing mooring line forces under passing ship effects. Gourlay [5] developed a coupled ship-and-harbor model to predict wave-induced motions and mooring line and fender loads of moored ships in Geraldton Harbour in Autralia. Sundar, Nandhini, and Nallayarasu [18] performed a comprehensive simulation of mooring line forces due to combined wind, wave, current, and passing ship effects at Mumbai Port. Sáenz et al. [14] investigated the impact of next-generation ULCVs (up to 40,000 TEU) on port mooring systems, by simulating the effects of wind and passing ship forces. Yan et al. [29] employed numerical modeling to analyze the hydrodynamic response of moored ships under harbor oscillations. Gourlay [6] modeled six-buoy spread mooring systems at Cape Cuvier in Australia in order to calculate the wave-induced motions and loads and validated results using field measurements.

1.2 Metamodeling

Metamodeling provides a computationally efficient alternative to numerical simulations. Metamodels, also known as surrogate models [3], represent the response surface of more complex simulation models, by providing simplified approximations. They map inputs to outputs when their underlying relationships are either unknown or computationally expensive to compute [28]. In essence, a metamodel is a "model of a model", offering similar predictive capabilities but at a significantly reduced computational cost [26]. Additionally, they provide valuable insight by facilitating analysis and interpretation of the behavior of the original complex model [1].

Several studies have investigated the use of machine learning (ML) models trained on simulated data to to predict mooring responses. However, these efforts have primarily focused on offshore floating structures. Saad et al. [13] presented two neural networks to predict the movement of a floating platform based on the observation of past time series. The models were trained with simulated motion data generated using actual environmental conditions measured in Rio de Janeiro, Brazil. Mentes and Yetkin [10] proposed an Artificial Neural Network (ANN) and Adaptive Neuro-Fuzzy Inference System (ANFIS) to estimate the mooring line tension and displacements of the spread mooring system of a floating platform or vessel, also using simulated data. Sidarta et al. [16] developed a ANN-based method to detect mooring line failures by identifying subtle shifts in motion patterns of floating offshore platforms. Their model was trained on numerical simulations and tested with modified field data. Sun et al. [17] assessed five ML methods in order to explore a suitable metamodel to replace time-domain numerical simulation for offshore floating structures. Yetkin and Mentes [31] presented a metamodel based on ANN to predict mooring tensions and tanker motion displacements in spread mooring systems. Ye et al. [30] developed a metamodel for floating offshore wind turbines to predict, among other targets, the motion response, incorporating it into a design optimization approach.

1.3 Research goal

Currently, research on ML-based metamodels trained on simulated data for predicting mooring line forces of large-scale vessels in port environments is underexplored.

This study aims to address this gap by developing and evaluating a metamodel trained on DMA-generated data to predict mooring line forces for large-scale vessels moored in ports. The proposed method was demonstrated through a case study at the Port of Rotterdam. To this end, 11,520 scenarios were simulated using DMA to generate training and test data. Two candidate metamodels were developed using Linear Regression (LR) and Multi-Layer Perceptron (MLP) algorithms. These models were evaluated based on multiple objectives to select the most suitable DMA metamodel.

1.4 Outline

The structure of this paper is as follows. Section 2 introduces the proposed metamodeling approach for predicting mooring line forces using numerical simulations from DMA. Section 3 presents the development and evaluation of two candidate metamodels, demonstrated through a case study in the Port of Rotterdam. Finally, Section 4 summarizes the main conclusions and provides recommendations for future work.

2. METHODOLOGY

2.1 Metamodeling process

The construction of metamodels typically involves three stages [26]:

(1) Sample design: selecting representative sample points
(2) Model training: optimizing the model parameters
(3) Model testing: evaluating the accuracy of the model

Sample design The synthetic dataset used for metamodel development is generated through numerical DMA simulations. Each data sample consists of an input scenario, defined by environmental and operational parameters, and the corresponding output, namely the mooring line forces. These input parameters serve as features for the metamodel, while the outputs form the target variables.

These input scenarios are constructed in a structured, three-step process:

(1) Identification of input parameters to be varied.
(2) Definition of the design space for each parameter.
(3) Sampling the set of scenarios.

After generation, the input and output data were preprocessed into usable features and targets. The dataset was then split into training and test subsets and scaled accordingly. The training set was used to fit the model, while the test set was reserved for performance evaluation [15]. Maintaining a balanced train-test split is crucial to prevent overfitting and underfitting.

Training The training phase involves fitting a supervised learning algorithm to the training subset to predict the mooring line forces from the input features.

Predicting mooring line forces based on simulated DMA data represents a Multivariate Multiple Regression problem, characterized by:

- Multivariate input
- Multivariate output
- Continuous numerical output

Testing The test subset is used to evaluate the predictive performance of the trained model. The prediction error, defined by the difference between the true and predicted outputs, is quantified using standard regression metrics [4]. The two metrics used in this study are the Root Mean Squared Error (RMSE) and the coefficient of determination (R^2) [19, 2]. Their expressions are listed in Table 1, where n is the number of samples, y_i the actual output, $\hat{y}_i$ the predicted output, and $\bar{y}$ the mean of the actual output values.

Table 1. Performance evaluation metrics for regression used in this study

Metric	Formula	Value range	Ideal value
RMSE	$\sqrt{\frac{1}{n}\sum_{i=1}^{n}(y_i-\hat{y}_i)^2}$	$[0,+\infty)$	0
R^2	$1-\frac{\sum_{i=1}^{n}(y_i-\hat{y}_i)^2}{\sum_{i=1}^{n}(y_i-\bar{y})^2}$	$(-\infty,1]$	1

2.2 Metamodel interpretability

To gain insights into the model's behavior, feature importance was analyzed using the model-agnostic interpretability tool SHAP (SHapley Additive exPlanations) [11]. SHAP quantifies how each feature contributes to individual predictions, with positive values indicating an increase and negative values indicating a decrease in the predicted output. A SHAP summary plot visualizes these contributions, ranking features by overall importance on the y-axis. Each point represents a SHAP value for a specific feature and instance, with color indicating the feature's value (blue for low, red for high), thereby revealing how different feature values influence the model's predictions.

2.3 Metamodel evaluation and selection

When multiple candidate models are developed, their selection is guided by a multi-objective evaluation framework. In this study, models are assessed according to the following objectives:

- Accuracy
- Efficiency
- Interpretability

Accuracy Accuracy is the most important objective, as the metamodel must reliably approximate mooring line forces in order to serve as a safe surrogate for numerical DMA. Model accuracy is evaluated using:

- RMSE, due to its sensitivity to large prediction errors, and
- R^2, as a complementary indicator of overall goodness-of-fit.

Efficiency Efficiency considered the second most important objective and is assessed based on two criteria:

- Inference time: The time required to make predictions. This is prioritized due to its significance in practical applications, and is a key reason for replacing the computationally intensive numerical model.
- Development effort: This includes the time and resources required for model design, hyperparameter tuning, and training. It indirectly reflects model complexity, but is considered less important as it involves a one-time investment.

Interpretability Although less critical than accuracy or efficiency, interpretability remains important for stakeholder confidence and operational transparency. It is evaluated based on model transparency, reflecting the degree to which the influence of input features on predictions can be understood and explained.

3. CASE STUDY

The proposed metamodeling methodology is applied to a case study in the Port of Rotterdam. It involves a container vessel with a length overall of 333 meters, a length between perpendiculars of 318 meters, a beam of 48 meters, and a draught of 12.15 meters. The vessel is moored at the DNN berth, with all vessel and berth characteristics held constant throughout the analysis.

3.1 Sample design

A total of 11 features were selected from the numerical DMA input parameters, categorized under key aspects that characterize moored vessel response. These features are summarized in Table 2.

Table 2. Input features

Feature	Parameter	Unit
x_1	Water depth	m
x_2	Number of mooring lines	-
x_3	Nylon mooring lines	-
x_4	Polyester mooring lines	-
x_5	MBL	ton
x_6	Pretension	% MBL
x_7	Viscous damping	%
x_8	Wind area	m^2
x_9	Wind velocity	m/s
x_{10}	Cosine of wind direction	-
x_{11}	Sine of wind direction	-

Ranges or sets of discrete values were defined for each input parameter, forming a multidimensional design space. Sampling was conducted using a combination of grid sampling and Latin Hypercube Sampling (LHS). This procedure resulted in 11,520 distinct input scenarios.

Each input scenario was simulated using the numerical DMA model aNySIM, and the corresponding outputs were used to define two target variables, as listed in Table 3.

Table 3. Targets

Target	Parameter	Unit
y_1	Mean mooring line force	kN
y_2	Maximum mooring line force	kN

The target variables are expressed as:

$$y_1 = \frac{1}{N}\sum_{i=1}^{N} F_{i,\text{mean}} \tag{2}$$

$$y_2 = \max_{i\in\{1,\ldots,N\}} F_{i,\text{max}} \tag{3}$$

Where F_i is the force in line i and N the number of lines.

3.2 Model training

Two regression algorithms were selected to develop candidate metamodels: Linear Regression (LR) and Multilayer Perceptron (MLP). Both methods are suitable for multivariate multiple regression tasks and were trained on the designated training subset of the dataset.

LR Linear Regression (LR) is widely used due to its simplicity and interpretability [8]. It models the relationship between multiple input variables and a response variable by fitting a linear function [7]:

$$\hat{y} = \sum_{i=1}^{n} x_i\beta_i + \beta_0 \tag{4}$$

Where $\hat{y}$ is the predicted output, n is the number of features, x_i are the input features, β_i are the feature coefficients, and β_0 is the bias term.

Although LR assumes a linear relationship, which may not fully capture the underlying physics, it serves as a strong baseline and is easy to interpret [8].

MLP The Multilayer Perceptron (MLP) is a popular deep learning model capable of approximating nonlinear relationships [25]. Its architecture includes an input layer, one or more hidden layers with nonlinear activation functions, and an output layer. The output of a hidden neuron is computed as:

$$h_j = f(\sum_{i=1}^{n} w_{ji}x_i) \tag{5}$$

Where h_j is the output of j^{th} hidden neuron in the hidden layer, n is the number of inputs, x_i are the inputs, w_{ji} the weight from input i to hidden neuron j, and f is the activation function.

Hyperparameter optimization is necessary to define the model architecture and training configuration. The optimal set of hyperparameters was identified using 5-fold cross-validation combined with random search and is presented in Table 4.

Table 4. The identified optimal hyperparameter set for the MLP model

Hyperparameter	Optimal value
hidden_layer_sizes	(50, 20)
activation	tanh
solver	sgd
alpha	0.01
learning_rate	adaptive
learning_rate_init	0.1
nesterovs_momentum	True

3.3 Model testing

The predictive performance of the trained models on the unseen test subset is visualized through Actual vs. Prediction plots, presented in Figure 1.

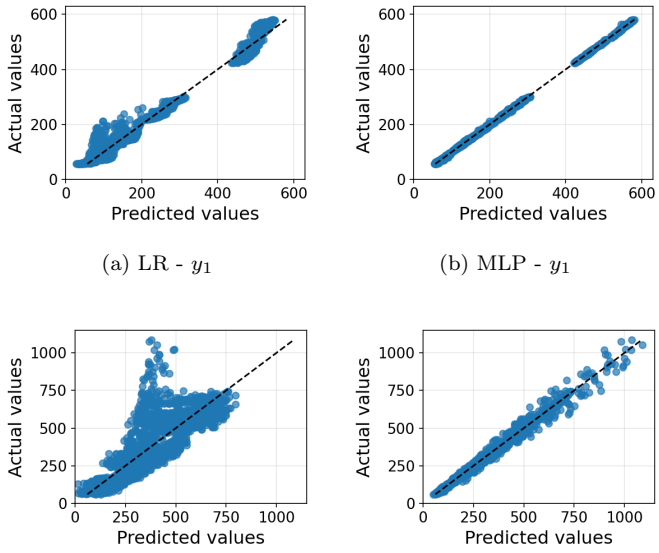

(a) LR - y_1 (b) MLP - y_1

(c) LR - y_2 (d) MLP - y_2

Fig. 1. Actual vs. Prediction plots for both candidate metamodels (LR and MLP) and both target variables (y_1: mean mooring line force, y_2: maximum mooring line force)

Model accuracy was quantified using RMSE and R^2 metrics. Table 5 summarizes these results for the targets y_1 (mean mooring line force) and y_2 (maximum mooring line force).

Both models showed reduced accuracy in predicting y_2, which is likely because it represents the instantaneous peak force. In contrast, y_1 is a time-averaged value and therefore less sensitive to transient fluctuations, making it inherently more predictable.

Table 5. Predictive accuracy of the candidate metamodels

Model	y_1		y_2	
	RMSE	R^2	RMSE	R^2
LR	21	0.9827	111	0.6883
MLP	2	0.9998	18	0.9922

3.4 Model insights

Insight in the models was obtained through feature importance analysis using SHAP summary plots, as shown in Figure 2. The relative importance of the features was generally consistent across the models.

For the prediction of y_1 (mean mooring line force), pretension was the most dominant factor in both models, with a mean absolute SHAP value of approximately 0.82. This was followed by the MBL ($\sim$ 0.10), which had a significantly lower importance.

For y_2 (maximum mooring line force), pretension ($\sim$ 0.56–0.58) and wind velocity ($\sim$ 0.37–0.40) contributed most significantly. The cosine of the wind direction also played a notable role with a mean SHAP value between 0.10 and 0.17.

3.5 Model evaluation

The candidate metamodels were evaluated against the criteria of accuracy, efficiency, and interpretability to support final model selection.

Accuracy The MLP significantly outperformed the LR model on both target variables. It achieved a near-perfect fit for the mean mooring line force (y_1), and demonstrated a substantially better fit for the maximum mooring line force (y_2) compared to the moderate performance of the LR model.

Efficiency Both models offer inference times on the order of microseconds. This marks a significant improvement over to the numerical DMA simulations, which require approximately 30 seconds per run.

However, development effort differed considerably between the models. The MLP required extensive hyperparameter and had longer training times due to its complexity. In contrast, the LR model involved minimal development effort, as it is simple to implement and train, with no hyperparameters to tune.

Interpretability The LR model is inherently interpretable, with coefficients that directly represent the effect of each input feature on the prediction. In contrast, interpreting MLP predictions requires model-agnostic tools such as SHAP values.

Selection Based on the combined evaluation of predictive accuracy, computational efficiency, and interpretability, the MLP model is selected as the final DMA metamodel.

While the MLP involves higher development effort and reduced interpretability compared to the LR model, its superior predictive performance makes it the most suitable surrogate for numerical DMA.

4. CONCLUSION

A methodology was proposed for constructing a metamodel of the numerical Dynamic Mooring Analysis (DMA) to estimate mooring line forces. This approach involves the systematic design a comprehensive DMA dataset, which was used to train and evaluate machine learning models. Candidate models are assessed using three objectives: accuracy, efficiency, and interpretability. This facilitates a quantitative selection of the most suitable DMA metamodel.

The methodology was demonstrated in a case study involving a 333-meter container vessel moored at a quay in the Port of Rotterdam. wo target variables were predicted: the average mean mooring line force per line and the average maximum mooring line force per line. Predictions were based on a set of 11 input features encompassing environmental conditions, and mooring system and ship characteristics. Two candidate metamodels were developed using Linear Regression (LR) and Multilayer Perceptron (MLP) algorithms, and evaluated against the three objectives. The MLP was selected as the preferred metamodel due to its high predictive performance, with an RMSE of 10 kN and an R^2 of 0.996. Additionally, the MLP achieved inference times on the order of microseconds per prediction, significantly faster than the DMA, which requires 30 seconds per simulation. This makes it well-suited for large batch scenario analyses. Despite its "black-box" nature, interpretability was sufficiently addressed through SHAP analysis. It revealed that pretension is clearly the most dominant feature for predicting y_1, followed by MBL. For y_2, the most influential features were identified as pretension, windvelocity, and wind direction (cosine).

This research contributes to bridging the gap in applying metamodeling techniques to DMA, specifically for predicting mooring line forces of large-scale vessels in port environments. The developed metamodel enables fast, data-driven predictions that are grounded in physically meaningful relationships. It can be used as a surrogate for numerical DMA simulations, supporting batch applications such as parameter updating to match field measurements and probabilistic analyses of bollard capacity exceedance over its operational lifetime.

There are two main recommendations for future research:

- Expand the design space: The applicability of the current metamodel is inherently constrained by the training data. Extending the model to cover a broader set of operational conditions involves incorporating wider value ranges and additional features, including diverse vessel types, alternative mooring configurations, and multiple berths. To support this, new simulations should be generated and the metamodel retrained accordingly.
- Explore additional algorithms: Future studies should investigate a broader spectrum of machine learning algorithms to determine whether higher accuracy or computational efficiency can be achieved.

REFERENCES

[1] M. Turrin C. Andriotis L. Mueller. *Surrogate models.* 2024. URL: `https://digipedia.tudelft.nl/tutorial/surrogate-models/?tab=chapter-0`.

[2] D. Chicco, M. Warrens, and G. Jurman. "The coefficient of determination R-squared is more informative than SMAPE, MAE, MAPE, MSE and RMSE in regression analysis evaluation". In: *Peerj computer*

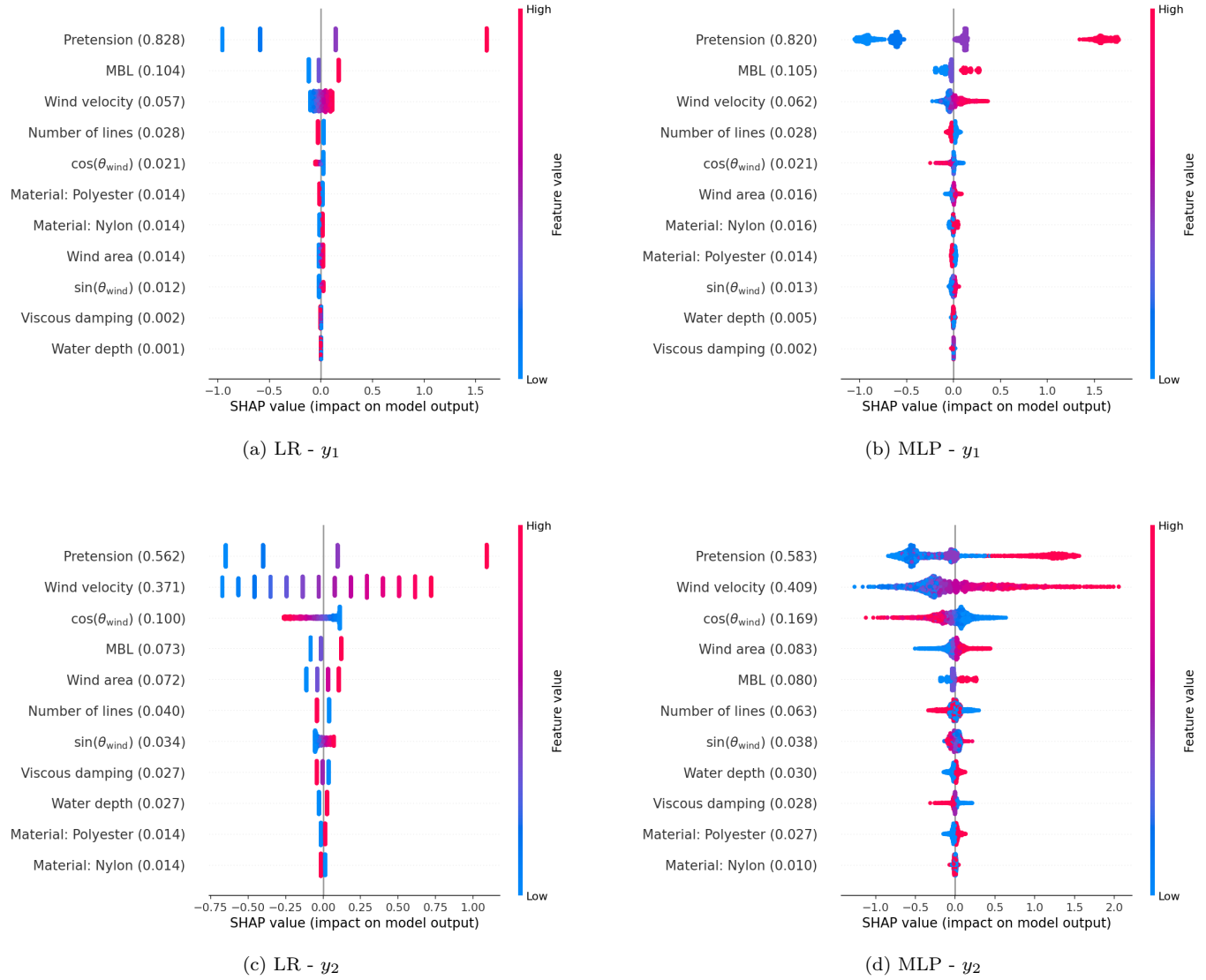

(a) LR - y_1

(b) MLP - y_1

(c) LR - y_2

(d) MLP - y_2

Fig. 2. SHAP summary plots for both candidate metamodels (LR and MLP) and both target variables (y_1: mean mooring line force, y_2: maximum mooring line force)

science 7 (2021), e623. DOI: 10.7717/peerj-cs.623.

[3] T. Delage, S. Zannane, and T. Neveux. "Metamodeling of chemical engineering unit operations using Kriging and prediction error estimation". In: *32nd European Symposium on Computer Aided Process Engineering*. Vol. 51. Computer Aided Chemical Engineering. Elsevier, 2022, pp. 535–540. DOI: 10.1016/B978-0-323-95879-0.50090-4. URL: https://www.sciencedirect.com/science/article/pii/B9780323958790500904.

[4] A. Forrester, A. Sobester, and A. Keane. *Engineering design via surrogate modelling: a practical guide*. John Wiley & Sons, 2008. DOI: 10.1002/9780470770801.

[5] T. Gourlay. "A Coupled Ship and Harbour Model for Dynamic Mooring Analysis in Geraldton Harbour". In: *Australasian Coasts and Ports 2019 Conference: Future Directions from 40 [Degrees] S and Beyond, Hobart, 10-13 September 2019*. Hobart: Engineers Australia, 2019, pp. 471–477. ISBN: 9781925627237. URL: https://search.informit.org/doi/10.3316/informit.797329177460561.

[6] T. Gourlay. "Dynamic Mooring Analysis of 6-Buoy Spread-Moored Ships at Cape Cuvier". In: *Australasian Coasts & Ports 2023 Conference - Sunshine Coast, QLD*. 2023. URL: https://www.perthhydro.com/pdf/GourlayPaynterSmith2023.pdf.

[7] T. Hastie, R. Tibshirani, and J. Friedman. "Overview of supervised learning". In: *The elements of statistical learning: Data mining, inference, and prediction* (2009), pp. 9–41. URL: https://link.springer.com/content/pdf/10.1007/978-0-387-84858-7_2.pdf.

[8] T. Hope. "Chapter 4 - Linear regression". In: *Machine Learning*. Academic Press, 2020, pp. 67–81. ISBN: 978-0-12-815739-8. DOI: 10.1016/B978-0-12-815739-8.00004-3. URL: https://www.sciencedirect.com/science/article/pii/B9780128157398000043.

[9] B. Liu et al. "Influence of regular wave and ship characteristics on mooring force prediction by data-driven model". In: *China Ocean Engineering* 34.4 (2020), pp. 589–596. DOI: 10.1007/s13344-020-0053-1.

[10] A. Mentes and M. Yetkin. "An application of soft computing techniques to predict dynamic behaviour of mooring systems". In: *Brodogradnja: An International Journal of Naval Architecture and Ocean Engineering for Research and Development* 73.2 (2022), pp. 121–137. DOI: 10.21278/brod73207.

[11] Christoph Molnar. *Interpretable Machine Learning. A Guide for Making Black Box Models Explainable*. 3rd ed. 2025. ISBN: 978-3-911578-03-5. URL: https://christophm.github.io/interpretable-ml-book.

[12] E. Romano-Moreno et al. "A Semi-supervised machine learning model to forecast movements of moored vessels". In: *Journal of Marine Science and Engineering* 10.8 (2022), p. 1125. DOI: 10.3390/jmse10081125.

[13] A. Saad et al. "Using neural network approaches to detect mooring line failure". In: *IEEE Access* 9 (2021), pp. 27678–27695. DOI: 10.1109/ACCESS.2021.3058592.

[14] S. Sáenz et al. "Analysis of the Mooring Effects of Future Ultra-Large Container Vessels (ULCV) on Port Infrastructures". In: *Journal of Marine Science and Engineering* 11.4 (2023). ISSN: 2077-1312. DOI: 10.3390/jmse11040856.

[15] S. Shalev-Shwartz and S. Ben-David. *Understanding machine learning: From theory to algorithms*. Cambridge Uiversity Press, 2014.

[16] D. Eka Sidarta et al. "Mooring Line Failure Detection Using Artificial Neural Networks: An Application to Field Data Including Artificial Failure Cases". In: *Offshore Technology Conference*. OTC. 2023. DOI: 10.4043/32181-MS.

[17] Q. Sun et al. "Research on Replacing Numerical Simulation of Mooring System with Machine Learning Methods". In: *Applied Sciences* 14.11 (2024). ISSN: 2076-3417. DOI: 10.3390/app14114759. URL: https://www.mdpi.com/2076-3417/14/11/4759.

[18] K. Sundar, V. Nandhini, and S. Nallayarasu. "Passing Vessel Effect on Mooring System of a Berthed Ship - A Case Study at Jawahar Dweep Berth No: 5, Mumbai Port". In: *Proceedings of the 4th International Conference in Ocean Engineering (ICOE2018)*. Singapore: Springer Singapore, 2019, pp. 217–257. ISBN: 978-981-13-3119-0.

[19] A. Tatachar. "Comparative assessment of regression models based on model evaluation metrics". In: *International Research Journal of Engineering and Technology (IRJET)* 8.09 (2021), pp. 2395–0056.

[20] UNCTAD. *Review of Maritime Transport 2023. Towards a green and just transition*. United Nations publication, Sept. 28, 2023. URL: https://unctad.org/system/files/official-document/rmt2023_en.pdf.

[21] W. Van der Molen et al. "Improvement of Mooring Configurations in Geraldton Harbour". In: *Journal of Marine Science and Engineering* 4.1 (2016). ISSN: 2077-1312. DOI: 10.3390/jmse4010003.

[22] T. Van Zwijnsvoorde and M. Vantorre. "Safe mooring of large container ships at quay walls subject to passing ship effects". In: *International Journal of Maritime Engineering* 159.A4 (2017). DOI: 10.3940/rina.ijme.2017.a4.441.

[23] T. Van Zwijnsvoorde, M. Vantorre, and S. Ides. "Container ships moored at the Port of Antwerp: modelling response to passing vessels". In: *Proceedings of the 34th PIANC World Congress, Panama City, Panama*. 2018, pp. 7–11. URL: https://www.vliz.be/imisdocs/publications/343512.pdf.

[24] T. Van Zwijnsvoorde et al. "Wind modeling for large container vessels: a critical review of the calculation procedure". eng. In: *International Journal of Transport Development and Integration* 3.4 (2019), 369–381. ISSN: 2058-8305. DOI: 10.2495/TDI-V3-N4-369-381.

[25] S. Vieira et al. "Chapter 9 - Deep neural networks". In: *Machine Learning*. Academic Press, 2020, pp. 157–172. ISBN: 978-0-12-815739-8. DOI: 10.1016/B978-0-12-815739-8.00009-2. URL: https://www.sciencedirect.com/science/article/pii/B9780128157398000092.

[26] C. Wang et al. "An evaluation of adaptive surrogate modeling based optimization with two benchmark problems". In: *Environmental Modelling & Software* 60 (2014), pp. 167–179. ISSN: 1364-8152. DOI: 10.1016/j.envsoft.2014.05.026. URL: https://www.sciencedirect.com/science/article/pii/S1364815214001698.

[27] O. Weiler et al. "Motions and mooring loads of an LNG-carrier moored at a jetty in a complex bathymetry". In: *International Conference on Offshore Mechanics and Arctic Engineering*. Vol. 43413. 2009, pp. 425–435. DOI: 10.1115/OMAE2009-79420.

[28] Bianca Williams and Selen Cremaschi. "Novel Tool for Selecting Surrogate Modeling Techniques for Surface Approximation". In: *31st European Symposium on Computer Aided Process Engineering*. Ed. by M. Türkay and R. Gani. Vol. 50. Computer Aided Chemical Engineering. Elsevier, 2021, pp. 451–456. DOI: 10.1016/B978-0-323-88506-5.50071-1.

[29] M. Yan et al. "Numerical evaluation of the tension mooring effects on the hydrodynamic response of moored ships under harbor oscillations". In: *Ocean Engineering* 288 (2023), p. 116127. ISSN: 0029-8018. DOI: 10.1016/j.oceaneng.2023.116127.

[30] X. Ye et al. "Multi-Objective Optimization Design of a Mooring System Based on the Surrogate Model". In: *Journal of Marine Science and Engineering* 12.10 (2024). ISSN: 2077-1312. DOI: 10.3390/jmse12101853. URL: https://www.mdpi.com/2077-1312/12/10/1853.

[31] M. Yetkin and A. Mentes. "Optimization of Spread Mooring Systems with Artificial Neural Networks". In: *Towards Green Marine Technology and Transport*. Ed. by C. Guedes Soares, R. Dejhalla, and

D. Pavletić. London: Taylor & Francis Group, 2015,
pp. 233–238. ISBN: 978-1-138-02887-6.

B

Input scenarios for the case study

B.1. Berth and ship specifics

B.1.1. Berth

The DDN quay (Figure B.1) is a closed structure with sheet pile walls and has a height of +3.52 meters NAP. It is orientated from 263° to 83° (Google Earth, 2024) and is equipped with 1000 kN capacity bollards, installed in pairs. Cylindrical sideloaded rubber fenders are mounted to to the quay wall, with fender pairs positioned at +1.00 m NAP and single fenders at -1.20 m NAP. This configuration ensures that the lower fenders remain submerged at all times, while the upper fenders are only submerged during high tide. The average seabed depth at the berth is at -17.20 m NAP. In Figure B.2 the exact arrangement and spacing between the bollards and fenders is illustrated.

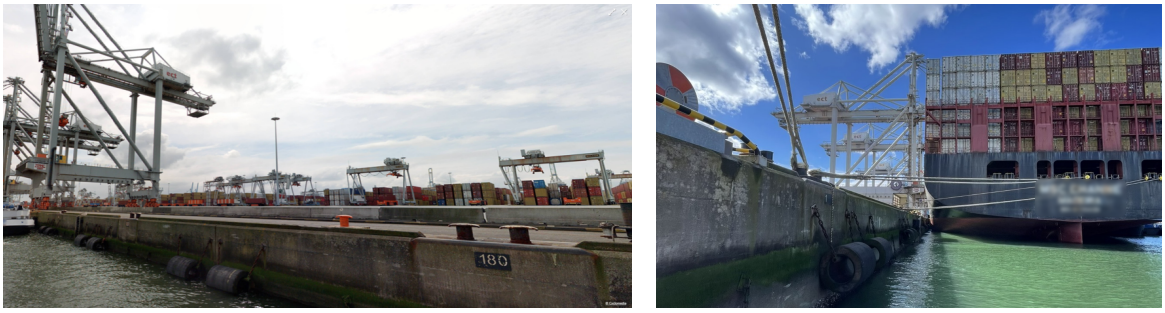

(a) (Port of Rotterdam, 2024)

(b) DDN berth viewed from the landside

Figure B.1: Views of the DDN berth from the waterside

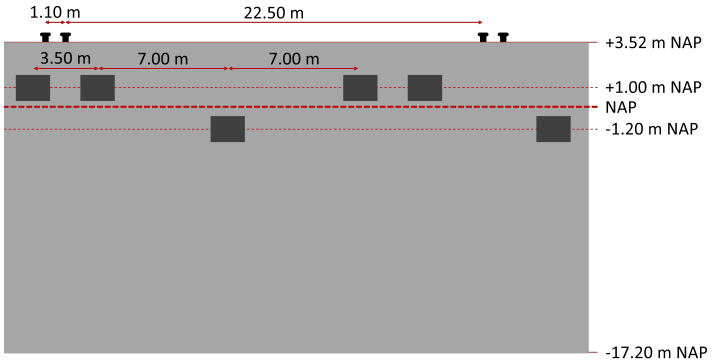

Figure B.2: Illustration of the DDN berth front view, showing the arrangement and spacing of bollards and fenders, and the seabed depth

B.1.2. Moored vessel

Sterkenbrug (2024) of the KRVE states that the average size of vessels moored at the DDN berths varies throughout the year. Over the entire year, a ship length of 333 m approximates the average.

For this reason, the considered ship is the Cartagena Express (Figure B.3), which has a length overall (L_{oa}) of 333 m, length between perpendiculars (L_{pp}) of 318 m, and beam (B) of 48 m.

Figure B.3: Cartagena Express (D. Hasenpusch, n.d.)

The load condition, and so the number of containers on deck, will vary between the scenarios. However, the mass of the vessel and thus the draught will be kept constant for simplicity reasons, so the defined draught should represent all scenarios.

In recent years, the average draught of the Cartagena Express was 12.75 meter when visiting the DDN berth. According to Royal Institution of Naval Architects (2017) her sister ship, the Valparaiso Express, shares the same dimensions and a scantling draught and a design draught of 14 m and 12.5 m, respectively. The estimation is that the draught of a half-loaded Cartagena Express will be around 12.25 m. This draught (T) is therefore assumed for all simulated scenarios. The displacement corresponding to this draught is 1.253E+5 m^3.

The deck plan of the ship is obtained from the sister ship Valparaiso Express according to Royal Institution of Naval Architects (2017), assuming similar layouts.

The deck plan of the vessel is based on that of its sister ship, the Valparaiso Express, as described by Royal Institution of Naval Architects (2017), under the assumption of a similar layout.

B.2. Varying input parameters

B.2.1. Water level

In the port of Rotterdam the water level is currently measured by water level radars in the monitoring network of the Port of Rotterdam. These fixed radars measure the distance to the water level. Previously, measurements were conducted using floats, known as “vlotters”. At the EURH location (Figure B.4), the average low water and high water levels were +1.28 m NAP and -0.67 m NAP, respectively, as measured from 2002 to 2022 (Janssen & Van Hell, 2023). The average seabed depth is at -17.20 m NAP.

In all simulations, the water level is set to the average minimum water level during low tide and the maximum during high tide at the DDN berth. These levels are 16.53 m (-0.67 m NAP) and 18.48 m (+1.28 m NAP), respectively.

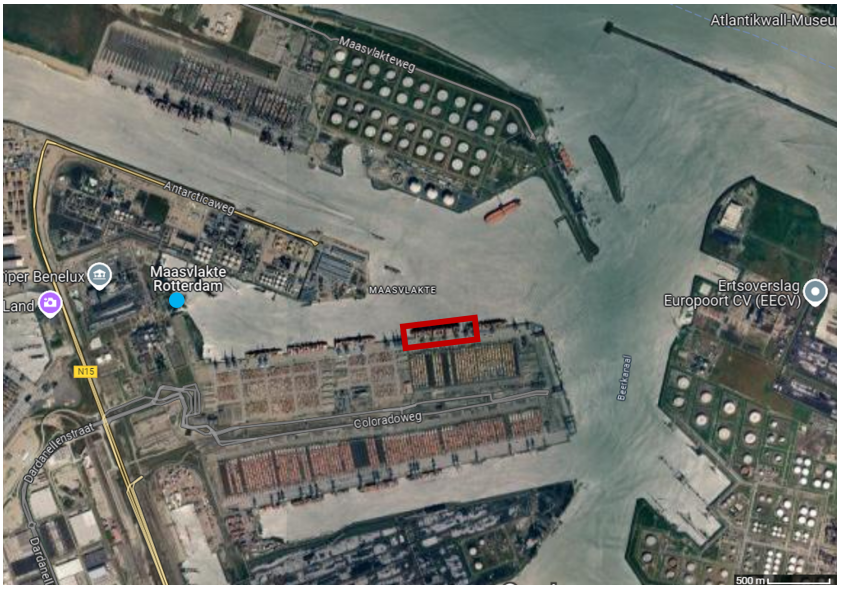

Figure B.4: Location of the water level radar EURH (orange dot) and DDN berth (red rectangle)

B.2.2. Mooring line configuration

Container vessels of this size are typically moored using a 4-to-2 configuration, which involves four breast lines and two spring lines on each side (stern and bow), totaling six mooring lines per side and twelve lines overall. Occasionally a 5-to-2 or 6-to-2 mooring arrangement may be used, but this depends on the weather conditions and available space on the quay (Sterkenbrug, 2024). At the DDN berth, vessels are generally moored to port side. The terminal decides whether vessels should be moored starboard of port side (Sterkenbrug, 2024).

The simulated scenarios considered two distinct mooring line configurations for port side mooring: one with 12 lines (Figure B.5a) and another with 16 lines (Figure B.5b).

The line numbering system for this vessel utilizes a consistent approach. Lines are numbered from aft to bow, from 1 to 12. This numbering remains consistent between the 12-line and 16-line configurations, ensuring each number corresponds to the same physical line.

The 12-line configuration typically employs a 4-to-2 mooring arrangement: four breast lines and two spring lines on each side.

The 16-line configuration, observed on the Cartagena Express on January 22, 2024, utilizes a 6-to-2 mooring arrangement: six breast lines and two spring lines on each side. This 16-line configuration includes four additional lines: 13 and 14 at the aft, and 15 and 16 at the bow.

(a) 12-line configuration

(b) 16-line configuration

Figure B.5: The two line configurations in the scenarios

The 12-line configuration is derived from the 16-line configuration by simply removing lines 13, 14, 15, and 16, leaving the vessel with the standard 12-line mooring setup.

B.2.3. Line material

The DDN berths serve primarily slightly older vessels that typically use nylon or polyester mooring lines. While HMSF lines are occasionally observed, steel wires have not been used for container ships for the past 15 years. Tails are used only in combination with HMSF or steel lines (Sterkenbrug, 2024).

Therefore, in the simulation scenarios, nylon or polyester mooring lines were chosen, with all lines being of the same material.

B.2.4. MBL

In the Port of Rotterdam, there is no data available on the MBL of used lines of the accommodated vessels.

The MBL of mooring lines is unknown to the boatmen, however, the specifications and usage of the lines are required to be recorded in the vessel's onboard logbook (Sterkenbrug, 2024).

However, in the ports of Antwerp and Hamburg is some limited information known about mooring lines.

A monitoring campaign conducted by Ides et al. (2018) at a container terminal in Antwerp focused on vessels exceeding Panamax size (over 4,500 TEU (Institute for Trade and Transportation Studies, 2009)). The study revealed variability in line types, even among ships of the same class. The MBL for 400-meter vessels appears to be relatively consistent, with 140 tons as a representative value (Van Zwijnsvoorde, Eloot, et al., 2019).

In the Port of Hamburg the line types and MBLs vary as well for ULCVs as can be seen in Table B.1.

Table B.1: Observed line types for Ultra Large Container Vessels (ULCVs) at Hamburg Port by ship size, based on Heitmann (2024)

Line type	300 - 330m		360m		400m	
	Percentage	Avg. MBL (t)	Percentage	Avg. MBL (t)	Percentage	Avg. MBL (t)
HMSF	5.33%	136	11%	137	34%	155
PE / PET / PP	43.33%	120	40%	129	38%	131
PA / Nylon	51.33%	114	49%	132	28%	153

Based on this data and discussions with representatives from the Port of Rotterdam, it was decided to use MBLs of 120, 130, and 150 tonnes in the scenarios for both the nylon and polyester mooring lines.

B.2.5. Pretension

The pretension in the mooring lines varies over time, depending on water level and draught. If the winches are set to auto-tension mode, they attempt to maintain a constant tension in the lines. When a winch is on the brake, the vessel crew is responsible for managing and adjusting the tension in the mooring line. The Smart Bollards installed on the DDN berth sometimes measure loads visibly increasing with the tide, resulting in very large mooring line tensions. This indicates poor management of the lines by the vessel crew.

All lines in each scenario are set to the same initial tension, which is a percentage of the MBL. Pretensions of 5%, 10%, 20%, and 40% of the MBL were chosen for the scenarios to cover a range from low to very high pretensions.

B.2.6. Wind area

The exact dimensions of sister ship Valparaiso Express and her technical drawings (Figure B.6) are obtained. Using the drawings, the wind areas of the load conditions on deck of 100%, 80%, 60% and 40% are defined in square meters as illustrated in Figure B.7.

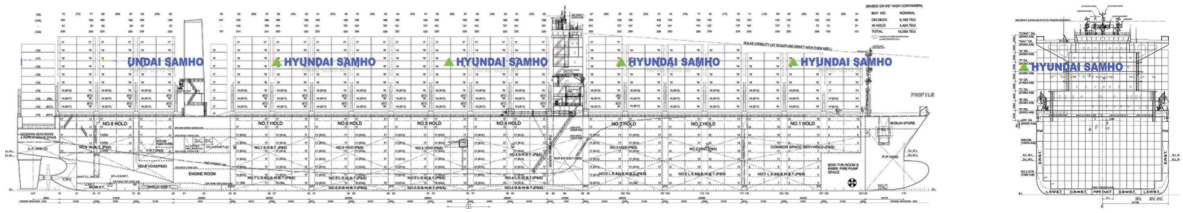

(a) Side view **(b)** Front view

Figure B.6: Midship section of the Valparaiso Express (Royal Institution of Naval Architects, 2017)

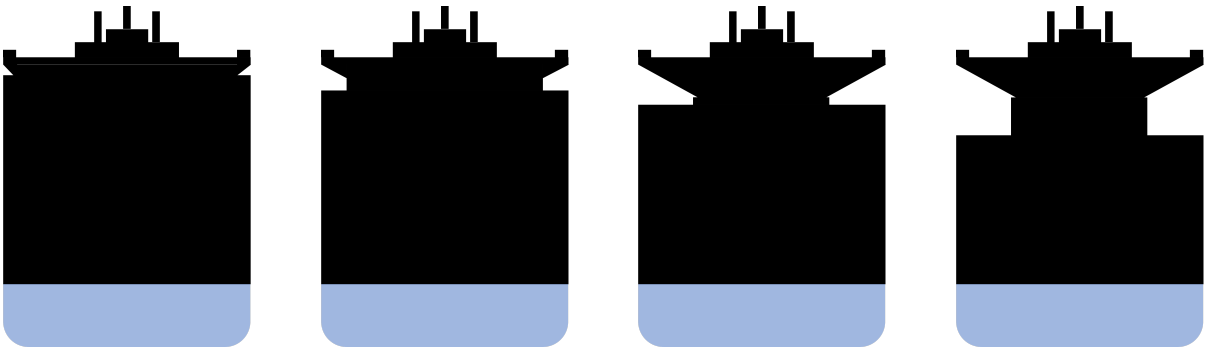

(a) 100% **(b)** 80% **(c)** 60% **(d)** 40%

Figure B.7: Wind-exposed areas (in black) for the Cartagena Express under varying deck load conditions, expressed as percentages of the total containers on deck. The underwater hull, corresponding to a draught of 12.25 m, is shown in blue.

Wind area (%)	Front area (m^2)	Side area (m^2)
100	2,242	11,378
80	2,210	10,340
60	2,138	9,303
40	2,009	8,266

Table B.2: The front and side areas of the vessel exposed to wind

B.2.6.1. Shielding of the quay

The presence of the quay provides wind shielding, which is accounted for by reducing the effective side wind area of the vessel. This reduction is calculated by subtracting the area shielded by the quay, which is determined as the product of the vertical distance between the water level and the quay height, and the vessel's length between perpendiculars L_{pp}.

The quay height is 3.52 m relative to Nederlands Amsterdams Peil (NAP). The shielded area varies depending on the water level:

- Low tide: The water level is at -0.67 m NAP, resulting in a vertical difference of $3.52 + 0.67 = 4.19$ m. The corresponding shielded area is:

$$A_{\text{shield, low}} = 318 \cdot 4.19 = 1,332.42 \text{ m}^2$$

- High tide: The water level is at +1.28 m NAP, resulting in a vertical difference of $3.52 - 1.28 = 2.24$ m. The corresponding shielded area is:

$$A_{\text{shield, high}} = 318 \cdot 2.24 = 712.32 \text{ m}^2$$

B.2.6.2. Wind coefficients

There are several methods to determine the aerodynamic drag coefficients or wind coefficients of a ship, including Computational Fluid Dynamics (CFD) modeling, wind tunnel tests, and other techniques. For this project, coefficients obtained from wind tunnel tests were chosen.

According to practice, wind coefficients can be used for similar ships. The selection of the modeled ship is based on the ship size, the superstructure arrangement on deck, and the mean height, which is the wind area divided by the overall length of the ship.

Marikom (2015) conducted wind tunnel tests on two ship models commissioned by the Hamburg Port Authority. These ship models had different draughts and loading conditions. The Globe, with a draught of 13 meters and partially loaded with 7 tiers of containers (Figure B.8), most closely resembles the Cartagena Express, which has a draught of 12.25 m and varying simulated wind areas in the scenarios. Therefore, the wind coefficients from the Globe tests have been adopted for the case study.

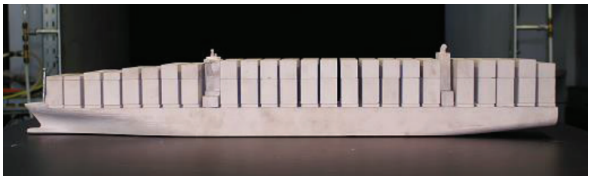

Figure B.8: Model of the Globe, fully loaded with draught of 10 m (Marikom, 2015)

Figure B.9: Side view of the Cartagena Express (Hapag-Lloyd, n.d.)

B.2.7. Viscous damping

Viscous damping is due to the flow between ship, quay, and seabed. It depends on the distance between the quay structure and the moored vessel, as well as the water depth (De Boer & Buchner, 2005). Additionally, it is sensitive to the type of quay structure, whether it is a closed quay or an open deck on piles.

Figure B.10: Effects of damping (De Boer & Buchner, 2005)

Not much is known about this topic, except what has been published in De Boer and Buchner (2005). For a ship moored to a quay wall, it is assumed for now that a viscous damping of 1 to 3% of the critical damping in the surge, sway, and yaw direction is appropriate.

Critical damping is calculated by formula, total mass (including mass of the ship and added mass) and natural frequency ω_{n} in rad/s.

For linear motions (surge, sway, heave):

$$b_{\text{cr}} = 2 \cdot m_{\text{total}} \cdot \omega_{\text{n}} \tag{B.1}$$

For rotations (roll, pitch, yaw):

$$b_{\text{cr}} = 2 \cdot (I_z z + m_{\text{added}}) \cdot \omega_{\text{n}} \tag{B.2}$$

Where

b_{cr}	critical damping per direction [N.s/m] for linear motions
m_{total}	total mass (ship's mass and added mass) per direction [kg]
ω_{n}	natural frequency [rad/s] per direction
I_{zz}	[kg.m^2]
m_{added}	added mass per rotation direction [kg]

The natural frequency is calculated for every base case using this formula:

$$\omega_{\text{n}} = \sqrt{\frac{C}{m_{\text{total}}}} \tag{B.3}$$

Where

ω_{n}	natural frequency per direction[rad/s]
C	stiffness per direction [N/m]
m_{total}	total mass (ship's mass and added mass) per direction [kg]

Note: The stiffness and added mass have different values in each direction (surge, sway, heave, roll, pitch, yaw), so the natural frequency (ω_{n}) is direction-dependent.

The total damping includes the viscous damping and "wave-making" damping obtained from the Hyd-files. A Hydfile provides wave-making damping b per water level. Therefore, for the 11,520 scenarios, there are two sets of b-values from the Hydfile. The total damping is assumed to be a percentage of the critical damping, often in the range of 1 to 3%, as direct measurements are not possible.

$$b_{\text{total}} = b + b_{\text{visc}} = \text{percentage} \cdot b_{\text{cr}} \tag{B.4}$$

Where

b_{total}	total damping per direction in [N.s/m] for linear motions and [N.m.s] for rotations
b	wave-making damping per direction in [N.s/m] for linear motions and [N.m.s] for rotations
b_{visc}	viscous damping per direction in [N.s/m] for linear motions and [N.m.s] for rotations
percentage	assumed percentage [%]
b_{cr}	critical damping per direction in [N.s/m] for linear motions and [N.m.s] for rotations

Thus, the viscous damping can be calculated by taking the assumed total damping and subtracting the "wave-making" damping.

For the scenarios, total damping values of 0%, 2%, and 4% of the critical damping are selected, all resulting in different viscous damping values. For simplicity, equal percentages are assumed for surge, sway, yaw direction. Damping in the heave, roll, and pitch directions is not considered.

B.2.8. Wind

Port of Rotterdam uses cup anemometers and wind vanes to measure the wind velocity and direction at various locations in the port. A cup anemometer consists of a rotating cup element which is driven by wind. The rotation produces an electric voltage signal, where the signal's magnitude is proportional to the wind velocity. The wind vane features a rigid metal plate mounted on a rotating axis. As the wind turns the vane, its position is registered to represent the wind direction (Janssen & Van Hell, 2023).

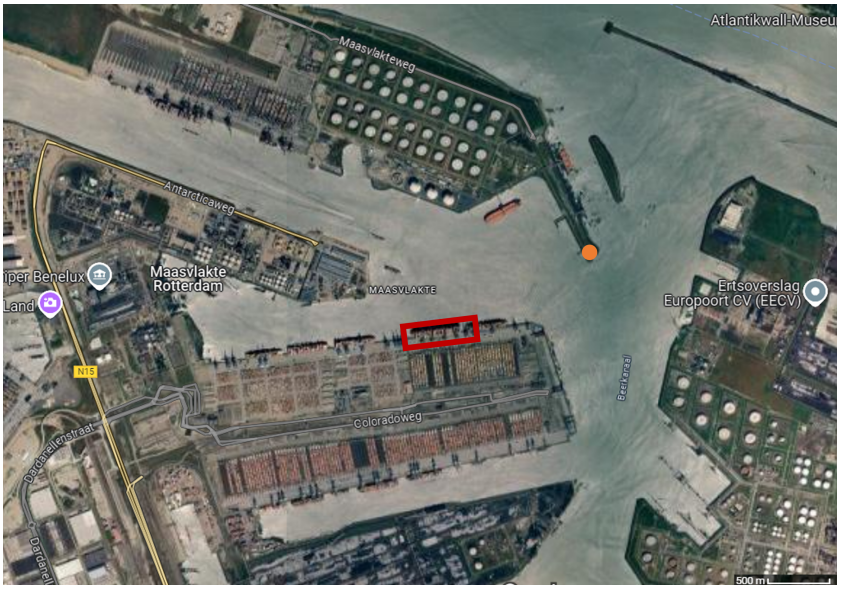

Figure B.11: Location of Beerkanaal Radarpost 37 (orange dot) and DDN berth (red rectangle)

The wind sensor installed at Beerkanaal Radarpost 37 (Figure B.11) is used by the Rotterdam Port Authority to record the wind and is the closest wind sensor to the DDN berth. In 2009-2019, south-wester winds were measured most frequently and the most common wind force was 0-3 Beaufort, followed by 4 Beaufort, and 5 Beaufort as visualized in Figure B.12.

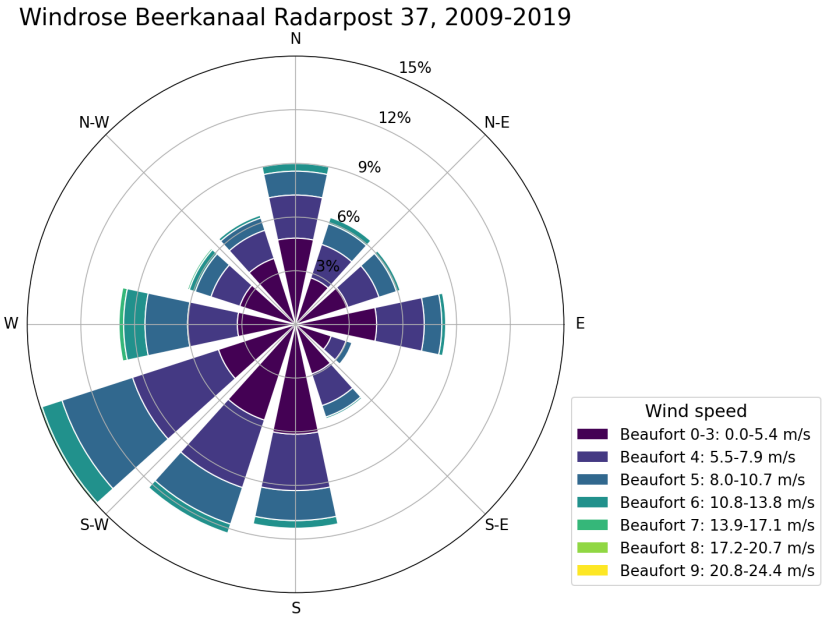

Figure B.12: Wind rose plot of Beerkanaal Radarpost 37 2009-2019, based on Janssen and Van Hell (2023)

The underlying data are the 10-minute average wind speed and direction.

For vessels with an approximate length of 333 m, the limiting wind speeds are 10-15 m/s and the critical sector are off-quay wind directions, meaning 90° +- 45° relative to the ship (Van Deyzen, Nguyen, & Van de Sande, 2024; Van Deyzen, Nguyen, & Eggermont, 2024).

The designed scenarios feature wind speeds ranging from 5 to 18 m/s, corresponding to moderate (Beaufort 3) to storm-force winds (Beaufort 8). As the wind most frequently comes from the south-west, it was decided to model the wind from 173° to 263°, covering directions from perpendicular to parallel to the quay, as illustrated in Figure B.13.

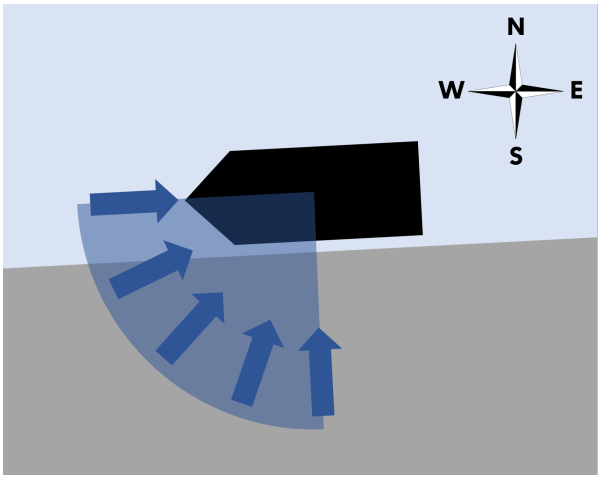

Figure B.13: Wind directions in the simulated scenarios are in the range of 173° to 263°

C

DMA data analysis

C.1. Raw DMA outputs analysis

To gain insights into how mooring forces are distributed across individual lines, the raw DMA output was analyzed separately for scenarios with 12 and 16 deployed mooring lines. This distinction is important as the number and configuration of lines directly influence how the total force is distributed.

Figure B.5 illustrates the line numbering and layout for both the 12-line and 16-line configurations.

C.1.1. Mean mooring line force

The first target variable, y_1, is the average mean force per line, denoted by $\bar{F}_{\text{mean}}$. It is calculated for each scenario by taking the sum of the mean forces across every deployed line i and dividing by the number of lines N:

$$\bar{F}_{\text{mean}} = \frac{1}{N} \sum_{i=1}^{N} F_{i,\text{mean}}$$

To analyze the contribution of each individual line, the force in each line was expressed as a percentage of the scenario's $\bar{F}_{\text{mean}}$. These percentages were then averaged across all scenarios to reveal how each line typically contributes relative to the average.

Table C.1 presents, for each mooring line, the average absolute mean force and the average relative contribution to the total mean force ($\bar{F}_{\text{mean}}$), separately for the 12-line and 16-line configurations. This provides insight into how individual lines contribute to the overall mooring load distribution across different system configurations.

Table C.1: Average mean mooring line forces per line and their relative contribution to the total mean force, for both 12-line and 16-line configurations

Line number	12-line configuration		16-line configuration	
	Average mean force $\bar{F}_{i,\text{mean}}$ (kN)	**Average % of $\bar{F}_{\text{mean}}$**	**Average mean force $\bar{F}_{i,\text{mean}}$ (kN)**	**Average % of $\bar{F}_{\text{mean}}$**
1	246.07	96.25	243.26	99.19
2	242.73	94.52	237.71	96.54
3	244.95	96.84	240.60	99.21
4	236.30	92.87	226.16	92.86
5	276.82	114.46	298.64	127.60
6	271.06	110.91	288.67	122.26
7	233.23	84.83	202.65	80.44
8	221.50	84.01	197.97	78.44
9	249.82	107.63	228.86	102.65
10	242.80	102.69	215.17	95.00
11	258.85	109.16	251.33	109.86
12	252.87		237.94	103.46
13	-	-	229.85	91.80
14	-	-	226.27	90.01
15	-	-	237.91	102.86
16	-	-	255.32	107.84
Average $\bar{F}_{\text{mean}}$	247.25	-	238.64	-

Figure C.1 illustrates the average mean force per mooring line, along with the overall average mean force across all lines.

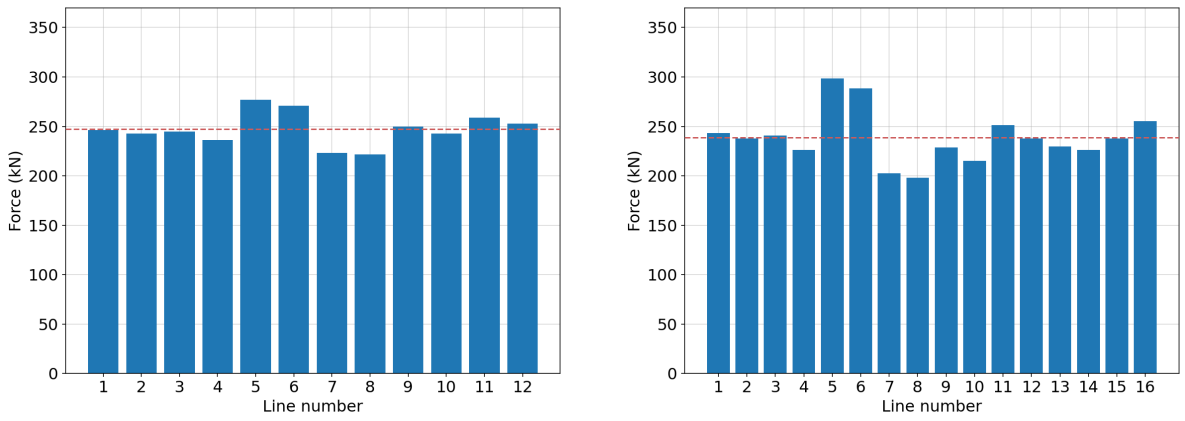

(a) 12-line configuration

(b) 16-line configuration

Figure C.1: Average mean mooring line forces per line for the 12-line and 16-line systems. The blue bars represent the average mean force per individual line. The red dashed line indicates the overall average mean line force across all lines in the system.

C.1.2. Maximum mooring line force

The second target variable, y_2, is the maximum peak force among all N mooring lines in a given scenario, denoted as F_{max}:

$$F_{\text{max}} = \max_{i \in \{1,\ldots,N\}} F_{i,\text{max}}$$

To better understand which lines are typically subjected to peak loads, the average maximum force

per line was computed over all scenarios. Besides, for each scenario, the peak force in each line was expressed as a percentage of that scenario's maximum peak force. These values were then averaged across all scenarios.

Table C.2 summarizes, for each mooring line, the average absolute maximum force and its relative percentage compared to the highest maximum force observed across all lines, separately for the 12-line and 16-line configurations.

Table C.2: Average maximum mooring line forces per line and their relative contribution to the highest maximum force, for both 12-line and 16-line configurations

Line number i	**12-line configuration**		**16-line configuration**	
	Average maximum force $\bar{F}_{i,\text{max}}$ **(kN)**	**Average % of** F_{max}	**Average maximum force** $\bar{F}_{i,\text{max}}$ **(kN)**	**Average % of** F_{max}
1	283.15	78.58	270.81	76.52
2	280.49	77.73	265.28	74.84
3	302.28	81.96	282.90	79.44
4	302.54	81.05	273.82	76.37
5	315.50	91.48	326.16	95.95
6	301.94	87.61	310.65	91.05
7	243.42	69.50	215.69	61.81
8	245.15	69.66	213.20	61.00
9	328.48	90.90	283.40	82.87
10	315.45	86.75	265.27	76.93
11	316.75	89.44	291.76	85.38
12	311.05	87.09	278.13	80.93
13	-	-	244.63	69.41
14	-	-	239.61	68.03
15	-	-	275.68	80.09
16	-	-	277.96	80.77
Average F_{max}	359.72	-	346.02	-

Figure C.2 presents the average maximum force per mooring line, as well as the overall average maximum force across all lines.

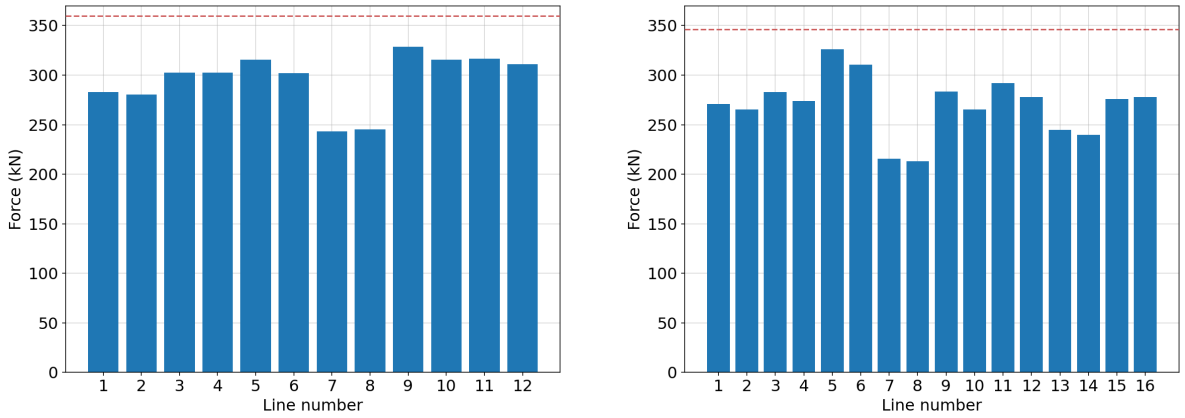

(a) 12-line configuration

(b) 16-line configuration

Figure C.2: Average maximum mooring line forces per line for the 12-line and 16-line systems. The blue bars represent the average maximum force per individual line. The red dashed line indicates the overall average maximum line force across all lines in the system.

C.2. Distributions, scatter plots, and correlation analysis

This section presents an exploratory analysis of the DMA dataset comprising 11,520 simulated scenarios. Each scenario corresponds to a unique combination of input features (Table 4.5) and the resulting target values: the mean mooring line force ($\bar{F}_{\text{mean}}$) and maximum mooring line force (F_{max}), both computed via numerical DMA.

The analysis includes frequency plots of the target variables in Subsection C.2.1. Subsection C.2.2 presents the sampled distribution of each feature and includes scatter plots illustrating its relationship with the target values. Additionally, Spearman's rank correlation coefficient (r_s) is used to quantify the monotonic association between each feature and the targets.

C.2.1. Target distributions

The distributions of the two target values over all scenarios are shown in Figure C.3.

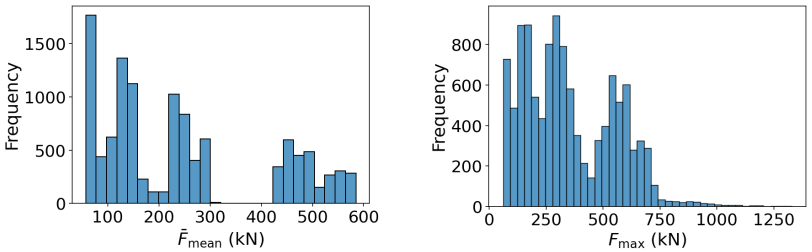

(a) $\bar{F}_{\text{mean}}$

(b) F_{max}

Figure C.3: Distribution of the calculated target forces across 11,520 DMA scenarios

C.2.2. Feature analyses

The following paragraphs provide of each feature the distribution, scatter plots with the targets, and the Spearman's correlation coefficient.

C.2.2.1. Water Depth (x_1)

Scenarios were sampled at low tide and high tide, corresponding to water depths of 16.53 and 18.48 meters, respectively.

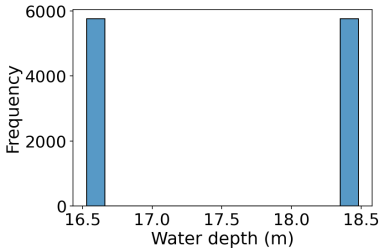

Figure C.4: Distribution of the water depth values in the DMA dataset

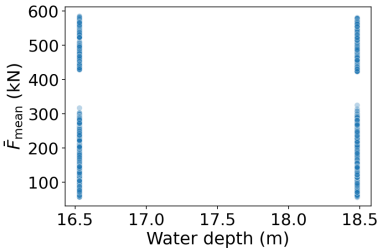

Figure C.5: Water depth versus $\bar{F}_{\text{mean}}$ ($r_s = -0.00$)

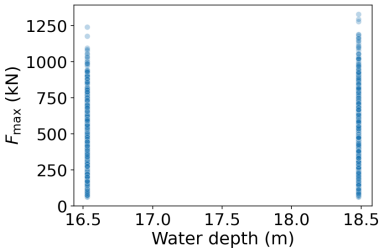

Figure C.6: Water depth versus F_{max} ($r_s = -0.02$)

C.2.2.2. Number of Lines (x_2)

The number of mooring lines was evenly distributed between 12 and 16.

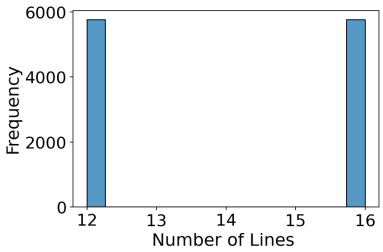

Figure C.7: Distribution of the number of lines in the DMA dataset

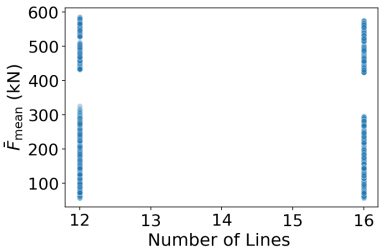

Figure C.8: Number of lines versus $\bar{F}_{\text{mean}}$ ($r_s = -0.05$)

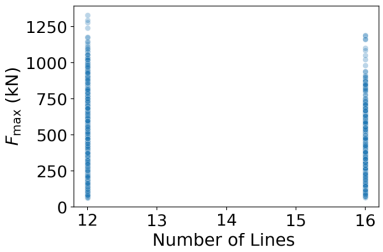

Figure C.9: Number of lines versus F_{max} ($r_s = -0.02$)

C.2.2.3. Mooring line material (x_3, x_4)

The mooring line material is encoded using two binary indicators: x_3 for nylon, and x_4 for polyester.

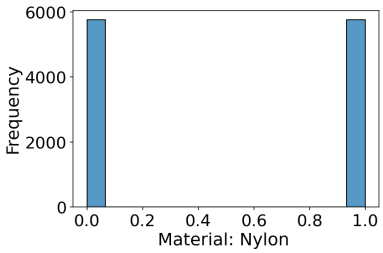

Figure C.10: Distribution of nylon lines in the DMA dataset

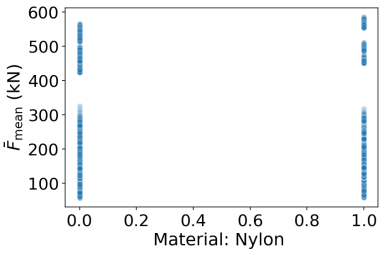

Figure C.11: Nylon lines versus $\bar{F}_{\text{mean}}$ ($r_s = 0.04$)

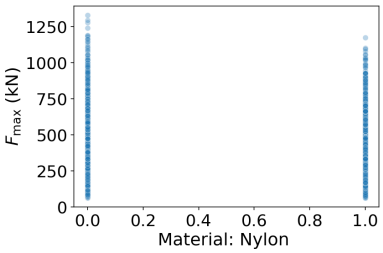

Figure C.12: Nylon lines versus F_{max} ($r_s = -0.03$)

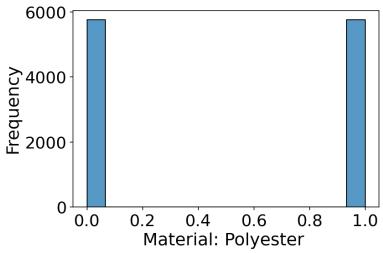

Figure C.13: Distribution of polyester lines in the DMA dataset

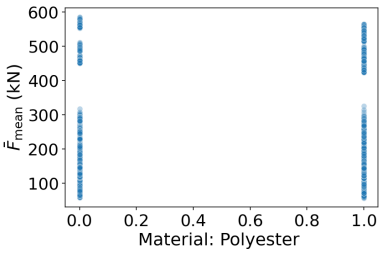

Figure C.14: Polyester lines versus $\bar{F}_{\text{mean}}$ ($r_s = -0.04$)

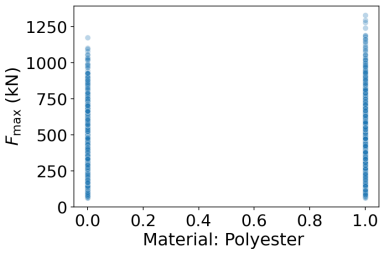

Figure C.15: Polyester lines versus F_{max} ($r_s = 0.03$)

C.2.2.4. Minimum Breaking Load (MBL) (x_5)

MBL values were sampled at 120, 130, and 150 tonnes.

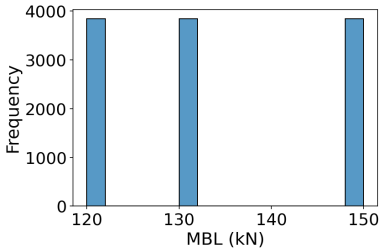

Figure C.16: Distribution of MBL values in the DMA dataset

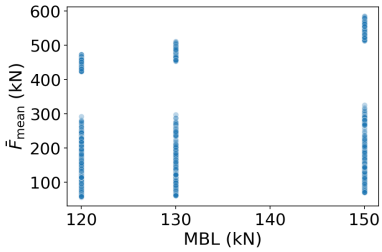

Figure C.17: MBL versus $\bar{F}_{\text{mean}}$ ($r_s = 0.19$)

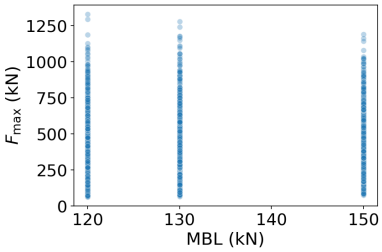

Figure C.18: MBL versus F_{max} ($r_s = 0.11$)

C.2.2.5. Pretension (x_6)

For all scenarios, pretension was assigned one of four discrete values: 5%, 10%, 20%, or 40% of the mooring line's MBL. This feature shows a very strong positive monotonic correlation with both target variables, indicating that higher pretension levels consistently lead to increased mooring line forces.

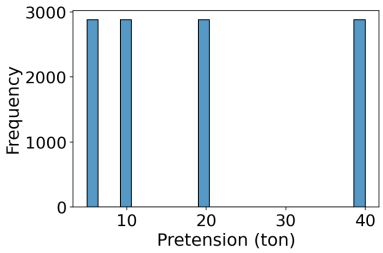

Figure C.19: Distribution of pretension values in the DMA dataset

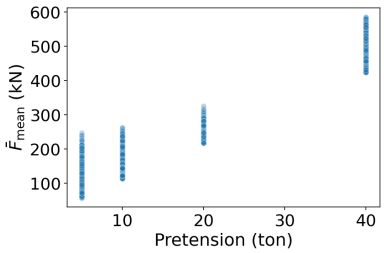

Figure C.20: Pretension versus $\bar{F}_{\text{mean}}$ ($r_s = 0.95$)

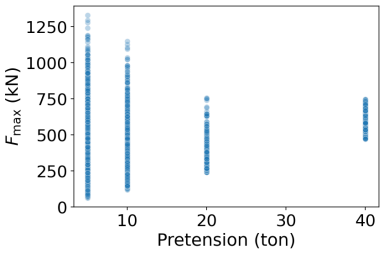

Figure C.21: Pretension versus F_{max} ($r_s = 0.66$)

C.2.2.6. Wind Area (x_7)

The wind area is expressed as a percentage of the fully loaded vessel profile and was sampled at 40%, 60%, 80%, and 100%.

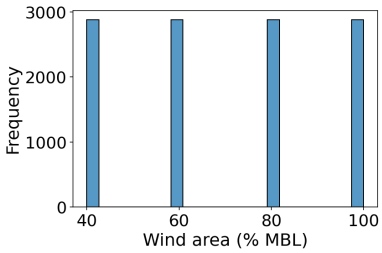

Figure C.22: Distribution of wind area values in the DMA dataset

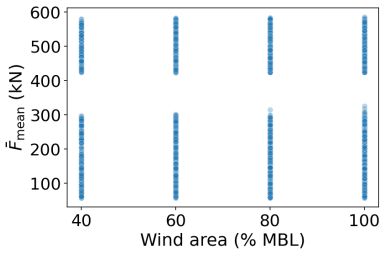

Figure C.23: Wind area versus $\bar{F}_{\text{mean}}$ ($r_s = 0.03$)

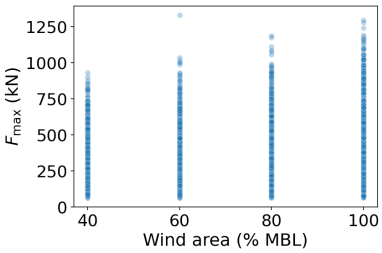

Figure C.24: Wind area versus F_{max} ($r_s = 0.07$)

C.2.2.7. Viscous Damping (x_8)

Evenly sampled values of 0%, 2%, and 4% represent varying levels of added damping.

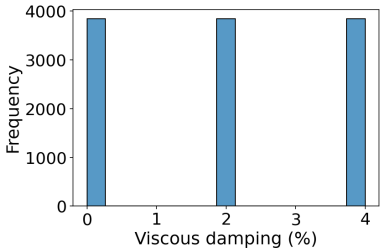

Figure C.25: Distribution of viscous damping values in the DMA dataset

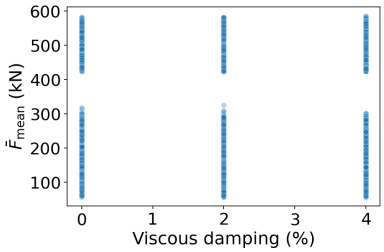

Figure C.26: Viscous damping versus $\bar{F}_{\text{mean}}$ ($r_s = -0.00$)

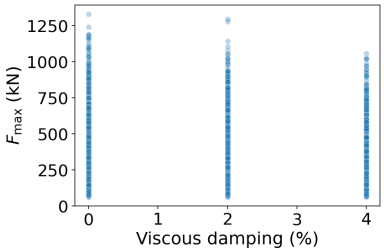

Figure C.27: Viscous damping versus F_{max} ($r_s = -0.02$)

C.2.2.8. Wind Velocity (x_9)

Wind velocity was varied between 5 m/s and 18 m/s.

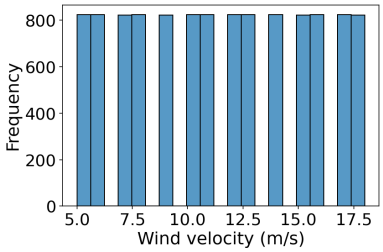

Figure C.28: Distribution of wind velocity values in the DMA dataset

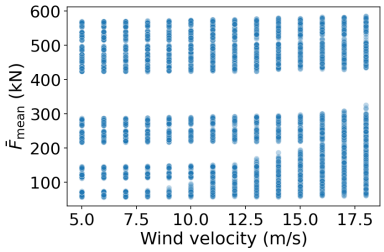

Figure C.29: Wind velocity versus $\bar{F}_{\text{mean}}$ ($r_s = 0.14$)

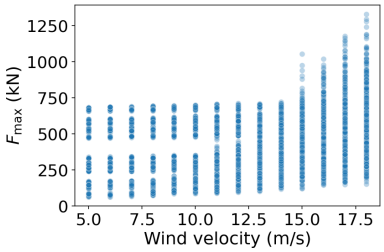

Figure C.30: Wind velocity versus F_{max} ($r_s = 0.47$)

C.2.2.9. Wind direction (x_{10}, x_{11})

The wind direction was uniformly sampled between 173° and 263° to represent the prevailing westerly winds in the region. To account for the cyclic nature of directional data, the wind direction was transformed into its sine (x_{10}) and cosine (x_{11}) components.

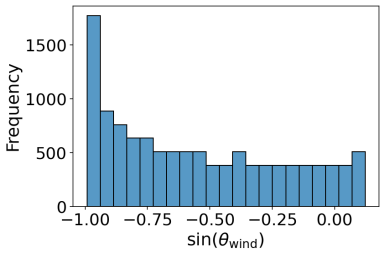

Figure C.31: Distribution of the sine components values in the DMA dataset

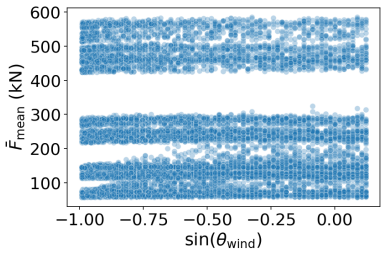

Figure C.32: Sine of the wind direction versus $\bar{F}_{\text{mean}}$ ($r_s = 0.08$)

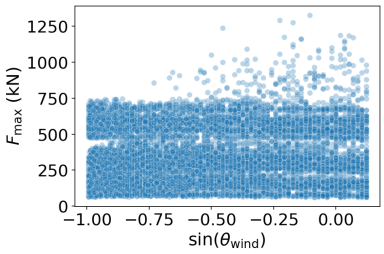

Figure C.33: Sine of the wind direction versus F_{max} ($r_s = 0.13$)

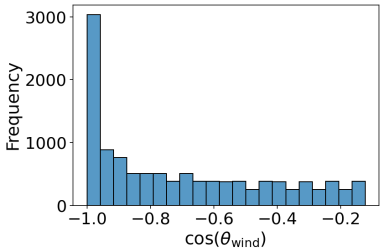

Figure C.34: Distribution of the cosine components values in the DMA dataset

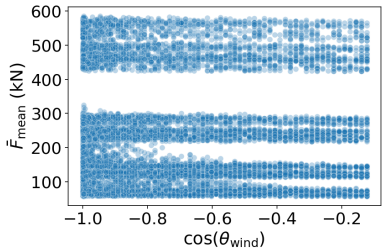

Figure C.35: Cosine of the wind direction versus $\bar{F}_{\text{mean}}$ ($r_s = -0.08$)

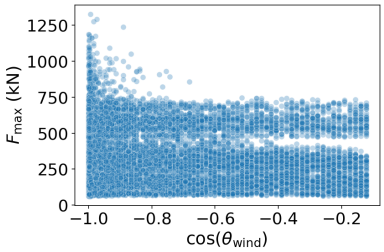

Figure C.36: Cosine of the wind direction versus F_{max} ($r_s = -0.14$)

C.3. Correlation coefficients

Spearman's correlation coefficient r_s ranges from -1 (perfect negative monotonic correlation) to 1 (perfect positive monotonic correlation). It is suitable for detecting nonlinear but monotonic relationships (Xiao et al., 2016). Non-monotonic such as perfect quadratic relationships, however, are not captured by this measure.

Figure C.37 presents the correlation matrix between the input features and target values. As the feature values were independently sampled, the correlation coefficients between input features are very low, as expected.

Regarding the mean mooring line force, pretension exhibits an extremely strong monotonic relationship ($r_s = 0.95$). This is followed by weak correlations with MBL ($r_s = 0.19$) and wind velocity ($r_s = 0.14$).

For the maximum mooring line force, pretension also shows the strongest correlation ($r_s = 0.66$), followed by a moderate correlation with wind velocity ($r_s = 0.47$). The wind direction components have weaker correlations: cosine ($r_s = -0.14$) and sine ($r_s = 0.13$). MBL follows closely with $r_s = 0.11$.

All other features show negligible correlation with the targets ($|r_s| < 0.10$), indicating very weak monotonic relationships.

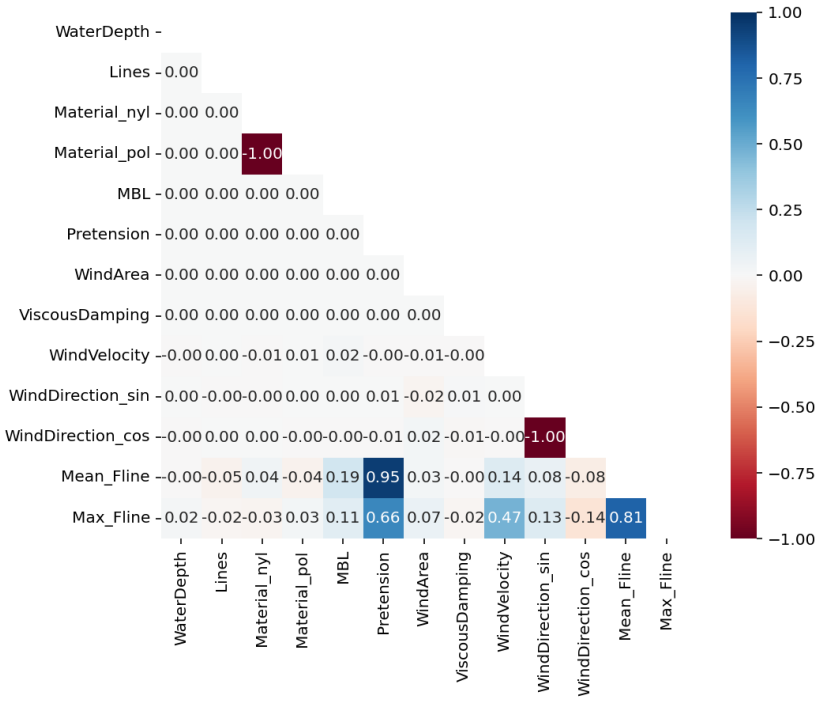

Figure C.37: Spearman's correlation coefficients between input features and target values

D

Sensitivity analysis of Multi-Criteria Analysis

Multi-Criteria Analysis (MCA) is inherently sensitive to the subjective selection of weights assigned to objectives and criteria. To evaluate the robustness of the MCA outcomes under varying priorities, a sensitivity analysis was performed.

The weights of the three objectives were systematically varied, while preserving their relative importance: accuracy was considered more important than efficiency, which in turn was prioritized over interpretability (accuracy > efficiency > interpretability), as determined in collaboration with the Port of Rotterdam.

For the actual MCA that determined the final DMA metamodel in Subsection 5.3.4, the following weights were applied: accuracy 55%, efficiency 30%, and interpretability 15%, in line with the defined priority ordering. This configuration resulted in total weighted scores of 73.70 for the LR model and 84.50 for the MLP model, making MLP the selected metamodel.

D.1. Method

The objective weights were varied in steps of 5%, while ensuring the total sum remained 100%. within each objective, the weights of the criteria were kept in fixed proportion. The sensitivity analysis was performed based on the predetermined criterion scores assigned to both models as presented in Subsection 5.3.4. These weights and scores are provided in Table D.1.

For each weight configuration, the total weighted score was computed for both the LR and MLP models. The model with the highest score was labeled the “winner”.

Table D.1: Proportional criteria weights and criteria scores of the candidate models

Objective	Criterion	Weight	Score	
			LR	MLP
Accuracy	RMSE	35/55	0.34	0.90
	R^2	20/55	0.84	1.00
Efficiency	Inference time	25/30	1.00	1.00
	Development effort	5/30	1.00	0.10
Interpretability	Transparency	1	1.00	0.50

D.2. Results

Table D.2 presents the results for all tested objective weight configurations, along with the resulting total scores for each model and the selected winner.

Although the weights were varied, the relative importance ordering (accuracy > efficiency > interpretability) was always preserved. The LR model was only selected as the winner in one configuration, where accuracy was weighted at 40%, efficiency at 35%, and interpretability at 25%. In all other configurations, where accuracy received a weight of 50% or more, the MLP model consistently outperformed LR.

Table D.2: Objective weight configurations and resulting model scores

No.	Objective weights (%)			Total weighted score		Winner
	Accuracy	Efficiency	Interpretability	LR	MLP	
1	40	35	25	80.87	79.70	LR
2	45	40	15	78.48	83.64	MLP
3	45	35	20	78.48	81.89	MLP
4	45	30	25	78.48	80.14	MLP
5	50	45	5	76.09	87.57	MLP
6	50	40	10	76.09	85.82	MLP
7	50	35	15	76.09	84.07	MLP
8	50	30	20	76.09	82.32	MLP
9	55	40	5	73.70	88.00	MLP
10	55	35	10	73.70	86.25	MLP
11*	55	30	15	73.70	84.50	MLP
12	55	25	20	73.70	82.75	MLP
13	60	35	5	71.31	88.43	MLP
14	60	30	10	71.31	86.68	MLP
15	60	25	15	71.31	84.93	MLP
16	65	30	5	68.92	88.86	MLP
17	65	25	10	68.92	87.11	MLP
18	65	20	15	68.92	85.36	MLP
19	70	25	5	66.53	89.30	MLP
20	70	20	10	66.53	87.55	MLP
21	75	20	5	64.14	89.73	MLP
22	75	15	10	64.14	87.98	MLP
23	80	15	5	61.75	90.16	MLP

* The actual weight configuration used for evaluating the candidate DMA metamodels

D.3. Conclusion

The MLP model is the justified winner based on the individual criterion scores. The MCA results are robust with respect to variations in the objective weights, provided that the relative importance remains accuracy > efficiency > interpretability and the internal criterion weights are proportional.

Additionally, based on stakeholder input it was concluded that accuracy should be valued at least as highly as efficiency and interpretability combined. Therefore, in all tested configurations where accuracy received a weight of 50% or more, the MLP model was consistently selected as the most suitable model.

E

Measurement data for updating input parameters

This appendix presents the measurements recorded during the event on January 21 and 23, 2024, when the Cartagena Express was moored at the ECT berth. Furthermore, it explains the process by which the respective measurements were consolidated into a single representative value for each parameter.

E.1. Mooring line force

The mooring line forces of four lines were measured with Smart Bollards during the measurement campaign.

E.1.1. Smart bollard

The Smart Bollard (Figure E.1), developed by Straatman in cooperation with Port of Rotterdam, is a device that provides real-time data on mooring line loads. It replaces traditional bollards and can be placed on existing anchor platforms using an adapter plate. The Smart Bollard maintains the familiar T-shape design, but waves in the base plate allow the shaft to move within safe limits. High-precision sensors measure the deformation in three directions, which is then converted into bollard force, line angle, and line direction. The collected data is transmitted wirelessly. Following a pilot phase, a large-scale deployment of Smart Bollards is being installed along selected quays in the Port of Rotterdam.

Figure E.1: Traditional bollard (left) and Smart Bollard (right) in the Port of Rotterdam (Rijnmond, 2021)

E.1.2. Smart bollard measurements

The Cartagena Express was moored using 16 lines, arranged in the same pattern as defined in the case study. Her lines were made of polyester and had an MBL of 163 tons. Lines 11 and 12 were both

attached to Smart Bollard 179O, line 15 to 179W, and line 16 to 178O, as illustrated in Figure E.2. It is assumed that the measured bollard loads correspond directly to the forces in the attached mooring lines.

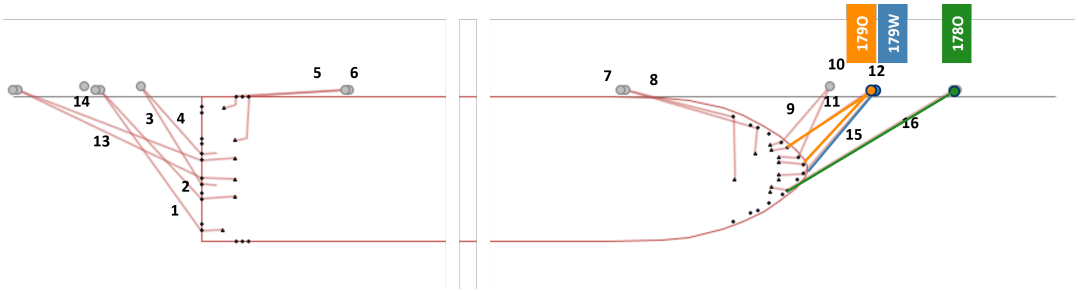

Figure E.2: Mooring layout of the stern of the observed vessel with line 11 and line 12 both attached to Smart Bollard 178O, line 15 to 179W, and line 16 to 179O

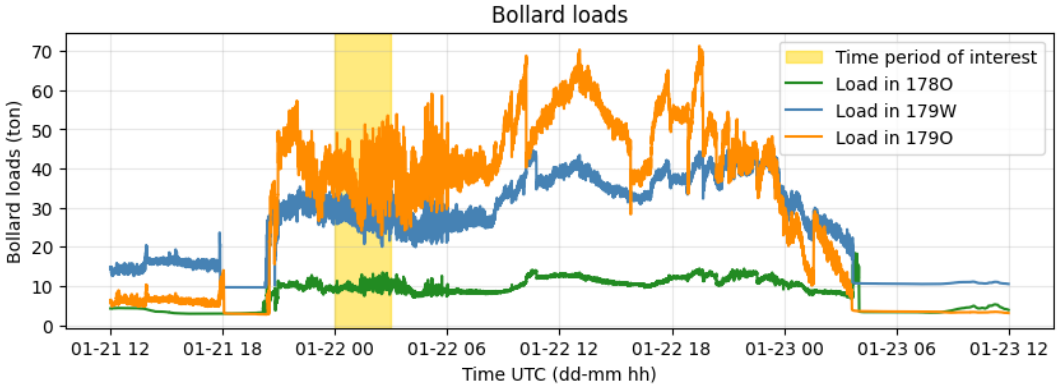

Figure E.3: Measurements of the Smart Bollards

Since the DMA metamodel requires target variables derived from mooring line forces, the available measurements must be translated accordingly. Targets mean ($\bar{F}_{\text{mean}}$) and maximum (F_{max}) mooring line force can both be estimated from individual mooring line force measurements.

As shown in Figure E.3, Smart Bollard 178O (connected to line 16) experiences the lowest loads. Bollard 179O, with lines 11 and 12 attached, records the highest total loads. Assuming an even load distribution between the two lines, the individual force in each is still lower than the force in line 15, which is connected to 179W. Therefore, the force measured at bollard 179W is taken as representative of the individual line forces.

To ensure consistency with the DMA simulation duration, the selected measurement window also spans three hours, from 2024-01-22 00:00:00 to 2024-01-22 03:00:00, as highlighted in yellow in the figure. During this period, the mean and maximum loads recorded at bollard 179W were 28.9 tonnes and 38.5 tonnes, respectively, equivalent to 289.070 kN and 385.000 kN.

As detailed in Section C.1, analysis of the synthetic DMA dataset (comprising 16 mooring lines) showed that the mean force in line 15 corresponds to approximately 102.86% of the overall average mean line force $\bar{F}_{\text{mean}}$, while its maximum force accounts for 80.09% of the overall maximum mooring line force F_{max}. To estimate the true targets for the metamodel, the measured values are scaled accordingly:

- The actual mean force per line is estimated by scaling the observed mean value of 289.0 kN by a factor of $\frac{100}{102.86}$, yielding $\bar{F}_{\text{mean}} = 281.032$ kN.

- The actual maximum mooring line force is estimated by scaling the observed maximum value of 385.0 kN by a factor of $\frac{100}{80.09}$, resulting in $F_{\text{max}} = 480.709$ kN.

E.2. Wind area vessel

The wind area of the vessel changed over time due to loading and unloading. Upon arrival, the front area was 1,790 m^2 and the side area was 6,479 m^2 according to photos. Upon departure on January 23, the front area was 1,810 m^2 and the side area 7,127 m^2.

A front area of 1,870 m^2 was assumed, corresponding to a ship with no containers protruding above or beside the superstructures on deck. The side area was averaged, resulting in 6,803 m^2 which corresponds to 39 containers on deck visible from the side. This means that the number of containers on deck was 12% of the total possible number of containers on deck. The wind area was thus set to 12%.

In reality, the draught was 13.00 m upon arrival, and 12.60 m upon departure. In the metamodel, a draught of 12.25 m, as in the case study, is assumed, but the reduction in wind area due to the larger draught was accounted for in the wind area percentage.

E.3. Environmental conditions

During the measurement campaign, the wind and water level were measured at two different sensor stations.

E.3.1. Sensor locations

Wind velocity and direction were measured at the Noorderpier (NRDP) station, located approximately 3.5 km from the berth. Water level data were obtained from the Europahaven (EURH) station, situated roughly 2.2 km from the DDN berth (Google Maps, 2024). The locations of these measurement stations are shown in Figure E.4.

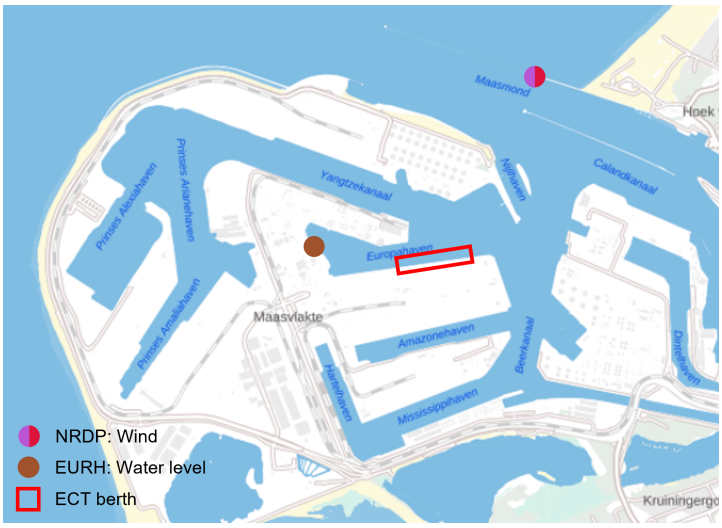

Figure E.4: The locations of the water level sensor at Europhaven (EURH) and wind sensors at Noorderpier (NRDP), and the ECT berth (Google Maps, 2024)

E.3.2. Wind

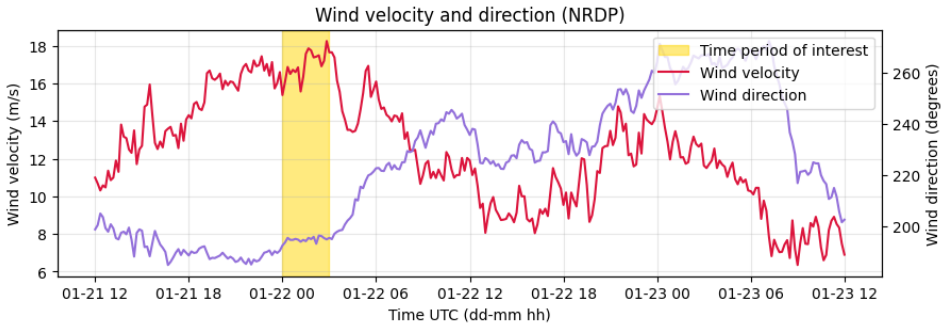

Figure E.5: Wind conditions measured at Noorderpier (NRDP) during the event

Figure E.5 illustrates the wind velocity and wind direction at the wind sensor location, Noorderpier (Figure E.4), during the event. The yellow area highlights again the time period of interest. Here, the least favorable wind conditions are observed, characterized by high wind speeds and a direction nearly perpendicular to the ship (263°). During the time period of interest the average wind velocity was 16.97 m/s and average wind direction was 194.64°.

The Port of Rotterdam provides conversion factors to translate the wind measured at Noorderpier to local wind conditions in the port. Specifically, for the observed wind direction, the wind speed amplification factor at the ECT berth was estimated to be 0.972, yielding a wind velocity of 16.49 m/s. The wind direction is assumed to be the same and is rounded to 195°.

E.3.3. Water level

Figure E.6 shows the recorded water level in the Europahaven during the event.

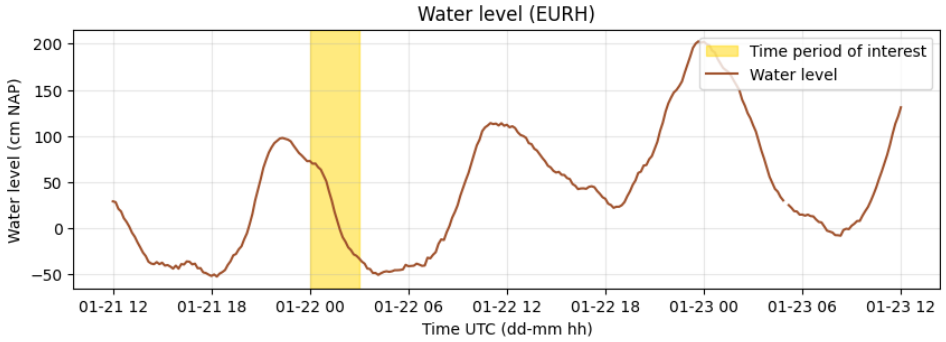

Figure E.6: Water level measurement in the Europahaven (EURH) during the event

During the time period of interest, the average water level was +20.22 cm NAP. It assumed that the water level at the ECT berth is similar to the water level at the sensor location. The defined water level, referenced to NAP, was converted to water depth relative to the seabed, which is located at -17.20 m NAP. Consequently, a measured water level of 20.22 cm NAP corresponds to a water depth of 17.40 m.

E.4. Measurement sample

For each measured parameter one value was found to create a sample that represents the time period of interest in the event best in the right location. The overview of these measurement values in the correct formats and units is presented in Table E.1.

Table E.1: Measurement of the mooring of Cartagena Express at the DDN berth at January 21 and 22, 2024

Parameter	Measured value	Metamodel variable type	
		Input	Output
Water level (m)	17.40 m	x_1	
Number of lines	16	x_2	
Mooring line material (-)	Polyester	x_3, x_4	
MBL (ton)	163 ton	x_5	
Wind area (%)	12%	x_7	
Wind velocity (m/s)	16.49 m/s	x_9	
Wind direction (°)	194.64°	x_{10}, x_{11}	
Mean mooring line force $\bar{F}_{\text{mean}}$	281.032 kN		y_1
Maximum mooring line force F_{max}	480.709 kN		y_2

F

Bollard capacity exceedance probability

This appendix provides an illustrative example of how the metamodel can be used to assess the probability of bollard load exceedance due to mooring line forces over its operational lifetime. It outlines the data sources, assumptions, and approach used in a simplified Monte Carlo simulation to demonstrate this application.

F.1. Reliability requirements

The Safe Working Load (SWL) of a structure corresponds to the Serviceability Limit State (SLS) and represents the maximum expected load under normal operational conditions. The design load F_d relates to the Ultimate Limit State (ULS) and defines the maximum load capacity a structure can sustain before collapse of failure occurs. Between the SWL and the design load, the structure is allowed to undergo deformation without experiencing failure.

Structural reliability is commonly expressed using the reliability index β and probability of failure P_f, which are standard metrics according to *Eurocode – Basis of structural and geotechnical design* (2025). Independent from the reference period, the functional relationship between failure probability and reliability index is given by:

$$P_f = \Phi(-\beta) \tag{F.1}$$

Where

P_f probability of failure
$\Phi()$ the standard normal cumulative probability distribution function
β reliability index

Table F.1: Relation between failure probability P_f and reliability index β (*Eurocode – Basis of structural and geotechnical design*, 2025)

P_f	10^{-1}	10^{-2}	10^{-3}	10^{-4}	10^{-5}	10^{-6}	10^{-7}
β	1.28	2.33	3.09	3.72	4.26	4.75	5.20

Target reliability index values β for 1-year and 50-year reference periods, applicable to design conditions in the ULS, must be met to consider the structure safe. These target values are listed in Table F.2.

Table F.2: Target values for reliability index β for different consequence classes

Consequence class	1-year reference period	50-year reference period	
	β	β	$P_{f,50}$
CC3	5.2	4.3	$\sim 10^{-5}$
CC2	4.7	3.8	$\sim 10^{-4}$
CC1	4.2	3.3	$\sim 10^{-3}$

When a load is considered the leading action and the resistance uncertainty is not taken into account, the reliability index β should be reduced by a factor of 0.7 to ensure a more conservative safety requirement.

F.2. Bollard information and mooring frequency

The DDN berth is equipped with bollards with a SWL of 1000 kN. Applying a safety factor of 1.5 (Broos et al., 2018), the corresponding design load F_{design} is 1,500 kN. The operational design lifetime of these bollards T_{life} is 100 years. According to the Port of Rotterdam's guidelines, a maximum of three mooring lines may normally be attached to a single bollard (Broos et al., 2018). However, at the DDN berth, the maximum is limited to two lines.

It is assumed that bollards fall under Consequence Class 1 (CC1), and that approximately 350 vessels are moored at the berth each year, defining the annual mooring frequency f_{annual}.

F.3. Input parameter distributions

The distributions for each input parameter of the DMA metamodel are presented in Table F.3 and are described in the following subsections.

Table F.3: Overview of input parameters and their distributions used for Monte Carlo simulations

Input parameter		Distribution	Parameters	Remarks
x_1	Water depth (m)	Uniform	Min = 16.53, Max = 18.48	Based on tidal measurements in the Europahaven (Janssen & Van Hell, 2023)
x_2	Number of lines (-)	Discrete (conditional)	12 (2/3), 16 (1/3); forced 16 if $v_{\text{wind}} \geq 13.9$ m/s	Based on mooring configuration practice by the KRVE (Sterkenbrug, 2024)
x_3, x_4	Line material (-)	Categorical	Nylon (51/94), Polyester (43/94)	Based on observations in the Port of Hamburg by Heitmann (2024)
x_5	MBL (t)	Truncated normal (by material)	Nylon: μ = 114, σ = 15 Polyester: μ = 120, σ = 15 Bounds: [90, 160]	Based on observations in the Port of Hamburg by Heitmann (2024)
x_6	Pretension (% MBL)	Truncated normal	μ = 10, σ = 5; bounds: [0, 40]	Based on Lamont-Smith (2019), Barros and Mazzilli (2018), M. Yan et al. (2023), and Van Zwijnsvoorde et al. (2018)
x_7	Wind area (%)	Truncated normal	μ = 70%, σ = 15; bounds: [40, 100]	Reflects varying container loading
x_8	Viscous damping (%)	Uniform	Min = 0, Max = 6	Based on values used in DMA practice by Haskoning
x_9	Wind velocity (m/s)	Joint (by direction)	Ranges per direction [0, 32.6]	Based on wind statistics at Beerkanaal Radarpost 37 (Janssen & Van Hell, 2023)
x_{10}, x_{11}	Wind direction (°)	Discrete	180°, 210°, 240°	Trained model range (173° – 263°)

F.3.1. Water depth

A uniform distribution is assumed between the observed mean low and high tide levels at the ECT berth (16.53 m and 18.48 m), based on measurements from the Europahaven sensor between 2002

and 2022. This reflects the assumption of equal likelihood across the tidal range.

F.3.2. Number of mooring lines

According to Sterkenbrug (2024), vessels like the Cartagena Express typically deploy 12 mooring lines under standard conditions. However, under extreme weather or when sufficient bollards are available, 16 lines may be deployed.

For the simulation, a discrete distribution with probabilities $\frac{2}{3}$ for 12 lines and $\frac{1}{3}$ for 16 lines was used. Additionally, to represent operational safety protocols, the number of lines is automatically set to 16 when the wind velocity exceeds 13.9 m/s.

F.3.3. Mooring line material and MBL

Only nylon and polyester lines are considered, as the DMA metamodel was only trained on these materials. Predictions involving other materials would therefore be impossible and unreliable.

Based on observations at the Port of Hamburg by Heitmann (2024) in Table B.1 for 300 m and 330 m vessels, 51% of the mooring lines are nylon, with an average MBL of 114 tonnes and 43% are polyester, with an average MBL of 120 tonnes.

The material sampling follows a probability distribution of $\frac{51}{94}$ for nylon and $\frac{43}{94}$ for polyester. MBL values are drawn from a truncated normal distribution with a mean of 114 t for nylon and 120 t for polyester lines, a standard deviation of 10 t, and bounds set between 90 and 160 t.

F.3.4. Pretension

As discussed in Subsection 2.2.1, the pretension in mooring lines typically ranges between 5% and 10% of the MBL, according to values reported in literature (Lamont-Smith, 2019; Barros & Mazzilli, 2018; M. Yan et al., 2023; Van Zwijnsvoorde et al., 2018).

In this study, pretension values are sampled from a truncated normal distribution with a mean of 10% of the MBL and a standard deviation of 5%. The distribution is bounded between 0% and 40% of the MBL to ensure physical realism and to allow for occasional high pretension scenarios, as may occur in practice.

F.3.5. Wind area

The wind-exposed area, representing the above-deck container stack, is expressed as a percentage of the maximum possible exposure. A truncated normal distribution is assumed, with a mean of 70% and a standard deviation of 15%, to reflect different loading conditions while ensuring values remain within the the range of 40% to 100%.

F.3.6. Viscous damping

A uniform distribution from 0% to 6% is assumed. This reflects the typical values used by Haskoning in their DMA simulations and represents uncertainty evenly across this range.

F.3.7. Wind velocity and direction

The wind joint distribution presented in Table F.4, derived from historical wind data collected between 2009 and 2019 at the Beerkanaal Radarpost 37 Janssen and Van Hell (2023), forms the basis of the applied wind distribution. Due to its close proximity to the DDN berth, this measurement location is considered representative of the local wind conditions.

Table F.4: Wind frequency Beerkanaal Radarpost 37 between 2009 and 2019 (Janssen & Van Hell, 2023)

Wind direction (°)		Wind velocity (m/s)							
		[0, 5.5) 0–3 Bft	[5.5, 8) 4 Bft	[8, 10.8) 5 Bft	[10.8, 13.9) 6 Bft	[13.9, 17.2) 7 Bft	[17.2, 20.8) 8 Bft	[20.8, 32.6) 9–11 Bft	*Total*
[345, 15)	North	4.81%	2.40%	1.33%	0.43%	0.05%	0.00%	0.00%	9.03%
[15, 45)	NNE	2.72%	1.96%	1.21%	0.37%	0.05%	0.00%	0.00%	6.31%
[45, 75)	ENE	3.06%	1.82%	1.02%	0.22%	0.01%	0.00%	0.00%	6.13%
[75, 105)	East	4.51%	2.65%	0.98%	0.22%	0.06%	0.00%	0.00%	8.42%
[105, 135)	ESE	2.08%	0.87%	0.35%	0.05%	0.00%	0.00%	0.00%	3.35%
[135, 165)	SSE	2.89%	1.86%	0.67%	0.10%	0.00%	0.00%	0.00%	5.52%
[165, 195)	South	6.11%	3.14%	1.67%	0.43%	0.05%	0.01%	0.00%	11.41%
[195, 225)	SSW	5.60%	3.95%	2.14%	0.53%	0.04%	0.00%	0.00%	12.26%
[225, 255)	WSW	4.51%	5.03%	4.14%	1.17%	0.10%	0.00%	0.00%	14.96%
[255, 285)	West	3.24%	2.77%	2.37%	1.19%	0.26%	0.04%	0.00%	9.88%
[285, 315)	WNW	3.26%	1.69%	0.92%	0.35%	0.10%	0.01%	0.00%	6.34%
[315, 345)	NNW	3.86%	1.65%	0.72%	0.16%	0.02%	0.00%	0.00%	6.42%
Total		*46.64%*	*29.79%*	*17.52%*	*5.23%*	*0.75%*	*0.07%*	*0.00%*	*100%*

The DMA metamodel is only valid for wind directions between 173° and 263°, which statistically occur most frequently and are associated with the highest mooring line forces as mentioned in Subsection B.2.8.

To ensure consistency and validity of the model predictions, only three representative directions were selected: 180° (South), 210° (SSW), and 240° (WSW). The sampling probabilities for these directions are derived from their relative frequencies and are normalized to sum up to 1: 180° has a probability of $\frac{11.41}{38.64}$, 210° has a probability of $\frac{12.26}{38.64}$, and 240° has a probability of $\frac{14.96}{38.64}$.

Wind speeds are sampled conditionally based on the selected direction and a joint distribution of wind direction and speed range. Each sampled wind direction corresponds to a speed interval and probability, ensuring that the wind conditions reflect realistic joint occurrences.

F.4. Monte Carlo sampling

Monte Carlo sampling is applied by repeatedly drawing random samples from the defined input distributions. These sampled inputs are evaluated using the metamodel to predict the corresponding maximum mooring line force F_{max}.

The total bollard load $F_{bollard}$ is approximated by multiplying the maximum predicted line force F_{max} by the number of mooring lines on a single bollard n:

$$F_{\text{bollard}} = F_{\text{max}} \cdot n \tag{F.2}$$

By aggregating a large number of such simulated outcomes ($N_{\text{samples}} = 100{,}000$), the probability distribution of the bollard load is estimated.

F.5. Probability calculation

The exceedance probability per mooring is computed by evaluating how often the predicted bollard load surpasses either the SWL or the design load (1.5×SWL). The basic exceedance probability per mooring event is defined as:

$$P_{\text{event}} = \frac{N_{\text{exceedance}}}{N_{\text{samples}}} \tag{F.3}$$

The probability that the load does not exceed the capacity in a single mooring is $P_{\text{no event}} = 1 - P_{\text{event}}$.

Assuming an annual mooring frequency of f_{annual} and a reference period of T_{ref} years, the probability that the load never exceeds the capacity during the reference period is:

$$P_{\text{no ref}} = (1 - P_{\text{event}})^{f_{\text{annual}} \cdot T_{\text{ref}}} \tag{F.4}$$

Hence, the probability that the capacity is exceeded at least once during the reference period becomes:

$$P_{\text{ref}} = 1 - (1 - P_{\text{event}})^{f_{\text{annual}} \cdot T_{\text{ref}}} \tag{F.5}$$

F.6. Results

Figure F.1 shows the distribution plot of the maximum mooring line force (F_{max}) calculated by the DMA metamodel, for the 100,000 Monte Carlo samples.

The distribution of maximum bollard load F_{bollard} is calculated for cases where one, two, or three mooring lines are attached to the same bollard. Several standard distributions were fitted to the data, including Normal, Lognormal, Weibull, and Gamma. Among the fitted distributions, the Lognormal distribution provided the best fit for the cases with one and two mooring lines, while the Gamma distribution offered the best fit for the case with three lines, as visualized in Figure F.2.

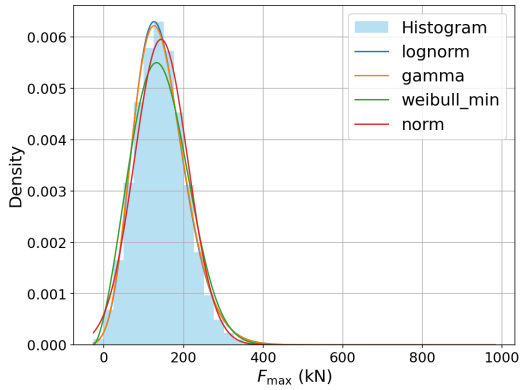

Figure F.1: Distribution of F_{max} (N=100,000)

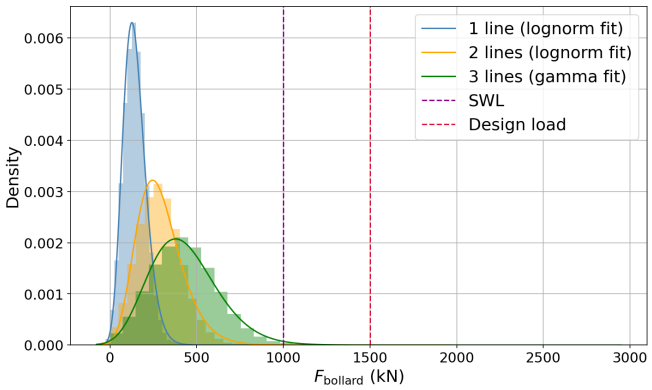

Figure F.2: Histogram and probability density of the maximum bollard load $F_{bollard}$ (N=100,000)

The probability that the bollard load exceeds the SWL, $P(F_{\text{bollard}} > F_{\text{SWL}})$, is calculated using the fitted distributions for different reference periods and varying numbers of attached lines. Similarly, the probability of bollard failure, defined as the bollard load exceeding the design load, is given by $P(F_{\text{bollard}} > F_{\text{design}})$. The distribution and resulting probabilities, along with the corresponding reliability index for a 50-year reference period, are summarized in Table F.5.

Table F.5: Fitted probability distributions of bollard load for one, two, and three lines per bollard, with exceedance probabilities for the SWL and design load per event, over 50 and 100 years (operational lifetime), and the corresponding reliability index for 50 years

Lines per bollard	Fitted distribution	Distribution parameters	$P(F_{\text{bollard}} > F_{\text{SWL}})$			$P(F_{\text{bollard}} > F_{\text{design}})$			
			Per event	50 years	100 years	Per event	50 years	100 years	β_{50}
1	Lognormal	s: 0.18519; loc: -210.42220; scale: 347.98036	$8.41 \cdot 10^{-12}$	$1.47 \cdot 10^{-7}$	$2.94 \cdot 10^{-7}$	$0.00 \cdot 10^{0}$	$0.00 \cdot 10^{0}$	$0.00 \cdot 10^{0}$	∞
2	Lognormal	s: 0.24191; loc: -252.38312; scale: 527.41120	$1.75 \cdot 10^{-4}$	$9.53 \cdot 10^{-1}$	$9.98 \cdot 10^{-1}$	$3.46 \cdot 10^{-7}$	$6.03 \cdot 10^{-3}$	$1.20 \cdot 10^{-2}$	2.51
3	Gamma	a: 14.08968; loc: -313.99886; scale: 52.86210	$7.39 \cdot 10^{-3}$	$1.00 \cdot 10^{0}$	$1.00 \cdot 10^{0}$	$3.15 \cdot 10^{-5}$	$4.23 \cdot 10^{-1}$	$6.68 \cdot 10^{-1}$	0.19

As stated in Section F.1, the target reliability index β_{50} for a 50-year reference period for structures in CC1 is 3.3. When considering only the leading action, a reduction factor of 0.7 is applied, resulting in a stricter β_{50} of 2.31. This corresponds to a probability of failure of approximately 10^{-2} over 50 years.

The reliability indices shown in Table F.5 are higher than the required value of 2.31 for configurations with one or two mooring lines per bollard, indicating sufficient safety. However, the configuration with three lines does not meet this criterion, suggesting it is not safe according to *Eurocode – Basis of structural and geotechnical design* (2025).

For the configuration with two lines per bollard, the probability that the bollard load exceeds the SWL during the 100-year lifetime is nearly 100%. While a single exceedance of the SWL does not necessarily lead to immediate failure, it may cause plastic deformation or initiate fatigue damage. Over time, this can reduce the structural capacity of the bollard. It is important to note that the calculated probabilities and corresponding reliability indices do not account for fatigue effects. Therefore, even the two-line configuration may be considered borderline in terms of long-term safety when fatigue is taken into account.

F.7. Assumptions

This analysis serves as an illustrative example demonstrating how the metamodel can be applied to estimate the probability of bollard capacity exceedance. Several simplifying assumptions are made in this approach:

- Only a single simulation is performed per mooring event, even though a vessel may remain moored for an extended period (e.g., an entire day). This implies that environmental and operational conditions (i.e., the model inputs) are assumed to remain constant throughout the mooring event.
- It is assumed that all mooring events involve the Cartagena Express vessel, using an identical mooring line configuration each time. Additionally, it is assumed that the same bollard is consistently subjected to the maximum mooring line forces in every mooring event.
- Only wind directions of 180°, 210°, and 240° are considered, representing exclusively unfavorable wind conditions for mooring. This choice results in a conservative estimate of the exceedance probability.
- The DMA metamodel does not enforce physical constraints on its output, allowing it to predict negative mooring line forces or excessive high values that exceed the MBL, which are physically unrealistic. It does not model line breakage or the redistribution of the resulting loads among the remaining lines. Additionally, winch rendering, which typically occurs at 60% of the MBL and limits the actual force in a line (Subsection 2.2.2), is not accounted for.
- The total load on a bollard is estimated as the number of lines multiplied by the predicted maximum mooring line force. This approach assumes that all lines connected to the same bollard experience their peak force simultaneously, with equal magnitude and in the same direction. This

oversimplified, conservative assumption neglects differences in line angles, winch settings, and the true resultant of forces, making it an overestimation of true bollard loading conditions.

- The method assumes that forces from multiple mooring lines attached to the same bollard act in the same direction and does not account for their resultant force.
- Fatigue effects are not included in the analysis. The current approach only considers the ultimate limit state failure due to excessive loading, whereas a complete structural reliability assessment would also account for fatigue and accumulated damage over time.
- The design load of the bollard is set to 1.5 times the SWL, representing a fixed safety factor used to define structural limits.

F.8. Conclusion

This appendix demonstrated how the DMA metamodel can be applied to estimate the probability of bollard loads exceeding their capacity over over different time periods.

A Monte Carlo simulation was performed using the DMA metamodel, integrating realistic input parameter distributions with historical wind data and mooring practices, to generate a representative distribution of the maximum mooring line force. These forces were then scaled according to the number of lines per bollard in order to estimate the resulting bollard loads. Based on their distributions, the probability of exceeding the 1,000 kN SWL and the 1,500 kN design threshold during individual mooring events was evaluated. When combined with annual mooring frequencies, this approach provides a data-driven method to assess long-term exceedance risks.

Results show that as more lines are attached to a single bollard, the probability of exceeding both the SWL and design load increases significantly. For one or two lines per bollard, the calculated reliability indices over 50 years are higher than the target value of 2.31, indicating acceptable safety according to *Eurocode – Basis of structural and geotechnical design* (2025). However, configurations with three lines do not meet this criterion and are therefore considered unsafe.

While two-line configurations satisfy the reliability requirement, the probability of exceeding the SWL at least once during the 100-year lifetime is nearly 100%. Although a single exceedance does not imply immediate failure, it may lead to plastic deformation and fatigue damage, potentially reducing the bollard's capacity over time. Since fatigue effects are not included in the current analysis, the two-line configuration may still pose a long-term safety concern.

It is important to note that the metamodel does not enforce physical constraints: it may predict non-physical negative forces and does not consider mooring line breakage or the redistribution of forces after failure. Moreover, the bollard load is conservatively estimated by multiplying the maximum force of a single line by the number of lines. This approach likely overestimates the actual bollard load. At the same time, the DMA metamodel is limited to vessels of 333 meters, whereas larger vessels, which do call at the DDN berth, could impose even higher mooring forces.

Since the Rotterdam Port Authority allows two lines per bollard on the DDN berth, these results cannot be overlooked. It highlights the importance of carefully assessing mooring line forces and considering cumulative effects of multiple lines on a single bollard. Despite simplifications the analysis emphasizes the practical value of the DMA metamodel as a decision-tool for evaluating long-term bollard safety.

While the methodology relies on simplifying assumptions, it effectively demonstrates the practical value of the metamodel as a decision-support tool. These assumptions include a fixed vessel type and mooring configuration, limited wind directions, and use of measured wind data 1.5 km verderop. Additionally, it unrealistically assumes that all lines attached to the bollard simultaneously experience the highest peak forces across all lines. Line breakage is also not considered, meaning force redistribution among remaining lines is not accounted for, and negative values...

G

Additional figures

G.1. Learning curves

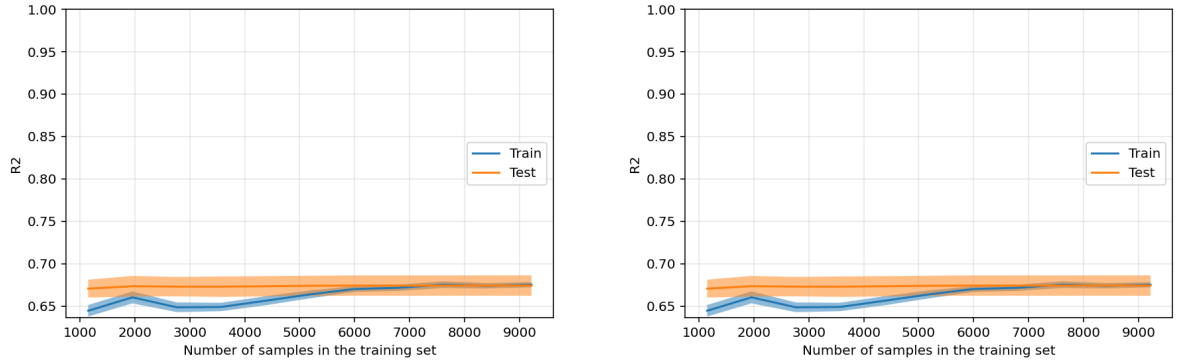

(a) LR - y_1

(b) LR - y_2

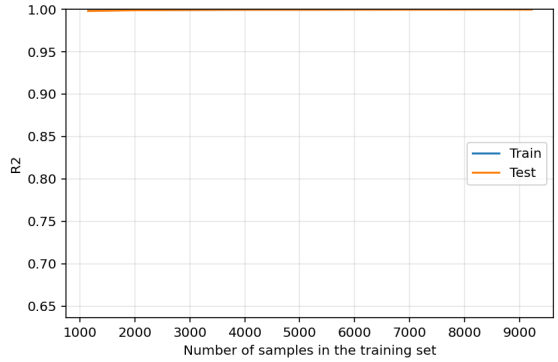

(c) MLP - y_1

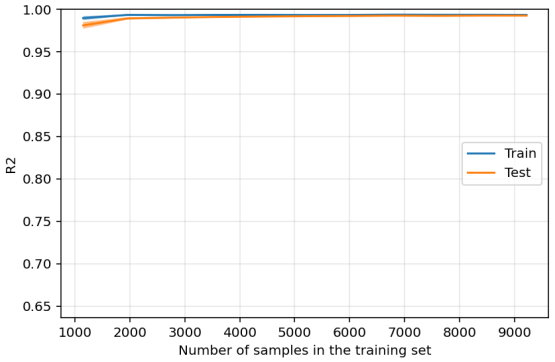

(d) MLP - y_2

Figure G.1: Learning curves of the two candidate models (LR and MLP) (LR and MLP) and both target variables (y_1: mean mooring line force, y_2: maximum mooring line force)